NASA TECHNICAL MEMORANDUM

NASA TM X-2814

NASA TM X-2814

DESIGN AND PERFORMANCE OF THE AMES ELECTRIC-ARC SHOCK TUNNEL

by John O. Reller, Jr.

Ames Research Center

Moffett Field, Calif. 94035

NATIONAL AERONAUTICS AND SPACE ADMINISTRATION • WASHINGTON, D. C. • JUNE 1973

1. Report No.	2. Government Accession No.	3. Recipient's Catalog No.
NASA TM X-2814		

4. Title and Subtitle	5. Report Date
DESIGN AND PERFORMANCE OF THE AMES ELECTRIC-ARC SHOCK TUNNEL	June 1973
	6. Performing Organization Code

7. Author(s)	8. Performing Organization Report No.
John O. Reller, Jr.	A-4606
	10. Work Unit No. 117–07–04–15

9. Performing Organization Name and Address	11. Contract or Grant No.
NASA Ames Research Center Moffett Field, Calif., 94035	
	13. Type of Report and Period Covered
12. Sponsoring Agency Name and Address	Technical Memorandum
National Aeronautics and Space Administration Washington, D. C. 20546	14. Sponsoring Agency Code

15. Supplementary Notes

16. Abstract

A high enthalpy shock tunnel using arc-heated helium as the driver gas has been designed for gasdynamic research at total stream energies from 7,000 to 35,000 J/g. The arc driver was found to be a relatively efficient energy converter. Tailored shock Mach numbers from 11.5 to 14.6 in air were demonstrated. A nozzle calibration with a total stream enthalpy of 18,600 J/g of air gave test times of 1.5 to 2.0 msec at flow Mach numbers from 16 to 24.

17. Key Words (Suggested by Author(s))	18. Distribution Statement
Shock Tunnels Nozzle Flow Are-discharge heating Calibrating Test facilities	Unclassified – Unlimited

19. Security Classif. (of this report)	20. Security Classif. (of this page)	21. No. of Pages	22. Price*
Unclassified	Unclassified	71	$3.00

* For sale by the National Technical Information Service, Springfield, Virginia 22151

TABLE OF CONTENTS

NOTATION

A	area
a	speed of sound
C	capacitance
C_1, C_1^*	defined in table 3
$\overline{C}$	$\dfrac{\mu_w T_\infty}{\mu_\infty T_w}$
C-V	constant volume process
CS	contact surface (interface)
D	diameter
d^*	nozzle throat diameter
ΔE	specific energy of reaction
f_n	natural resonant frequency
G	defined in appendix B
g	equivalence factor (see eq. (2))
H	enthalpy
K	model flow starting parameter
K_w	catalytic reaction rate
L	inductance or length
ℓ	shock wave–interface separation distance
Le	Lewis number
M	Mach number
M_F	effective freeze Mach number
M_{ST}	shock wave Mach number for tailored interface

ΔM_S	decrement in M_S due to viscous attenuation
m	molecular weight
P	pressure
P_b	surface pressure in inviscid flow
P_{T2}	pitot pressure
P_V	viscous induced pressure
$(Pr)_{FR}$	"frozen" Prandtl number
Q	capacitor bank energy
$\dot{q}_s$	stagnation heating rate
R	resistance; radius of curvature; gas constant
Re	Reynolds number
Re_ℓ	Reynolds number based on shock wave–interface separation distance
RE	reflected driver expansion
RS	reflected shock wave
$\frac{S}{R}$	entropy, dimensionless
St	Stanton number
T	absolute temperature
t	time
U	gas velocity
$\bar{u}$	gas velocity relative to shock wave
V_S	shock wave velocity
V_{ST}	shock wave velocity for tailored interface
v	volume
x	distance along axis
Z	$(1 + \alpha)$

α	dissociation mass fraction
γ	ratio of specific heats
δ_i	half-angle of starting cone
η	energy transfer efficiency
μ	dynamic viscosity
ρ	gas density
τ	duration of steady pressure in a reservoir
τ_D	flow drainage time
τ_R	flow residence time
τ_V	characteristic vibrational excitation time

Subscripts

D	driver tube
DT	driver tube
d	based on diameter
f	final value
H	referenced to heat transfer
i	initial value; driver condition before heating
N	ambient condition or location in nozzle
n	referenced to model nose section
P	referenced to pressure
RT	response time
S	shock wave
T	reservoir condition
Th	theoretical value

TS	test slug
w	wall condition
1	ambient condition in driven tube
2	behind incident shock wave
3	behind incident contact surface
4	driver condition after heating
5	behind reflected shock wave
∞	free stream in nozzle

Superscripts

*	sonic flow
( )′	effective driver conditions after expansion from A_4 to A_1

DESIGN AND PERFORMANCE OF THE AMES ELECTRIC-ARC SHOCK TUNNEL

John O. Reller, Jr.

Ames Research Center

SUMMARY

A high enthalpy shock tunnel using arc-heated helium as the driver gas has been designed for gasdynamic research at total stream energies from 7,000 to 35,000 J/g. The arc driver was found to be a relatively efficient energy converter. Tailored shock Mach numbers from 11.5 to 14.6 in air were demonstrated. A nozzle calibration with a total stream enthalpy of 18,600 J/g of air gave test times of 1.5 to 2.0 msec at flow Mach numbers from 16 to 24.

INTRODUCTION

With the advent of extraterrestial flight and with the increasing sophistication of interplanetary probes, a substantial portion of the research effort in the aeronautical sciences has been directed toward high-temperature reacting gasdynamics. For many reasons, this discipline often has been advanced more rapidly theoretically than experimentally. Thus, while numerical methods of investigating gasdynamic reactions at elevated temperatures have improved rapidly, generating similar conditions in the laboratory has become increasingly difficult. A prime source of information on the kinetics of gas reactions is the shock tube and, in successive improvements over several generations, it has continued to produce results of vital interest. In general, however, these results relate directly to the basic physical chemistry of a rapidly heated gas in that they may identify the path and/or verify the predicted rate of energy exchange. In one sense, these results serve to implement or quantify the gasdynamic theories that apply to flow about bodies moving at high velocity through planetary atmospheres. Beyond this, there has been extensive simulation in the shock tube of flow in the stagnation region of blunt bodies at equivalent flight speeds up to 18 km/sec.

The application of the shock-tube method to a more complete simulation of high-velocity atmospheric flight has proved more difficult than anticipated and has proceeded at a slower pace. To achieve representative Mach numbers, the shock-heated gas must be expanded to a lower temperature by increasing its velocity, usually in a supersonic nozzle. The extent of nozzle expansion is determined by the type of simulation desired, that is, is Mach number the sole criterion, or are stream static pressure and velocity to be at realistic values? A summary of much of the recent work in hypersonic similitudes is found in reference 1, where it is adequately demonstrated that duplication of flight velocity is of primary importance for simulating body flow fields of reacting gases.

The primacy attached to velocity duplication, along with the need for relatively high Mach numbers ($\geqslant 10$) for flow similitude over slender bodies, means that stream total enthalpies must equal flight values and that relatively large flow expansions are required. In the development of the

present facility, it was decided to use a reflected shock reservoir with the tailored-interface restriction to obtain a range of reservoir enthalpies. This decision implies an upper limit to total enthalpy (and stream velocity) determined by radiation losses from the quiescent reservoir gas. Previous experience in a facility of this type showed that this limit was not encountered at incident shock velocities up to 3 km/sec (ref. 2).

The criterion of a tailored interface has dual significance; first, this condition theoretically minimizes the time required to achieve a steady reservoir pressure by virtue of the wave processes in the tube and, second, it is a boundary condition beyond which mixing of driver gas with test gas is promoted by instability (into the test gas) of the gaseous interface. Either factor could be critical, since typical test times in shock-driven facilities are of the order of a few milliseconds. To set up the tailored-interface condition with shock speeds of interest – above 3 km/sec – a hot driver gas of low molecular weight is necessary, as the results of reference 3 demonstrate. Thus, to provide a high-temperature driver that could be varied readily in temperature to match the desired test enthalpy in different test gas mixtures, an arc-discharge heating cycle was chosen.

The following sections describe the design and operating features of the Ames electric-arc shock tunnel, including the performance characteristics of the driver and shock tube, along with a preliminary calibration of the expanded nozzle flow.

DESIGN OF FACILITY COMPONENTS

Energy Storage and Delivery Systems

The shock-driven wind tunnel is a device that creates a high-velocity stream of test gas large enough for detailed model studies but of short duration. When stream velocities greater than 4.5 km/sec are desired, the choice of driver designs is severely restricted by the high temperatures required, and arc-discharge heating becomes attractive. The design reservoir enthalpy of 29,000 J/g (equivalent stream velocity 7.6 km/sec) requires a driver temperature of at least 4500° to 5500° K. In addition, as will be shown later, driver length is a critical factor in shock-tunnel operation. Extrapolation of existing pressurized arc data indicated that driver lengths up to 3 m would be possible with a potential of 40 kV.

Capacitor bank– In the design of this system, a rapid energy pulse was assumed desirable to minimize energy losses to the containing walls of the driver; thus a low-inductance energy source was specified and a discharge time of 100 μsec was sought. These factors (high temperature, arc length, and rapid discharge) were the primary performance parameters for design of the system.

The end product is a fused storage bank of 180 capacitor units each rated at 27.5 μF and 20 kV, arranged in series-pair groups of 18 units for the delivery of energies from less than 5×10^4 to 1×10^6 J at potentials variable to 40 kV. The rating of the capacitor units requires that all discharges be at least critically damped to avoid voltage reversal. Units are fixed in a bolted aluminum rack mounted on 95 kV standoff insulators to permit rack potential to rise to 20 kV during the charge cycle (assembly is shown in fig. 1). The RG–17 transmission cables connecting the storage bank to the collector ring are roughly matched to the resistance and inductance of the driver arc to provide the most rapid and complete discharge possible, with minimum energy loss

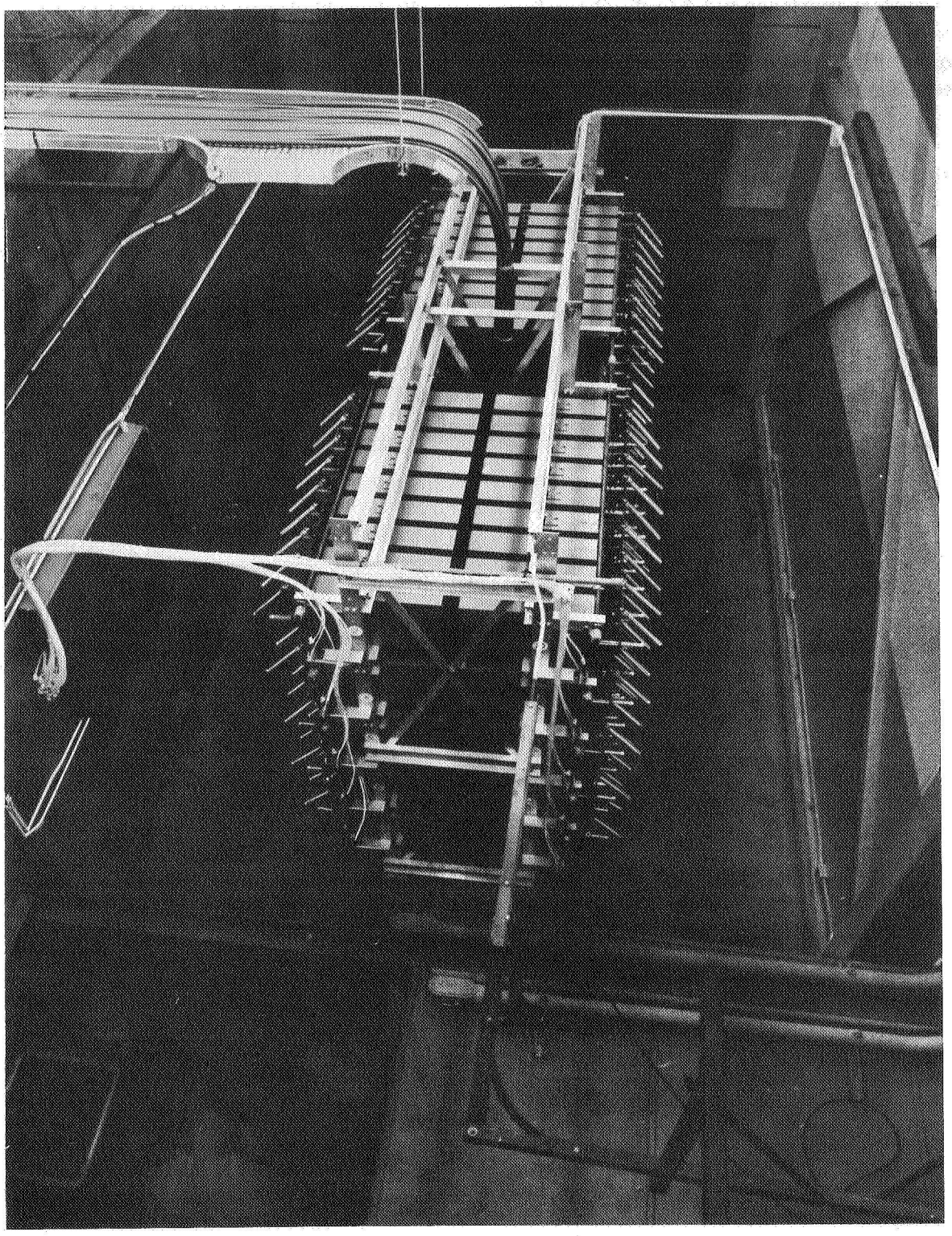

Figure 1.— Top view of 1-MJ, 40-kV capacitor bank.

external to the driver chamber. Total system inductance exclusive of the load (arc) is 0.25 μH and the system resistance is 1.87 mΩ. Since for a nonoscillatory discharge $R \geqslant 2\sqrt{L/C}$ the minimum resistance of the system plus load must be about 28 mΩ; with arc inductance, this value is slightly higher. Thus, the resistance of the arc discharge is critical and must exceed 26 mΩ. A detailed description of the energy storage system and its operating characteristics is given in reference 4.

Collector assembly and discharge chamber– The current collector and arc chamber are shown schematically in figure 2 and the overall electrical circuit in figure 3. The collector ring consists of

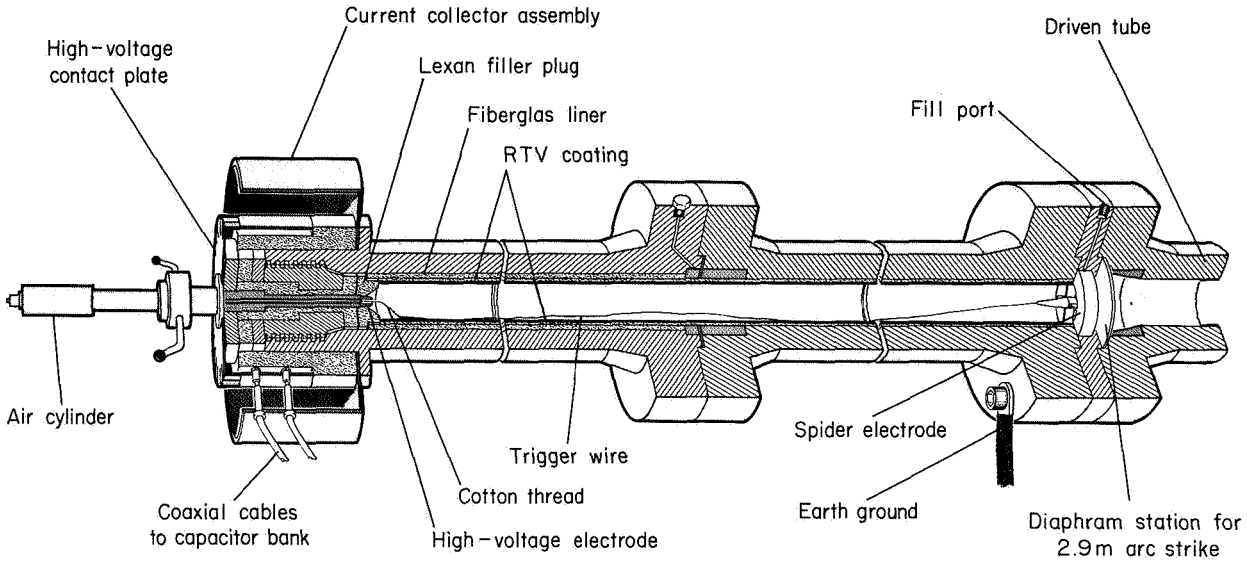

Figure 2.– Driver assembly.

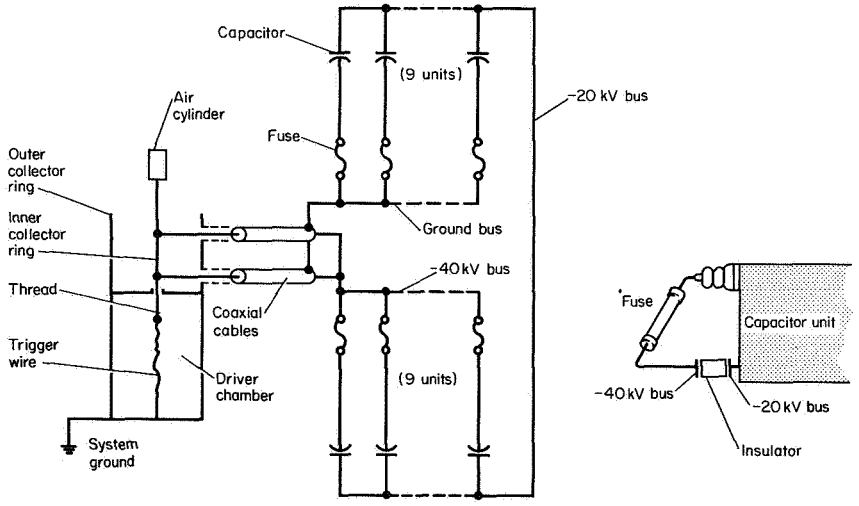

Figure 3.– Schematic diagram of one row of 18 capacitors in series/parallel; total bank of 10 rows, 180 capacitors, and 20 RG-17/u coaxial cables.

two coaxial copper cylinders; the outer, flanged to the driver tube, is electrically grounded, while the inner is connected by a copper spring contact plate to the main electrode. When this contact plate is removed, the entire electrode assembly can be "hipot" tested to rated voltage; this is normal practice before initiating the bank charging cycle and has frequently disclosed critical leakage paths. The electrode assembly is supported by a steel breech plug for pressure loads and insulated by a Teflon element.

The high-voltage electrode has a hollow core through which a brass rod extends back to the piston of a pneumatic solenoid (air cylinder) which actuates the trigger. The trigger switch is simply a short length of cotton thread connecting the sliding rod to the trigger wire which extends the length of the chamber to the ground electrode. When the slack wire is drawn to the high-voltage electrode, the arc discharge is initiated. (see ref. 4 for more details).

The arc chamber is designed for a pressure of 1000 atm and fabricated of a nonmagnetic stainless steel (A286) in two sections. An insulating liner of filament-wound fiberglas with a bonded inner layer of silicone rubber forms the inner wall of the chamber. This liner is surprisingly durable and can be reused many times; techniques have been developed to replace the rubber inner layer as often as required.

Instrumentation– Voltage and current wave forms are recorded for each discharge. Voltage buildup on the rack structure (capacitor midpoint) is relayed by a resistive voltage divider to a chart recorder, while discharge voltage is relayed by a capacitive voltage divider and an attenuator probe to the recording oscilloscope. Arc current is measured by monitoring the voltage drop across one pair of RG–17 cables, from the downstream driver flange to the capacitor rack. Since all cables are exactly the same length, each pair carries 1/10 of the total current; a voltage divider across the shunt cables reduces the signal for input to the recording oscilloscope.

Driver Tube

The arc-heated driver tube can be viewed as an energy convertor, changing electrical into pressure and temperature energy, which serves as the connecting link between the energy source and the test-gas generator. As such, its design must match (and, in part, determine) the electrical characteristics of the capacitor bank and the desired gasdynamic performance of the shock tube. From the former, the important parameters are the energy available and the length of arc that can be drawn.

Gasdynamic requirements– The choice of a reflected-shock wave, tailored-interface mode of operation for this facility, combined with the necessity of steady reservoir conditions of sufficient duration to establish supersonic flow in a relatively large nozzle, to establish steady flow over a sizeable test model, and to provide a test period for aerodynamic measurements, serves to fix the driver length and temperature. Consider first the temperature requirements. With helium as the driver gas, the variation of driver temperature with tailored shock Mach number is shown in figure 4 for several test gases. The index mark on each curve represents a design total enthalpy (in the shock-tube reservoir) of 29,000 J/g. Thus, for real air, the required driver temperature is about 4200° K; the small effect of pressure level, through variation of P_2, has been neglected here. It is obvious that the required temperatures are well in excess of those available by other methods of heating.

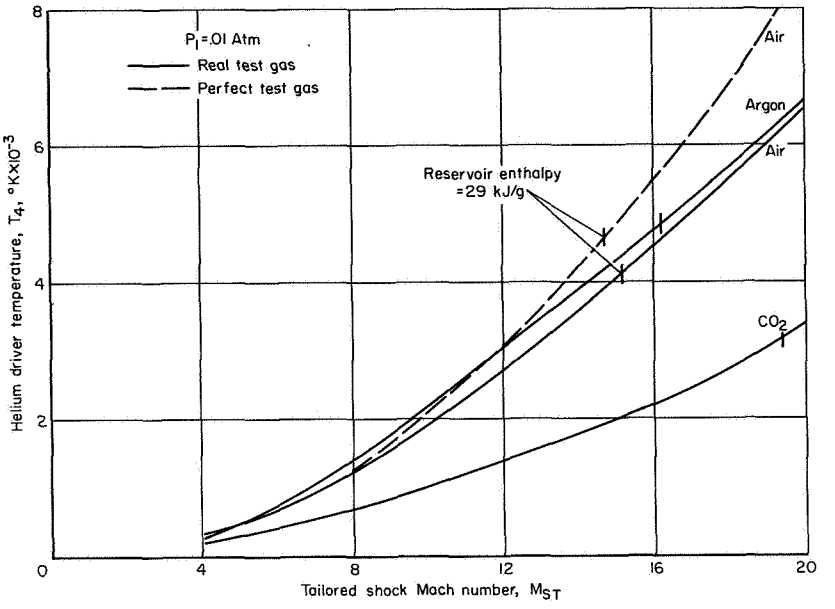

Figure 4.– Driver temperatures required for interface tailoring in several gases.

In a constant-area shock tube, where the driver and driven tubes have the same diameter, the length of the driver can be related in simple fashion to the duration of steady-state conditions in the reservoir. Ideally, the tailored-interface condition is first disturbed by the arrival of an expansion fan reflected from the closed end of the driver chamber. While this event is not independent of shock-tube length, it has been shown (e.g., ref. 3) that an optimum ratio of shock-tube length to driver length exists for which the time is maximized. The variation of driver length with M_{ST} is shown in figure 5 for this optimum length ratio, along with a sketch of the wave diagram showing the triple intersection point of the optimum condition. Since the figure is for $\tau = 1$ msec, and driver lengths of 2 to 2.5 m are indicated at the design condition, the critical importance of driver length is

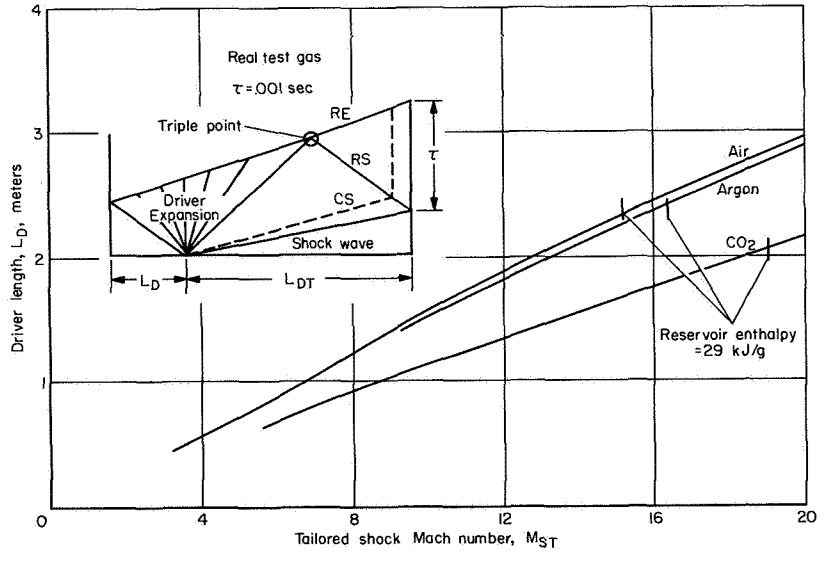

Figure 5.– Optimum driver length for maximum test time.

apparent. The term τ varies directly as L_D and nearly inversely with M_{ST}; steady-state reservoir times range from 1 to 3 msec at best, based on the projected maximum arc length of 3 m.

The design pressure of the driver chamber is perhaps less critical than either temperature or length, since the total enthalpy and steady-state time in the shock-tube reservoir are nearly independent of reservoir pressure. However, in general, the reservoir pressure and driver pressure should be as high as possible to afford the widest latitude in flow-scaling parameters for aerodynamic testing in a nozzle. In particular, the Reynolds number and the binary scaling parameter ρR (for dissociating diatomic gases) are difficult to duplicate. In the present case, the constraints of available energy and test time (driver length) serve to determine the maximum driver pressure. Ideally, for constant volume heating,

$$T_{4i} = P_{4i} = 1 + (\gamma_i - 1)\frac{\eta Q}{\nu P_i} \tag{1}$$

where ηQ is the energy supplied to the driver. Thus, while T_4 varies widely with P_i, P_4 is relatively constant. Figure 6 illustrates this behavior for an energy addition of 10^6 J and for a range of intial pressures from 7 to 40 atm. Now, from reference 4, at driver initial pressures above about 35 atm, it was not possible to draw an arc over a length of 3.0 m with a potential of 40 kV. With this information as a guide, along with the temperature and length requirements developed above, the ideal driver pressure ranges from 350 to 450 atm for diameters between 8 and 10 cm.

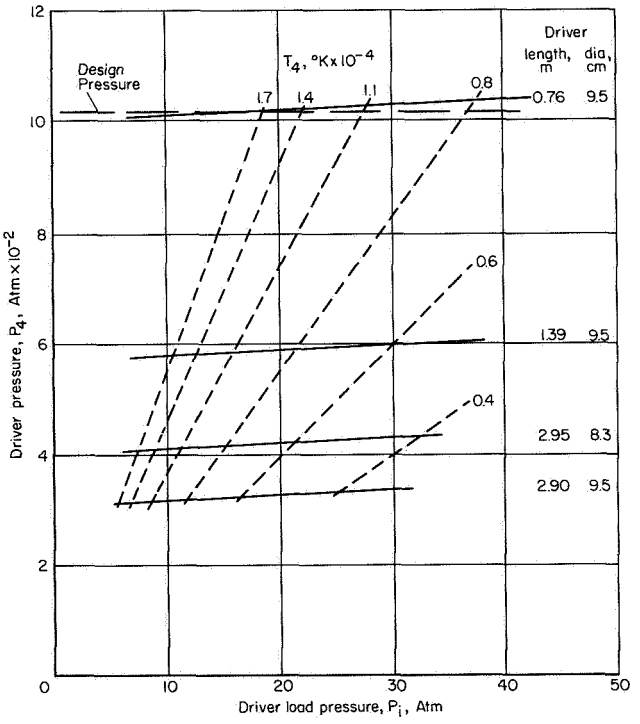

Figure 6.– Driver performance map, ηQ = 1 MJ.

The driver mechanical design pressure was actually set at 1000 atm, primarily to allow use of the tube in sections as short as 76 cm (see fig. 6) and also to allow for growth potential.

The results of this study are summarized as follows: An arc-heated shock-tunnel driver was designed to match a capacitor bank storing 1 MJ of electrical energy, and to provide a tailored-interface reservoir of test gas at an enthalpy of 29 kJ/g. A driver length of 3 m was chosen as the minimum size to provide a usable test period and, in turn, this length was determined to be the projected maximum arc that could be drawn with a 40-kV potential. The inside diameter of the driver was set at approximately 10 cm, which provides pressures up to 340 atm for driver temperatures from 3500° to 8500° K.

Shock-tube application– The driver chamber of a high-velocity shock tube must operate at very high pressures and temperatures but does not have the length requirement of a shock-tunnel driver. A single parameter – energy density (energy per unit volume) – can be used to predict the range of shock velocities obtainable. This is shown in figure 7, where the dashed lines indicate

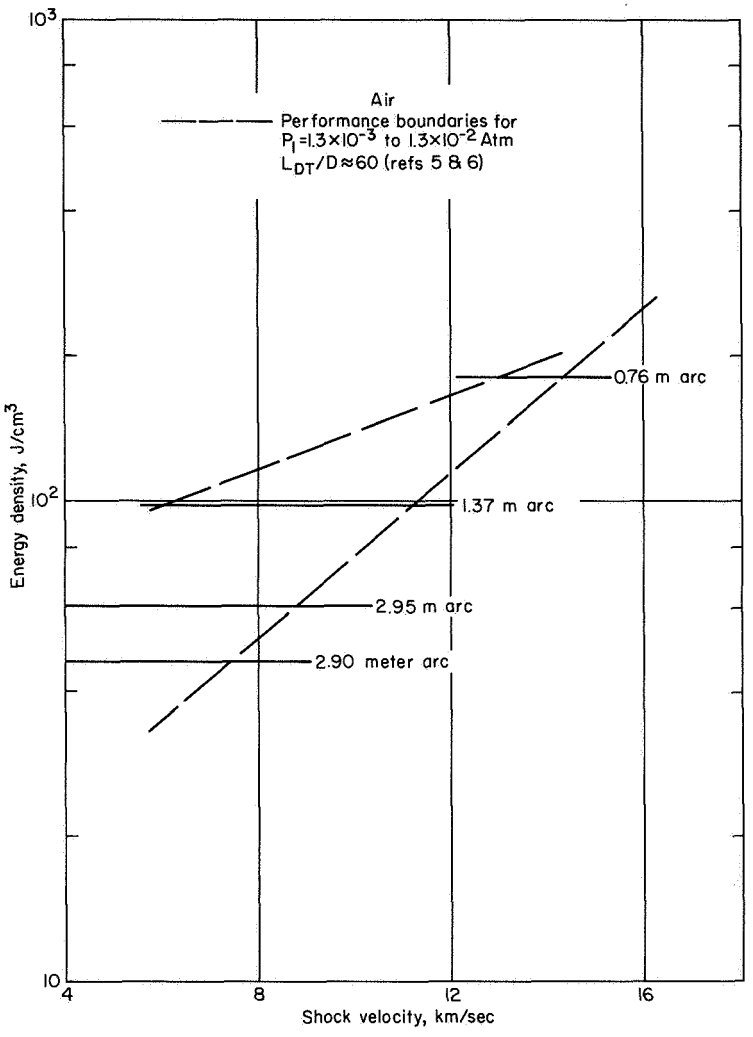

Figure 7.– Estimated shock velocities in shock-tube mode of operation, Q = 1 MJ.

approximate velocity boundaries at a given energy density (from the results of refs. 5 and 6). The relatively long shock-tunnel drivers of the present design are limited to velocities below 9 km/sec. Therefore, to accommodate future shock-tube investigations, the driver was fabricated in two sections, one of which provides a 1.37-m arc chamber that can be shortened to 0.76 m with a plug insert. By this means the energy density can be raised from 45 to 185 J/cm^3 and the maximum velocity potential to 14 km/sec or more. The corresponding driver pressures and temperatures are shown in figure 6.

Primary diaphragm— The design of the primary diaphragm is conventional. Twenty-three-centimeter discs of fully annealed, type 304 stainless steel are used; surfaces have a commercial bright finish. Material properties and dimensions are carefully specified and each lot must be taken from a single heat. Surfaces are protected from damage during machining, shipment, and storage. The upstream-facing surface is grooved at 90° for 15 cm, at 45° to the grain of the metal, with a cutter having a 90° included angle. The depth of groove is controlled to within 0.08 mm and at the bottom the radius is between 0.13 to 0.38 mm. The diaphragm is pin-located, secured by clamping against serrations machined into the face of the upstream flange, and sealed by O-rings (fig. 8). It opens into the square end of a transition insert to minimize tearing at the base of the petals and to insure full opening without projecting corners or edges. Grooves are positioned in line with the support legs of the spider electrode since this orientation appears to give the best results. Diaphragms are available in thicknesses from 1.5 to 5.0 mm and with groove depths from 10 to 70 percent. The best configuration for each test condition is determined by experiment; the results will be discussed in a later section.

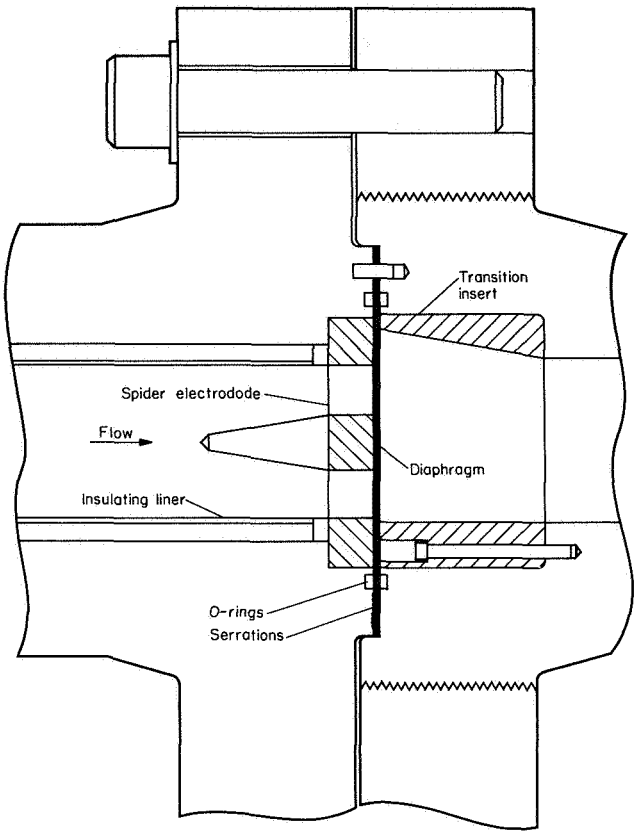

Figure 8.— Main diaphragm arrangement.

Shock Tube

The design of the shock-tube portion of the facility, as for the driver chamber, is predicated upon its use to develop a reflected-shock reservoir of test gas of sufficient quantity and duration to supply a large supersonic nozzle. As mentioned in the Introduction, the conditions of interest are at primary shock velocities greater than 3 km/sec, since other methods of heating a driver gas are more effective below this value.

Gasdynamic considerations— The primary consideration that influences the choice of shock-tube diameter is the reservoir pressure. As mentioned earlier, this pressure should be as high as possible for shock-tunnel application. To achieve this objective, within the constraints imposed by a turbulent boundary layer on the tube wall and the required range of shock velocities, the shock-tube diameter was chosen to be 10.16 cm (4.00 in.), approximately the same as the driver.

The maximum pressure in the shock-tube reservoir is determined by the driver pressure and by the initial pressure loading required for tailored-interface operation at any given shock velocity. This

is illustrated in figure 9 where both the reservoir pressure and enthalpy are shown as a function of M_{ST} for air, CO_2, and argon. The ideal driver pressures for the 2.90-m arc driver (taken from fig. 6) have been used. The index marks on each curve bound the region of interest, from $V_{ST} = 3$ km/sec at the lower end to $H_5 = 29$ kJ/g at the upper. Reservoir pressures are relatively constant with M_{ST} for any test gas and vary between 240 to 410 atm for this particular driver. For the 2.95-m driver, the values are about 30 percent higher, and for the 1.37-m driver, about 80 percent. To accommodate these latter driver configurations, the design pressure of the tube was fixed at 600 atm. This value was applied over the entire length of the tube to allow for high pressures behind the upstream-propagating reflected shock wave and for different reservoir locations.

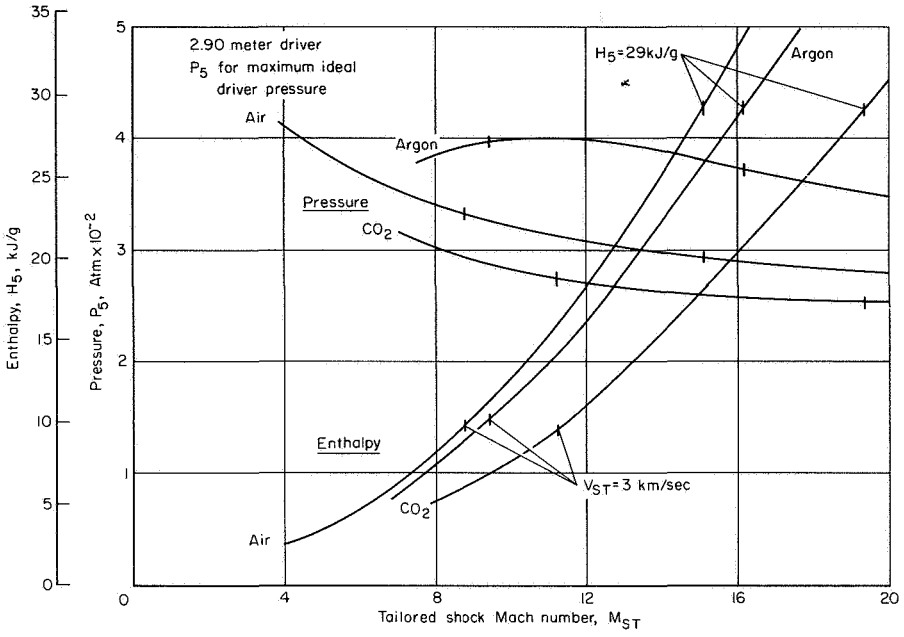

Figure 9.– Reflected shock pressure and enthalpy for tailored conditions.

The length of the shock tube can be optimized, with respect to steady-state reservoir time, for each different test gas and tailored reservoir condition (ref. 3). This was illustrated in figure 5 where the triple-point intersection of the reflected shock wave, the leading edge of the primary driver expansion, and the initial wave of the reflected driver expansion defines the optimum length ratio. This length ratio is plotted in figure 10 as a function of M_{ST} for the same three gases and for an initial pressure of 0.01 atm; the typically small pressure dependence is shown only for air. Tube lengths one to five times the driver length are indicated with real-gas values considerably greater than those computed from perfect-gas relations. This result implies that the facility design should allow for considerable variation in overall length as, for example, in the placement of the vacuum pumping system. However, at least two other factors must be considered before the shock-tube length can be fixed – shock attenuation and test-slug length. These two are opposing factors with the first showing improvement as tube length decreases and the second as the length increases. Experience shows (see, e.g., ref. 5) that shock-tube lengths greater than 120 to 150 tube diameters (in the present case from 12 to 15 m) will incur large shock-wave attenuation. On the other hand, the length of the relatively quiescent slug of test gas in the reservoir is, in practice, influenced by the shock wave interface behavior before and after shock reflection and is always less than the ideal

value. For these design estimates, the ideal slug length is shown in figure 11 as a function of tube length, along with the variation of steady reservoir time at several values of M_{ST}. Driver length L_D is 3 m and initial pressure of test gas (air) is 0.01 atm; the circle symbols indicate the optimum tube lengths obtained from the length ratios shown on the previous figure. Now, it is obvious that tube lengths less than optimum are not desirable, and that greater lengths pose a compromise between slug length (available volume of test gas) and time. The maximum L_{DT} (as defined in ref. 3) should be avoided since steady time is at a minimum, which could well be marginal compared to nozzle

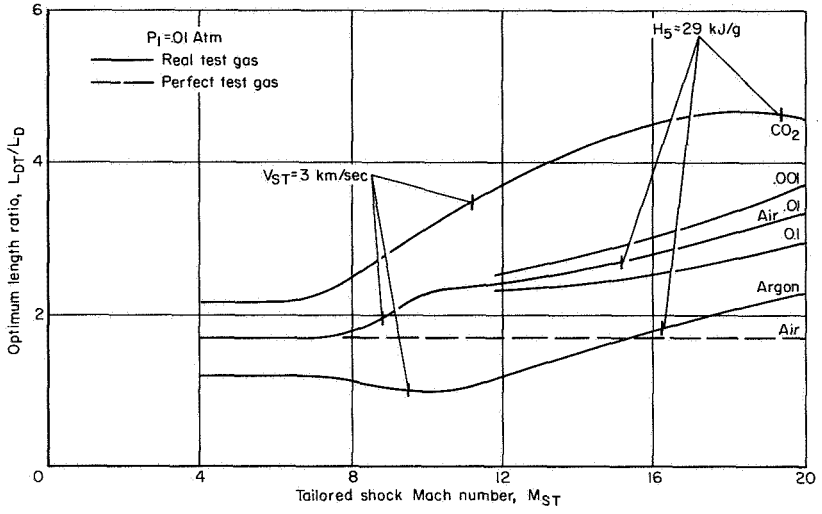

Figure 10.– Optimum ratio of shock tube to driver length.

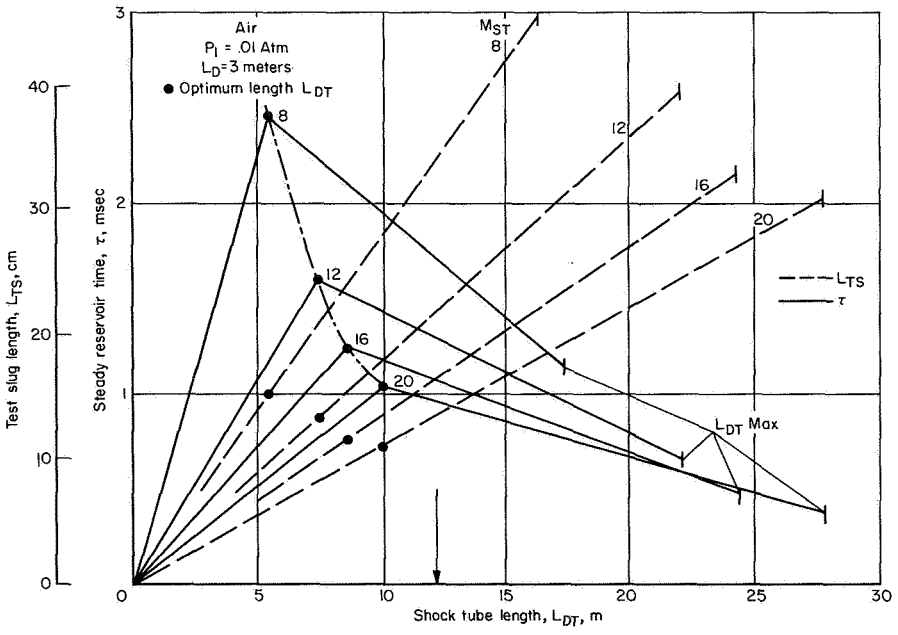

Figure 11.– Test slug length and steady reservoir time for ideal conditions.

starting transients and the response time of instrumented models.[1] Thus, since slug length increases more rapidly than steady time decreases with tube length, a practical compromise is reached at a nominal value of 12 m, long enough to include the optimums over the operating range of interest, but not long enough to reduce steady reservoir time appreciably.

A similar exercise for CO_2 and argon as test gases indicated tube lengths of 15 and 7.5 m, respectively.

Instrumentation– Conventional pressure gages can be used to control the evacuation, flushing, and loading of the shock tube with the desired test gas. Bourdon-tube gages are accurate at pressures down to 0.01 atm and a variable-capacitance diaphragm cell at pressures as low as 10^{-5} atm, for most gases. Ionization gages are used to monitor evacuation and leak rates.

An important source of spurious signals is the electrical noise generated during the normal operating cycle of the energy storage system, by the functioning of various high-voltage relays and by the arc discharge process. Interference with instrument circuits is minimized by an inhibit function (delay or blanking) that provides isolation until the arc discharge is completed, at which time it is removed by a high-level trigger pulse. Figure 12 is a schematic diagram of the delay and trigger arrangement used with the shock-velocity system. The Master Start Source (MSS) consists of a low-frequency bandpass filter, a threshold level detector and a low-impedance pulse circuit; input to the MSS is from a voltage divider across the ground return to the capacitor bank. When the divider sees a voltage equivalent to an arc current of $6X10^4$ amp, the unit produces a 50-V signal. This start signal, in turn, triggers a 6-channel time-delay device that provides separate and isolated pulses with adjustable delay from 10 to 10^4 μsec. Each delayed single pulse is a positive 50 V into a 50-Ω load for 4-μsec duration.

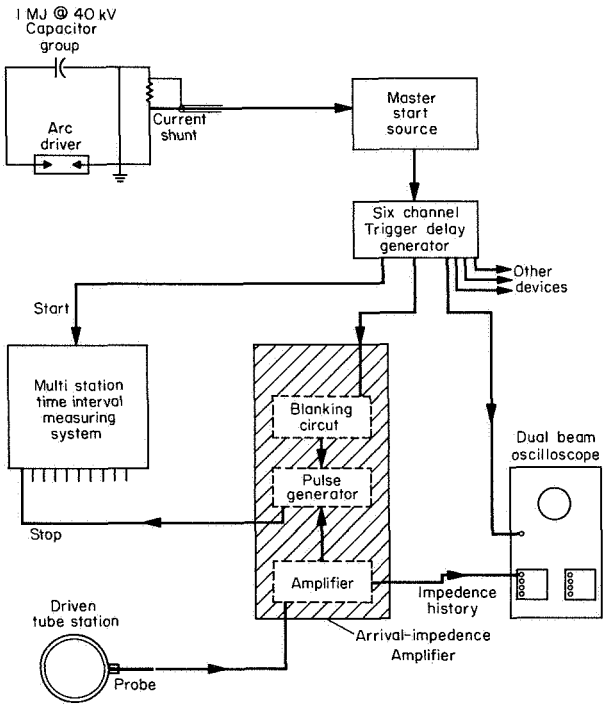

Figure 12.– Block diagram of trigger system.

The shock velocity measuring system consists of a biased, twin-electrode probe with a signal amplifier (ref. 7) at each measuring station (intervals of 1.22 m along the tube) feeding into a time-interval console having 10 independent counter-display channels. The console circuitry was designed for positive reset of all counters at the end of the delay period and is protected from transient noise by buffered trigger circuits. Each counter is

[1]Maximum L_{DT} is that length for which the reflected shock-wave and reflected driver expansion interect at the contact surface to give a minimum value of τ, consistent with the tailored-interface concept.

stopped by one probe amplifier signal and the circuit is locked out until manually reset. Shock arrival times up to 10^4 μsec can be recorded with a resolution of ± 0.1 μsec. With this counting accuracy, the residual error in velocity measurement is due to probe response and electronic signal conditioning.

Nozzle and Test Section

Among the factors considered in the design of the driver and driven tubes, none was more critical than wave propagation time. A steady reservoir condition can be obtained, in theory, for times of 1 to 2 msec for the range of total enthalpy of interest. It follows that the test gas must be expanded through the nozzle in the most effective way possible if there is to be any useful test time. The first implication is that the nozzle should be as short as possible to minimize the "starting transients." Conversely, as nozzle diameter is increased the usable test core increases and larger more detailed models can be accommodated. The required compromise is outlined in the following sections.

Flow drainage time– Consider first the time it takes for the reservoir test slug to flow through the nozzle sonic throat. With the ideal slug lengths of figure 11 and a shock-tube length of 12 m, the flow drainage times, τ_D, are obtained as a function of throat diameter (fig. 13); τ_D is relatively long by comparison with the steady reservoir time τ from shock-tube performance (fig. 11). Even with a factor of 2 allowance for less than ideal slug lengths and interface mixing (to be discussed later), as shown by the dashed line in the figure, throat sizes up to 2 cm appear reasonable. Design values of d^* are shown (filled symbols) on three of the M_{ST} curves; these were chosen to give static temperatures of about 200° K and flow Mach numbers equivalent to flight Mach numbers having the same total enthalpy. Flow drainage time appears more than adequate for these conditions, that is $\tau_D >> 2\tau$.

Figure 14 is a sketch of the nozzle throat assembly. The nozzle insert is of copper and is fastened into the stainless steel end plug that is clamped into the shock tube by the nozzle hub and flange. A stainless steel end plate serves as the reflecting surface for the incident shock wave and holds the plastic nozzle diaphragm in place. Throat diameter is varied by changing the internal contour of the nozzle insert and allowing dimension B to vary. Dimension A, the distance from the end plate to the instrument port, varies from 2.67 to 6.10 cm with increasing d^*.

Nozzle starting time– When the flow in a supersonic nozzle is started impulsively, a certain time must elapse before a steady expansion is achieved. In the general case, the transient flow pattern closely resembles a shock-tube flow, with an incident shock and an interface, followed by an unsteady expansion. In addition, there may also be a secondary upstream-facing shock wave embedded in the unsteady expansion. This rather complex behavior has been the subject of several investigations in recent years (e.g., refs. 8–11). While the solutions of Smith and Laval (ref. 9 and 10) are reasonably exact, they have been applied only to small nozzles and ideal gases. In the present study, therefore, two of the more approximate methods will be used to survey parameters and establish limiting conditions. First, Chisnell's method (ref. 11) with be used to locate the incident shock wave since Ackroyd (ref. 8) found good agreement between this method and his experiments over a wide range of initial pressures. Second, Smith's suggestion (ref. 9) is used – that $(U-a)$ for steady flow is less than for unsteady and that, therefore, the former value will define the earliest time at which steady flow can exist in a nozzle.

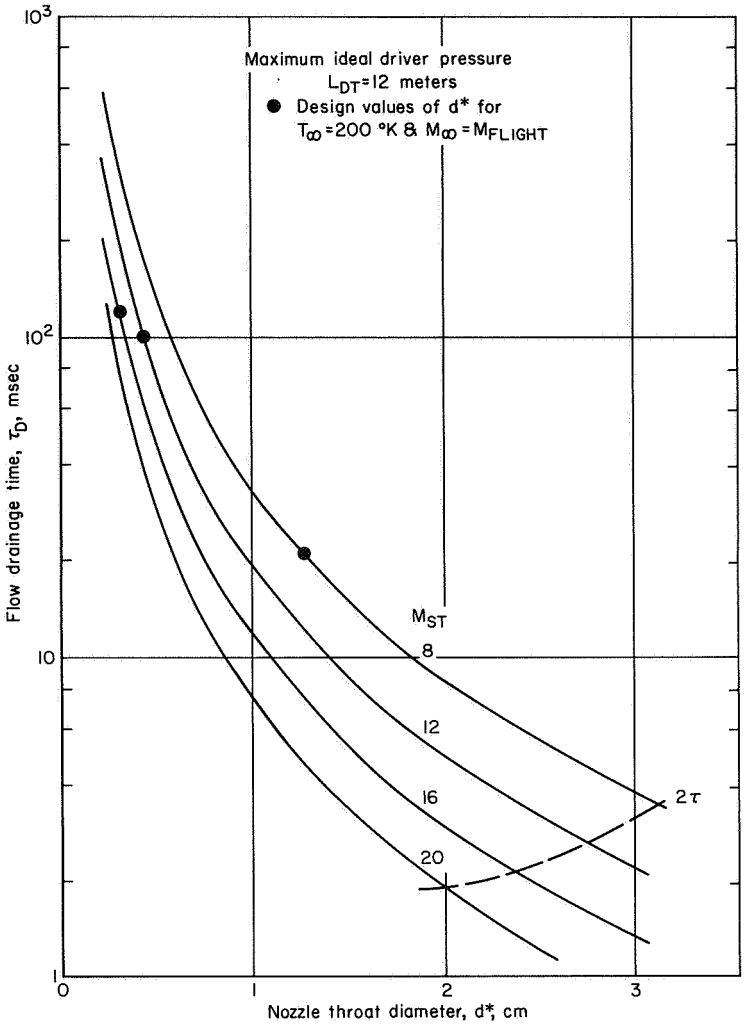

Figure 13.– Ideal flow drainage time.

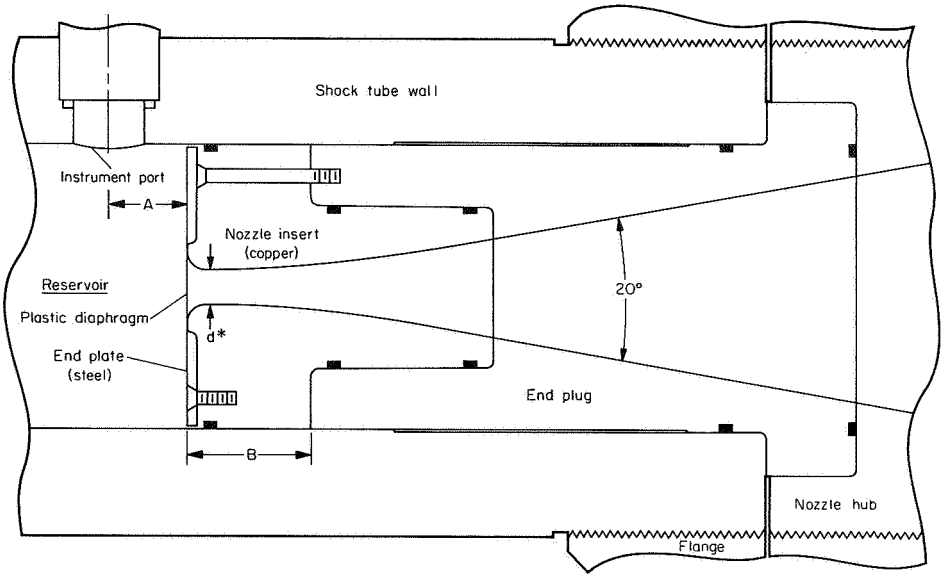

Figure 14.– Sketch of nozzle throat assembly.

The results are shown in figure 15 for two values of d^*, a nozzle half-angle of 10°, and for an intermediate enthalpy corresponding to $M_{ST} = 12$; time (in msec) is plotted as a function of distance along the nozzle centerline from the sonic throat. Observe first the solid curves which are the Chisnell solution for the incident shock wave. This solution originates at the sonic throat where the shock strength, following Ackroyd, can be evaluated as for a shock tube with an area reduction at the diaphragm. Thus, in the present notation,

$$\frac{P_5}{P_N} = \frac{P_{2N}^*}{gP_N}\left[\left(1-\frac{a_N}{a_5}\right)\left(\frac{\gamma_5-1}{2}\right)\left(\frac{U_{2N}^*}{a_N}\right)g^{\frac{-(\gamma_5-1)}{2\gamma_5}}\right]^{\frac{-2\gamma_5}{\gamma_5-1}} \tag{2}$$

where P_5/P_N is the pressure ratio (after shock reflection) across the plastic diaphragm at the nozzle entrance and P_{2N}^*/P_N is the pressure ratio across the incident shock wave at the nozzle throat, with air as the nozzle gas. The factor g is the "equivalence factor" of Alpher and White which is a function of A_5/A^* and γ_5. Real-gas values of P_{2N}^*, U_{2N}^*, and γ_5 were used. With M_{SN}^*, the shock Mach number at any downstream location in the nozzle can be approximated by

$$M_{SN} \approx \left\{\frac{(M_{SN}^*)^2-1}{(A_N/A^*)^{0.4}}+1\right\}^{1/2} \tag{3}$$

where the exponent on the area ratio is for strong shock waves in a diatomic gas (ref. 11). In the first part of figure 15, for a nozzle throat diameter of 0.45 cm, the effect of reservoir pressure and initial nozzle (test section) pressure on incident shock trajectory is shown; higher reservoir pressures and lower nozzle pressures are favorable. For a 75-cm exit diameter, with reservoir pressures from 50 to 300 atm and nozzle pressures from 10^{-6} to 10^{-5} atm, the shock transit time is about 0.9 msec.

Compare this result with estimates using Smith's (U–a) criterion, (dashed lines on the figure). His approximate expression for this conical nozzle

$$t = \frac{0.76\,d^*}{2a_T \tan 10^\circ}\left[M_\infty^{1/2}\left(1-\frac{1}{M_\infty}\right)+\frac{1}{15}\left(M_\infty^{3/2}-1\right)+\frac{1}{25}\left(M_\infty^{5/2}-1\right)\right] \tag{4}$$

involves the nozzle geometry, the speed of sound in the reservoir gas, and the exit Mach number for steady flow. Now, in a partly dissociated, expanding flow the exit Mach number will depend on the extent to which conditions depart from local equilibrium. With "freeze Mach numbers" (M_F) of 3 and 4 as approximate limits within which the real flow will fall, the above equation yields the valves shown in figure 15(a). At both limits, the time estimates are less than for the incident shock wave, except at small distances from the throat; for a 75-cm exit, the average is about 0.6 msec. This time

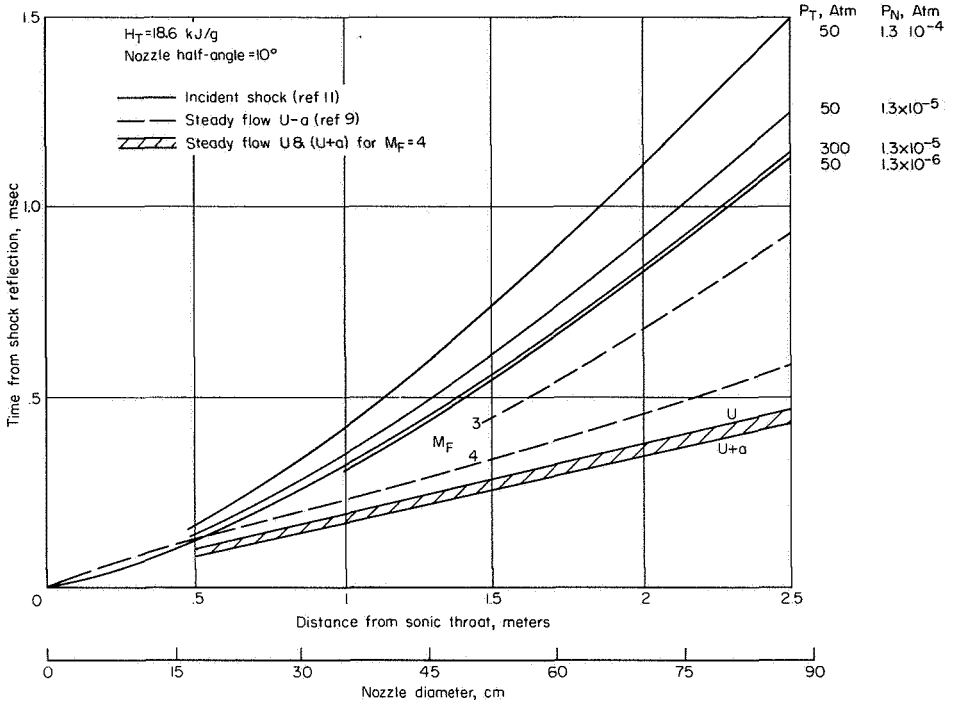

(a) $d^* = 0.45$ cm

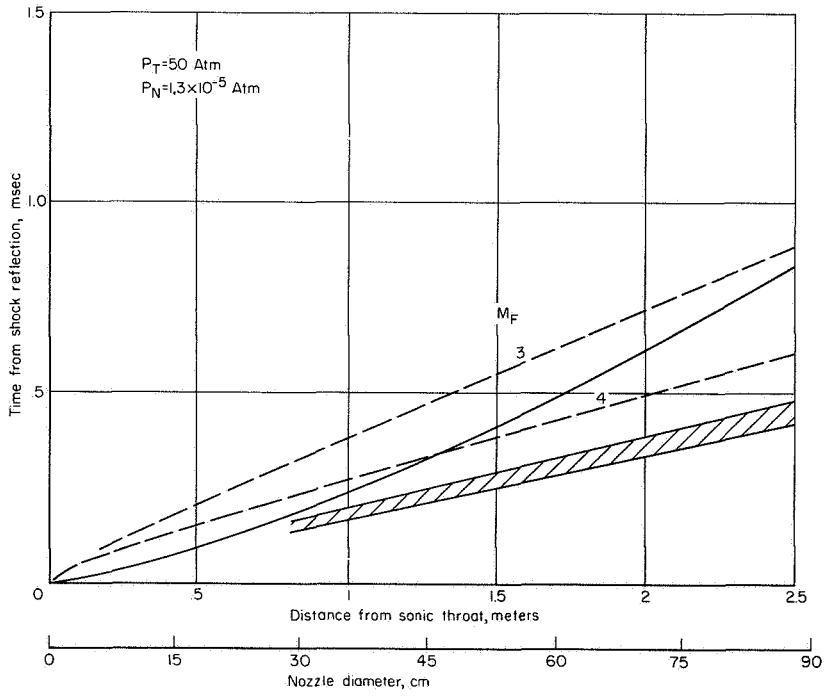

(b) $d^* = 1.27$ cm

Figure 15.– Estimate of flow starting time in a conical nozzle.

inversion of the two starting criteria is not unexpected and was, in fact, predicted by Smith for flows starting from very high temperature reservoirs. Under this condition, the entire starting process is dominated by the initial shock wave and the $(U-a)$ estimate does not apply.

It should not be overlooked that a nozzle has a "stopping time" as well as a starting time (illustrated in fig. 15 by the shaded band, where the upper boundary is the flow transit time from reservoir to exit and the lower is the transmittal time of a pressure signal $(U+a)$). Since both U and $(U+a)$ times are very closes, either a change in gas composition or pressure in the reservoir will be felt about 0.4 msec. later in a 75-cm nozzle. Therefore, the loss of test time in a nozzle is the difference between the starting and stopping times. In this instance, the difference should be slightly greater than that between the incident shock arrival and the $(U+a)$ signal; the uncertainty arises since the location of the upstream-facing shock wave is not known. However, if the initial nozzle pressure P_N is of order 10^{-6} atm, the second shock (if it develops at all) will be weak and will lie near to the incident shock. The resultant time loss in a 75-cm nozzle is estimated to be about 0.5 msec when $d^* = 0.45$ cm and $H_T = 18.6$ kJ/g.

A similar plot is shown in the second part of figure 15 for $d^* = 1.27$ cm. Here the $(U-a)$ values are more significant; nozzle time loss is only about 0.25 msec for a 75-cm exit diameter. These times are within reasonable bounds for the present design. It is readily apparent that initial nozzle pressure must be kept in the 10^{-5} to 10^{-6} atm range and that the combination of low reservoir enthalpy and small sonic throat diameter should be avoided. Any nozzle expansion with air or other test gas must be experimentally checked for nozzle loss time since the available methods of estimation are at best only approximate. Nozzle length must be limited on a facility of this type; in the present case, a 10° half-angle and a 75-cm exit diameter nozzle is about the largest that can be tolerated.[2] This size should accomodate models sufficiently large for most test programs.

Model flow start time– This process has been studied both in shock tubes and shock tunnels. In at least two cases of nozzle flow (refs. 12 and 13), steady flow was achieved on slender models at about the same time that steady nozzle flow was established; the two processes were nearly coincident. This behavior is advantageous in that the nozzle starting time serves a useful purpose. In a more quantitative sense, Rom (ref. 14) applied the unsteady flow analysis of Ihrig and Korst to wake flow measurements in a shock tube. He showed that pressures stabilized more quickly than heating rates, and attached flows more quickly than separated flows. Characteristic times for pressures and heating rates were defined as $t_P = L/a$ and $t_H = L/USt$, respectively, where St is the Stanton number, U local external velocity, a local speed of sound, and L a characteristic length.

The experimental work of Powers and his associates (ref. 15), again in a shock tube, yields approximate numbers for the heating-rate parameter in the form $t_H U_2/L$, where L is model length. For attached flow on a blunt model, $t_H U_2/L$ varied from 2 to 4, for a turbulent wake it was about 10, and for a laminar wake from 15 to 20. In the shock tunnel of reference 12, the times for laminar wake stability correspond to values of $t_H U_\infty/L$ from 14 to 17. Since these various results for shock tubes and shock tunnels appear rather consistent, the same concepts have been applied to the present design study (as shown in fig. 16). The first part of the figure presents flow starting time based on the pressure criterion $t_P = L/a$ as a function of local flow temperature; the second uses the heating rate time as $t_H = LK/U_\infty$ for characteristic K values of 3, 10, and 15, over

[2] Calculations indicate that the time loss can be reduced if the initial nozzle gas in helium. At 10^{-5}-atm initial pressure, the time loss for a 75-cm exit diameter is reduced by about 1/2, from 0.6 to 0.3 msec.

a range of stream velocity. The term U_∞ is used here rather than local external velocity for ease of comparison, and L should be interpreted as the model or flow-field length (as for wakes) in the stream direction.

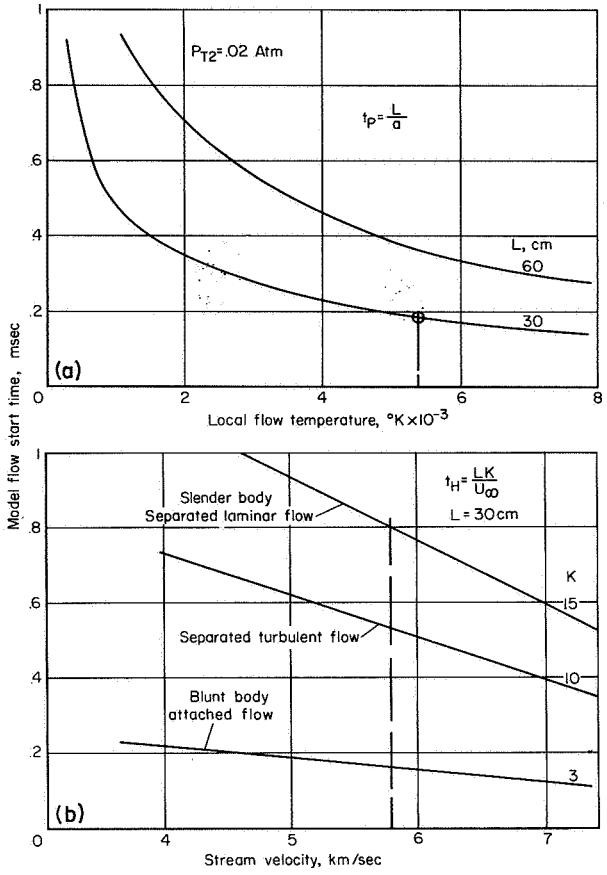

(a) Pressure model

(b) Heat-transfer model.

Figure 16.– Effect of gas properties on model flow starting time.

The results in figure 16 are considered to illustrate realistic trends and approximate values of flow transient times on models. Accordingly, pressures stabilize quickly when local flow temperatures are high, such as on a blunt body, but can take three to four times longer on very slender shapes where flow temperature approaches the stream value; intervals from 0.2 to 0.8 msec are indicated for a length of 30 cm. A similar sensitivity to model shape occurs for heating rates, with approximate limits set by the upper and lower curves shown on the figure. Presumably, slender bodies with attached flow would have K values between 3 and 10. The scale of time is roughly the same for heating rates as for pressures, although, in principle, the former should be greater; compare the times indicated by the symbols, which represent the stagnation region of a blunt body at one stream condition.

In comparing these results with the preceding nozzle analysis, it appears that flow starting times for models with a characteristic dimension of 30 cm can extend beyond the nozzle starting time. Even in the most optimistic limit, where the model time origin is assumed coincident with the arrival of the incident shock wave, it appears that only very blunt shapes with attached flow can adjust to steady state without a significant loss in test time. This finding apparently contradicts the results of references 12 and 13 mentioned earlier. With slender shapes and in wake flows, a significant loss of time may occur; thus, it is important to evaluate the process experimentally for the flow configuration, reservoir condition, and nozzle expansion of any proposed test program.

Transducer response and model design– A study was made of measuring techniques, transducers, and recording devices applicable to aerodynamic testing in the high-temperature, low-pressure, short-time environment of a highly expanded nozzle flow. Three areas were identified which could not be satisfied by simple extensions of present methods, namely, the measurement of very low pressures, force measurements, and multichannel digital recording. Before considering these, note that heating rates can be measured by well-known methods if certain design criteria are followed. Both thin-wall and thin-film technology are useful; in general, the thin-wall approach can be used where heating rates are relatively high. For example, a copper wall 0.125 mm thick has a

response time of about 60 μsec and, with a standard thermocouple sensor, can be used for rates from 10 to over 1000 W/cm^2. The lower limit is determined by the electrical noise pickup of the thermocouple circuit and the accuracy of the recording system. At lower heating rates, the thin-film gage is particularly useful because signal output is high and the temperature rise of the film is not excessive during the nozzle transient period, while response time is less than 10 μsec.

Model pressures are difficult to measure, not only because they are of low magnitude but also because transducers are both temperature-and acceleration-sensitive. (Now, for the time scale of the present design, it is readily apparent that the transducer must be located inside the model and very close to the measuring station; thus, transducer size is an important consideration.) The acceleration loading of a transducer has components from three sources – shock-generated accelerations transmitted through the model support system from tunnel structure, flow-starting accelerations applied directly to the model and support system, and acceleration of the transducer itself by sudden pressure application. The first was minimized in two design steps – by a slip joint at the nozzle exit to avoid direct transmittal of shock-tube accelerations into the test section structure (previous experience showed order-of-magnitude reductions) and by an acceleration damper in the model support system to reduce loads transmitted through the floor (fig. 17). The acceleration damper is a

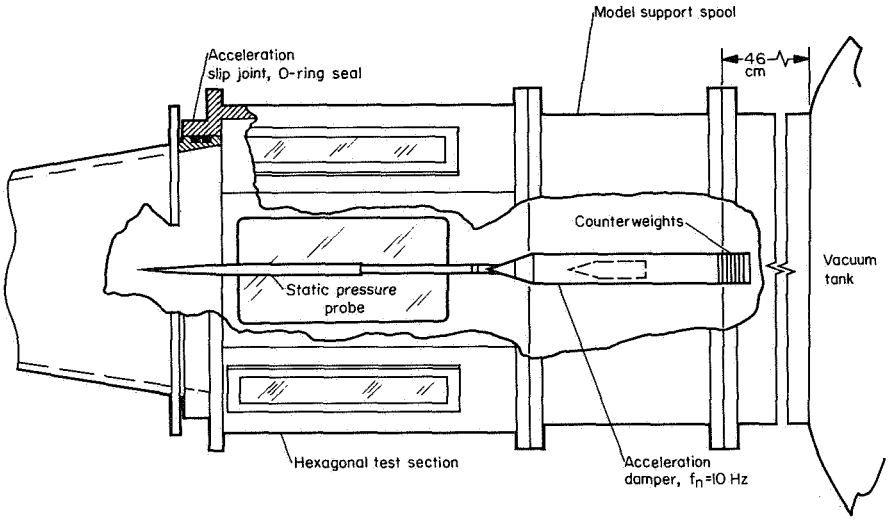

Figure 17.– Side view of test section.

mass of lead, spring-mounted to an internal member that is bolted to the horizontal support structure. Counterweights can be adjusted to balance the model weight and align it with the flow. The influence of the second load source, flow-induced model accelerations, is, in part, nullified by the acceleration damper while the remainder (that induced in model and sting support) can, in principle, be reduced by interposing an elastic material between the model structure and the transducer. However, the mass of a transducer often is so small that it cannot be effectively isolated; the only alternative is to use a unit with inherently low acceleration sensitivity. This last approach also helps reduce the third load component, accelerations from suddenly applied pressure; alternatively, this loading might also be damped by an orifice-fed cavity, if the cavity fill time could be tolerated. Both approaches were used in the present work.

Thermal protection is required to prevent damage to pressure transducers and suprious outputs due to thermal expansion of sensing elements. Two concepts were considered in this design study – ablation cooling and heat-sink cooling; both require mass addition which increases the response time of the transducer. Ablation cooling is most effective for a flush-mounted cell exposed to very high temperature gases, such as in the reservoir or at the stagnation point of a model. If the transducer has a high resonant frequency (> 50 kHz), adding a thin layer of ablative material (e.g., silicone rubber) will not degrade the response time excessively. For example, in figure 18 case ① represents a piezoelectric transducer having a natural resonant frequency of 130 kHz, a

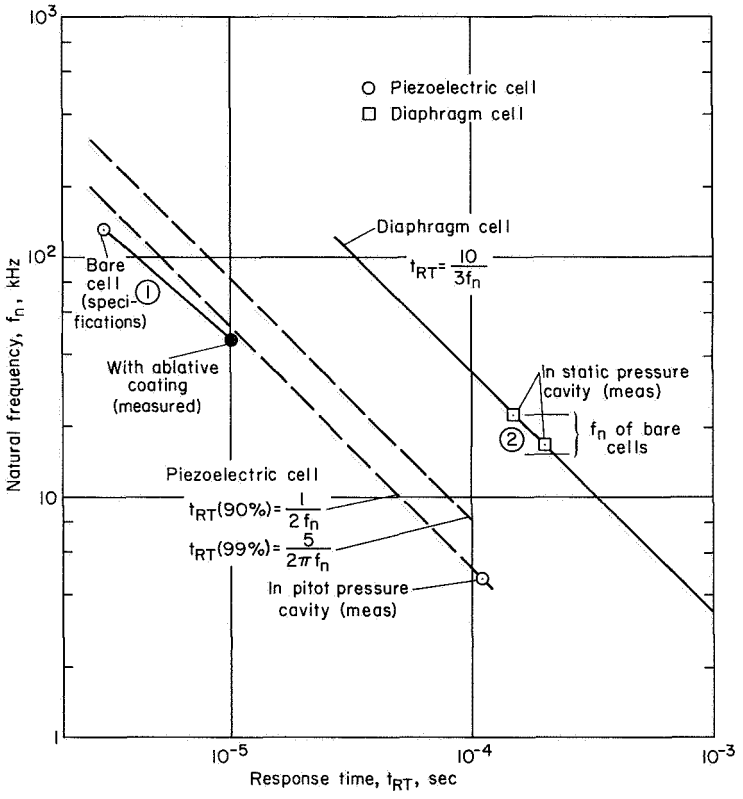

Figure 18.– Response time of pressure transducers and thermal cavities.

nominal response time of 3 μsec, and with ablative ablative protection, a 10 μsec response. On the other hand, case ② is a diaphram-type cell with $f_n \approx 20$ kHz, which, with an added layer of ablative material, could have a response time of 0.5 msec or more. In this case, it might be better to mount the cell behind a small cavity containing a heat-sink material like copper, over which the gas must flow prior to contacting the diaphragm. By careful design, such cavities can have a fill time of 0.1 to 0.2 msec and serve to protect against both flash heating and diaphragm acceleration from sudden pressure loading (see fig. 18).

Having discussed design methods whereby thermal and acceleration effects are controlled for low-pressure measurements, consider now the inherent qualities of two types of pressure transducers that apply to this regime, say, from 10^{-5} to 10^{-1} atm. Table 1 lists these qualities

for commerical quartz-crystal piezoelectric cells and for variable-capacitance type pressure cells having stretched invar diaphragms.[3] The primary advantage of the piezoelectric type is response time, but its use is limited to the upper two decades of pressure by the acceleration

TABLE 1.– PRESSURE TRANSDUCERS FOR SHOCK TUNNEL APPLICATION

Type	Diameter, mm	Length, mm	fn, kHz	Response time, μ sec	Pressure range, atm	Acceleration sensitivity on axis, atm/g	Temperature sensitivity, percent/°C	Diaphragm thickness, mm
Piezoelectric	10.9	26.7	60	6	10^{-3} - 10^{-1}	1.4×10^{-3}	0.02[a]	– – –
(absolute)	6.4	15.2	130	3	10^{-2} - 10^{-1}	7×10^{-3}	.02[a]	– – –
Variable capacitance	7.9	7.4	~20	150	10^{-5} - 10^{-3}	2.5×10^{-5}	.10	0.0031
(differential)	7.9	7.4	>20	<150	10^{-3} - 10^{-1}	3.1×10^{-4}	.10	.038

[a]Nominal value for quartz, not including mechanical distortion of diaphragm seal due to flash heating.

sensitivity. The capacitance type has a relatively slow response time but can be extended to lower pressures because the acceleration effect is less by a factor of 50. Neither type of cell is unduely sensitive to flash heating, but both must obviously be protected from gas temperatures that locally exceed 3000° K. The diaphragm cell has a size advantage, but is more complicated to use since it is a differential cell. In practice, there is a considerable region of overlap where both types can be used for comparison. An alternate design for a low-pressure transducer has been originated and patented by H. L. Seegmiller (see ref. 17) wherein the motion of a slack diaphragm in response to an imposed pressure force is measured. Such a cell would have much better time response and far less temperature sensitivity than the diaphragm cells shown above.

A study of force-measuring techniques in hypersonic flow has shown that steady-state, elastic balances are not applicable to test times of 1 to 2 msec. Some inertial method must then be used. The most promising appears to be a variation of the free-flight method in which accelerometer signals are transmitted through flexible trailing leads. Conceptually, a rigid model is instrumented with miniature accelerometers and supported by threads; the model fits over but does not touch a hollow sting which serves as a conduit for the trailing leads and as a catcher for the model. For tests where support interference must be minimized, the free-flight model could be caught in a net at the bottom of the test section. Adequate response time and signal strength can be achieved with existing commercial accelerometers.

Data recording system– The analog signals from pressure or heat-transfer transducers must be converted to digital form for computer input. It is advantageous to perform this conversion within the basic recording instrument since data handling is reduced and a higher level of accuracy is maintained. This was accomplished by the development of the 1/2-megacycle digital recording

[3]The capacitance cells, which are made at Ames, are briefly described in reference 16. Recent improvements include the use of pretensioned invar diaphragms as thin as 3×10^{-3} mm to achieve a rated pressure range of 3×10^{-4} atm, a high natural frequency, and a minimum temperature sensitivity. The piezoelectric cells are available from the Kistler Instrument Corporation.

system described in reference 18. Low-level analog signals from a test model (up to 24 channels) are individually amplified, sequentially switched, and presented as a train of analog samples to a high-speed, analog-to-digital converter. The output of the ADC is stored in four magnetostrictive delay lines in real time, with a total storage capacity of 5000 samples during a 10-msec period. The delay lines are mechanical and store the incoming digital information in binary form as a train of torsional stress waves that travel at the acoustic velocity of the line. The lines are of sufficient length to have a wave transit time of 10 msec. Stored information can be interrogated without destroying the data, thereby enabling an immediate scan of test results (pen recorder) prior to making a permanent record in digital form as a typewriter listing and a punched paper tape.

The constant sampling rate (5×10^5/sec) can be applied to the number of channels desired (from 1 to 24) to match the number of transducers or to adjust the time interval between samples in each channel. Amplifier gain and response, as well as delay line function, can be checked with internal signals.

Considerable original effort was required to integrate this recorder with the shock-tunnel environment. Both recorder protection and common-mode noise were considered, the former being related to the capacitor bank discharge which heats the driver gas and the latter to the flow of hot gas (plasma) past the model surface. The final result is the unique grounding and isolation system shown in figure 19. The safety ground serves to protect the recorder from a faulty discharge of the

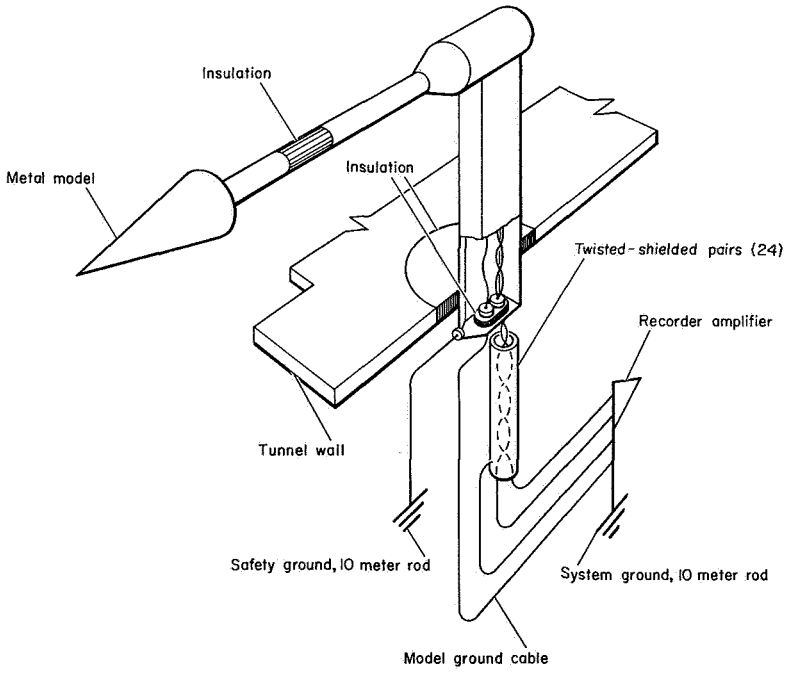

Figure 19.– Model and recorder grounding system, thermocouple readout.

driver capacitor bank which might induce current flow in the tunnel structure, while both the safety and model grounds remove the charge picked up from the flowing plasma. By this means, common-mode noise levels were reduced to a few microvolts.

Additional safety features include the use of isolation transformers at the power input to the recorder system, an optical isolation device in the trigger signal circuit, and optical telemetry circuits (ref. 19) to carry signals from the shock tube (e.g., reservoir pressure) to the recorder.

FACILITY PERFORMANCE

Energy Transfer to Driver Gas

The present discussion will touch briefly on the performance of the arc driver system over the available range of arc lengths, and then will concentrate on the experimental results for the 2.9-m arcs used for shock-tunnel operation.

Arc discharge characteristics– An operating map of the system is shown in figure 20 in terms of capacitor bank voltage and arc length, with helium as the driver gas. Arc lengths from 0.75 to 2.95 m have been initiated over the range of voltage indicated in the upper shaded area, using a straight trigger wire and the full capacity of the bank (1250 μF). Arc-out voltages are shown (lower shaded band) to vary from 0 to about 20 kV with increasing arc length. Upper and lower limits to arc length are fixed by the voltage gradient required to cause a discharge (about 11 kV/m) and by the requirement of a damped discharge, respectively. The efficiency of energy transfer from capacitor bank to driver tube, defined here as $(V_i^2 - V_f^2)/V_i^2$, varies from nearly 100 percent to about 75 percent with increasing arc length, based on V_i = 40 kV discharges. For further details on system performance, methods to improve the efficiency of long arcs, and an explanation of various arc phenomena, see references 4, 5, and 20 through 22.

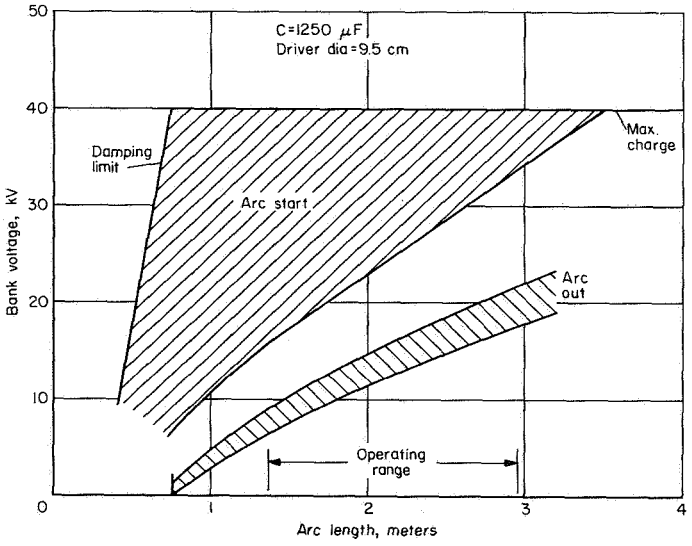

Figure 20.– Arc operating range in helium with a straight trigger wire, 2.9 m driver.

Driver gas conditions–Neglecting losses in the capacitor bank, cabling and grounding circuits during the arc discharge, the energy density achieved in the driver is shown in figure 21. With full-bank operation, the limits for a 0.75-m arc are about 10 and 200 J/cm^3, while for the 2.9-m arc, the limits are 20 and 40. Partial-bank operation could reduce the lower limit (as shown by the dashed line in the figure) if needed for a particular test. The velocity scale (at the left of the figure) is from the lower limit of figure 7 and indicates, very roughly, the relation between shock velocity and arc length for this facility.

Consider now the range of driver-gas conditions that can be obtained in the 2.9-m chamber. Figure 22 is an energy-pressure map on which is shown the ideal (uniform, constant-volume heating) helium temperature at any combination of energy input and driver loading pressure. Figure 23 is a similar map for driver pressure after heating. The symbols represent experimental energy transfer based on capacitor charge less residual voltage and, when compared to the *C-V* grid, indicate maximum conditions available assuming uniform heating with no energy losses. With full-bank operation, temperatures range from 2400° to 8000° K at pressures to 290 atm. In practice, the actual average values will be somewhat lower than these ideal figures, while local temperatures may vary considerably across the diameter of the tube. Additionally, a temperature gradient will develop along the tube when the diaphragm opens, since the gas at the upstream end of the driver has a

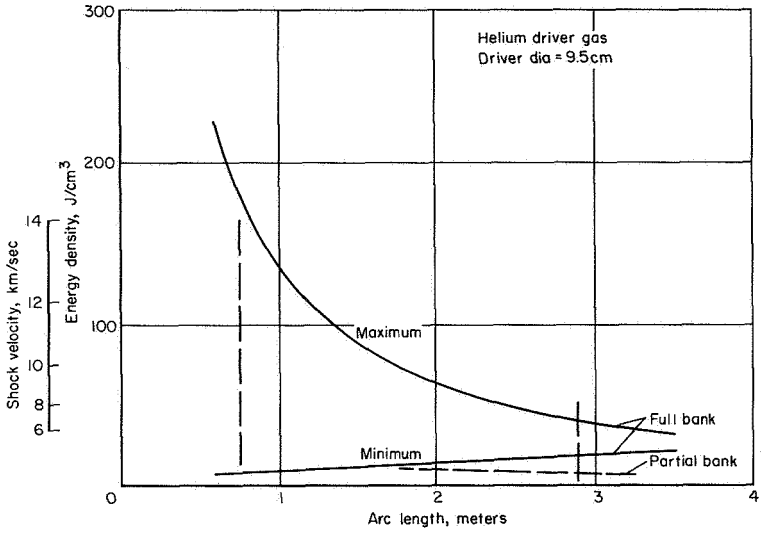

Figure 21.– Energy density available in arc chamber.

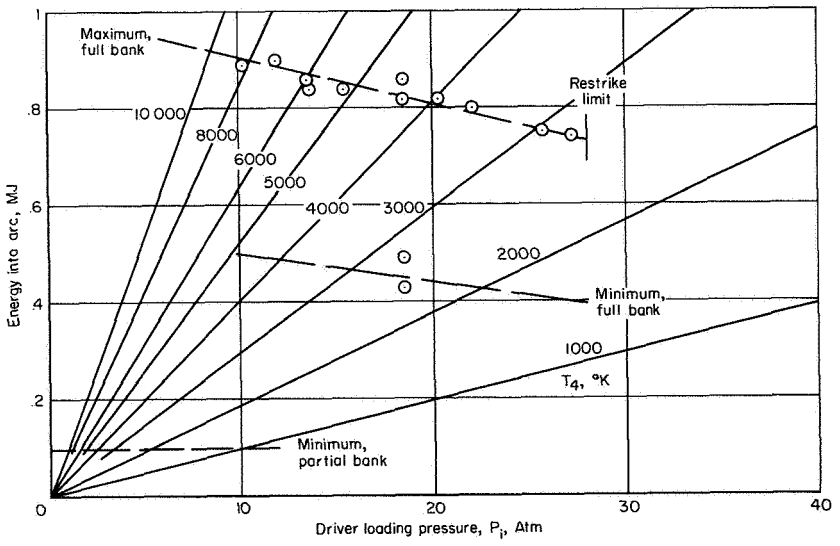

Figure 22.– Ideal driver temperature after arc heating, L_D = 2.9 m.

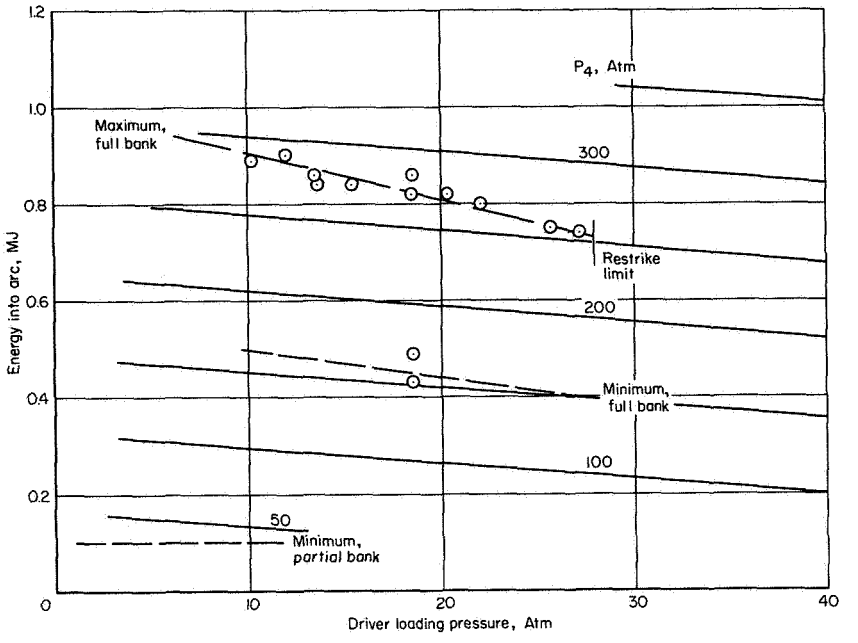

Figure 23.– Ideal driver pressure after arc heating, L_D = 2.9 m.

longer residence time (at high temperature) than that near the diaphragm. Tests are under way to evaluate some of these variables; until these results are available, the operational characteristics of the facility can only be referenced to the idealized driver conditions.

Diaphragm Operation

A diaphragm burst study was made, using the assembly shown in figure 8 by pressurizing the upstream chamber slowly until rupture occurred. The experimental results are shown in figure 24 (solid curves) for blank thicknesses from 1.6 to 3.2 mm and groove depths from 20 to 70 percent. Conditions were closely repeatable, while burst pressures varied from 40 to almost 550 atm. The dashed curves are lines of constant tear thickness. For groove depths less than 50 percent, the tear thickness must increase with blank thickness to retain a constant burst pressure, while above 50 percent the burst pressure depends on tear thickness alone. Thus, it appears that the stress concentration factor associated with the cruciform grooves becomes relatively constant at depths greater than 50 percent.

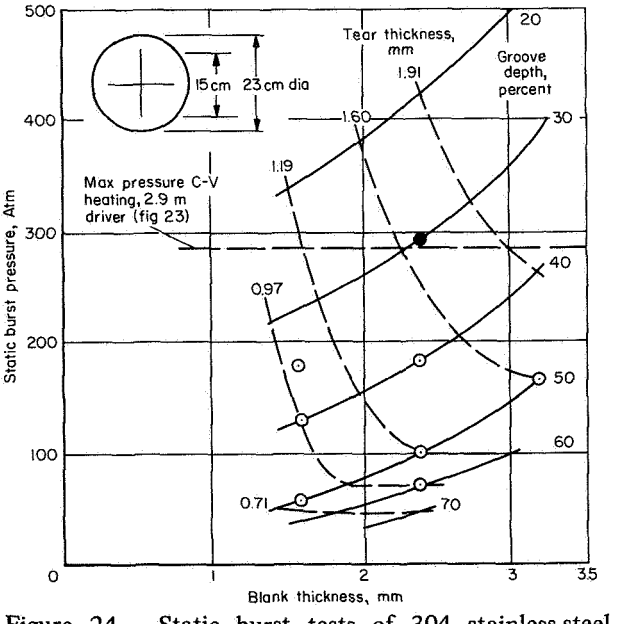

Figure 24.– Static burst tests of 304 stainless-steel diaphragms.

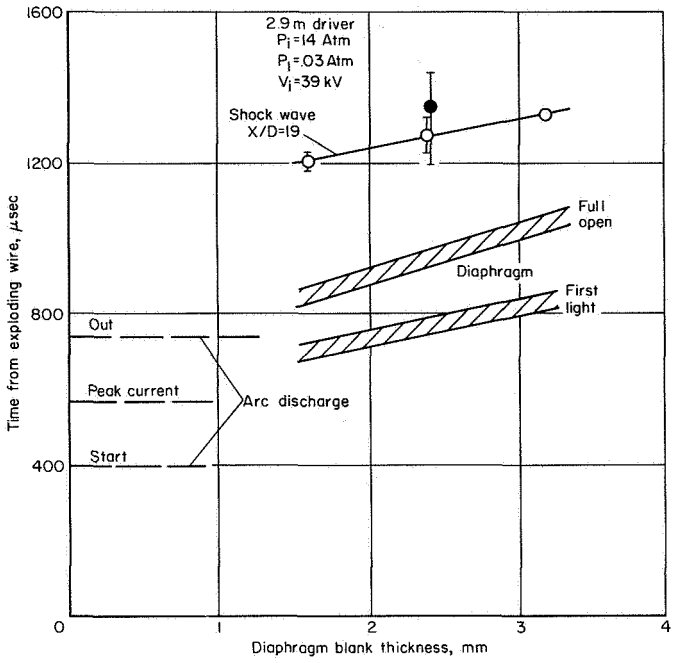

Figure 25.– Timing of events from start of discharge cycle.

For the present application, with the ideal maximum pressure in the driver just over 290 atm, a series of diaphragms (indicated by the symbols in fig. 24) was tested to determine the effects of diaphragm mass and bursting strength on shock-tube performance. The practical limits on blank thickness were set by loss of petal tips, at the lower end, and by erratic burst behavior at the upper. With one exception (solid symbol), all diaphragms were chosen to have bursting pressures well below the ideal driver pressure to assure a uniform rupture. An approximate time correlation of events during the discharge cycle is shown in figure 25. The main arc discharge starts about 400 μsec after wire explosion and lasts 350 μsec. The diaphragms start to open when the arc discharge is completed, and the primary shock reaches the first measuring station some 500 μsec later. For the limited range of thicknesses tested, there was little control over diaphragm timing relative to the arc discharge period. The high-pressure diaphragms (solid symbol) gave shock times that varied widely compared to the others, indicating a close approach to the upper pressure limit. (A "no open" situation is to be avoided with any length

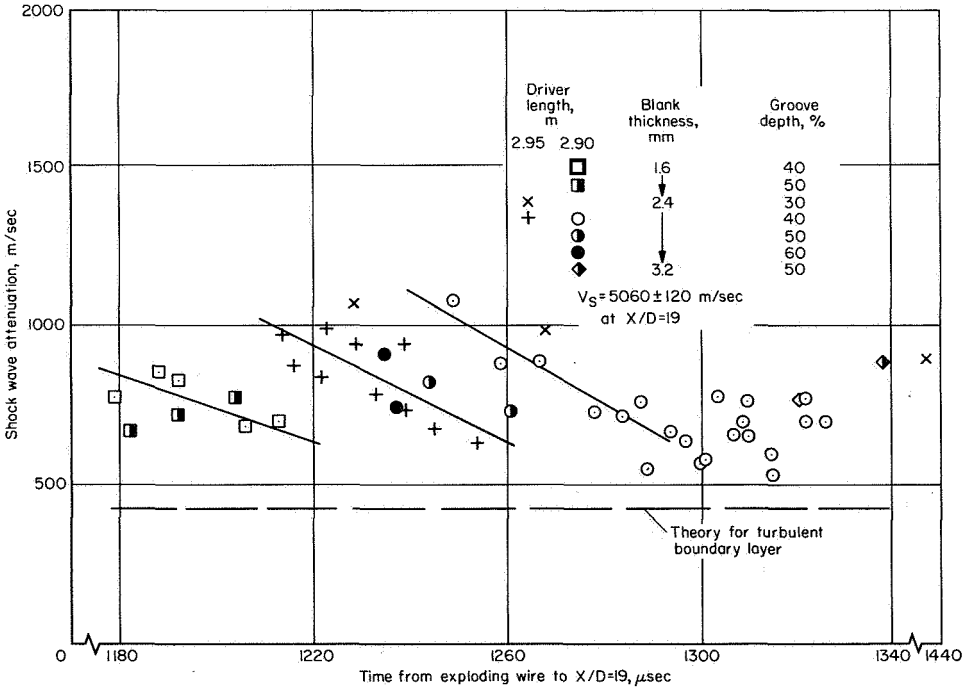

Figure 26.– Effect of diaphragm operation on shock-wave attenuation.

driver because the heated gas will severely degrade the insulating elements in the chamber; with the long-arc driver, the residual bank voltage of 15 to 18 kV is sufficient to cause considerable damage to the chamber itself, if arc discharge to ground occurs after local failure of an insulator due to overheating.)

Other results of this study are shown in figure 26, where shock-wave attenuation over the tube length (10 m) was chosen as the characteristic variable. The relatively constant level of attenuation over the entire range of observed times shows that there is little effect of diaphragm mass or bursting strength. The substantial variation within groups appears to show a consistent trend wherein the "slow openers" result in less shock-wave attenuation, approaching the theoretical value. This trend is assumed to represent the finer details of the diaphragm-opening process which are not readily controllable. Shock-tube performance at these stated conditions is not significantly influenced by changing diaphragm mass by a factor of 2 or bursting strength by a factor of 3, if bursting pressure does not exceed 2/3 of the ideal driver pressure.

Shock-Tube Performance

The performance of the driven tube will be covered in two sections: the incident shock and wave system, and the reflected shock reservoir. Results will be shown both for the 2.95-m driver (8.3-cm inside diameter) and the 2.90-m driver (9.5-cm inside diameter); in both cases, the inner surface of the liner is silicone rubber.

Incident shock wave– Representative variations of incident shock velocity with driven tube loading pressure are shown in figure 27. The measured velocity data in this figure are the maximum values obtained for each test; at values of P_1 above 0.01 atm this occurred over the interval $x/D = 19$ to 31, while at lower loading pressures the maximum velocity occurred between $x/D = 31$ to 54. The upper curves are theoretical predictions for the two drivers with an energy input of 8×10^5 J, the average for all test runs. Other information is tabulated in the figure, where the difference in ideal T_4 and P_4 due to driver volume is shown. Note that T_4' and P_4' are the effective driver conditions that result from the area ratio A_1/A_4, (after the method of ref. 5).

The measured shock velocities are essentially the same for both driver configurations, indicating that the larger diameter driver is more effective since the data fall closer to the theoretical performance curve. Now, some fraction of the velocity decrement is due to energy losses associated with diaphragm opening and the shock formation process. The former is found to be relatively small, at least on the basis of mechanical work; the latter involves turbulent mixing losses of unknown magnitude. For purposes of this analysis, both effects are termed "overall driver effectiveness," and the primary variable influencing shock-tube performance at these upstream locations is assumed to be the quality of the driver gas.

In the absence of any measurements of bulk gas properties in the driver, the gas quality will be inferred from the velocities. Two other sets of driver conditions (P_4' & T_4') more closely describe the observed performance (fig. 27). First, if a constant-volume cooling of a uniformly heated driver gas is assumed (2.90 m driver), then the set $P_4' = 187$ atm, and $T_4' = 3100°$ K compares with the data. This corresponds to a residual driver energy of 6×10^5 J of an initial 8×10^5, an energy loss of 25 percent. An alternate assumption is that the gas is not uniformly heated and that the first efflux is higher than average temperature; the set $P_4' = 100$ atm and $T_4' = 5000°$ K compares with

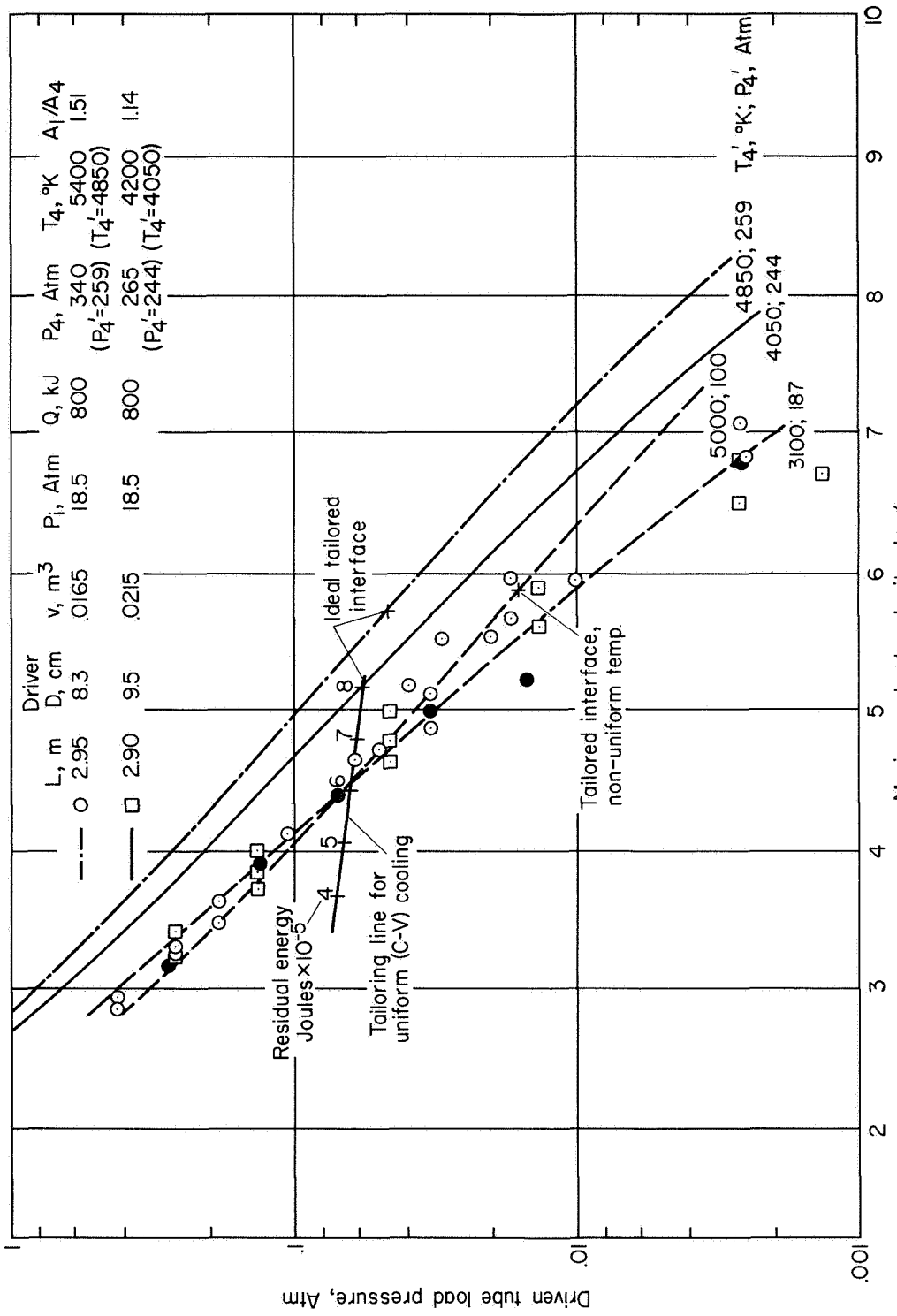

Figure 27.— Shock-tube performance with air.

measured velocities except at the lowest pressures. Thus, either mechanism appears to describe the physical behavior observed and additional information is required to make a choice and to evaluate the validity of the assumed process.

Figure 27 also shows the conditions at which a tailored interface should occur. For the two ideal driver curves, this occurs at $P_1 \approx 0.05$ atm and $V_S \approx 5.5$ km/sec; for nonideal performance with constant-volume cooling, it should fall on the nearly horizontal curve; for the nonuniform heating curve, at $P_1 \approx .015$ atm and $V_S \approx 5.9$ km/sec. This criterion is proposed as the basis for choosing the effective driver conditions. The essential connecting link in this analysis is provided by Flagg (ref. 23), who demonstrates that the best experimental tailoring is achieved at the *end* of a shock tube if the appropriate interface conditions are established near the *start* of the tube. Thus, later in this report, the tailored interface condition in the reservoir will be referred to these results.

Driver effectiveness– An indication of driver effectiveness, η, is shown in figures 28 and 29. As mentioned before, this is a lumped parameter defined as the theoretical driver energy required to develop the observed shock strength, ratioed to the actual energy removed from the storage bank. Constant-volume, uniform heating of the driver gas is assumed, and the shock velocity measured between $x/D = 19$ and 31 is used as the base. In figure 28, the variation of η with ideal T_4 is shown and, despite considerable scatter, a definite trend is visible.

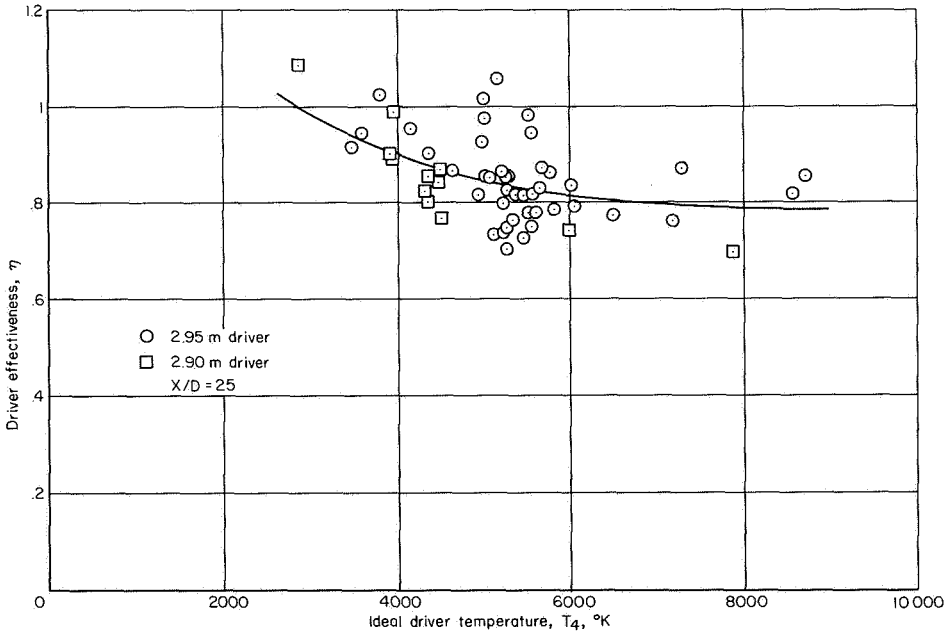

Figure 28.– Variation of driver effectiveness with temperature.

The rather surprising result is that overall driver effectiveness is so high. Not only does η approach the ideal limit at low temperatures (say, 3000° K) but it also decreases relatively slowly at $T_4 > 5000°$ K, where the average value is about 0.80. In fact, the variation of η for a threefold increase in temperature is no greater than the run-to-run variation at a constant temperature. Thus, for the T_4 range of these experiments, the arc-heated driver is a rather efficient energy converter, at least for the early times (after diaphragm opening) associated with this upstream position in the

shock tube. A word of caution is in order, however, since, in several cases, η exceeds unity. This $\eta > 1.0$ is noted elsewhere (e.g., ref. 22) as being characteristic of low driver specific energies (J/g); in reality, it suggests a compensating effect in the shock formation process, perhaps the initial efflux of a hotter-than-average driver gas mentioned earlier, which overcorrects for the concurrent energy loss mechanisms.

In figure 29, the driver effectiveness at constant T_4 varies inversely with tube loading pressure P_1 although, again, the scatter is large. In the P_1 range appropriate to tailored operation (0.01 to 0.06 atm) η is about 0.90, a very reasonable driver performance.

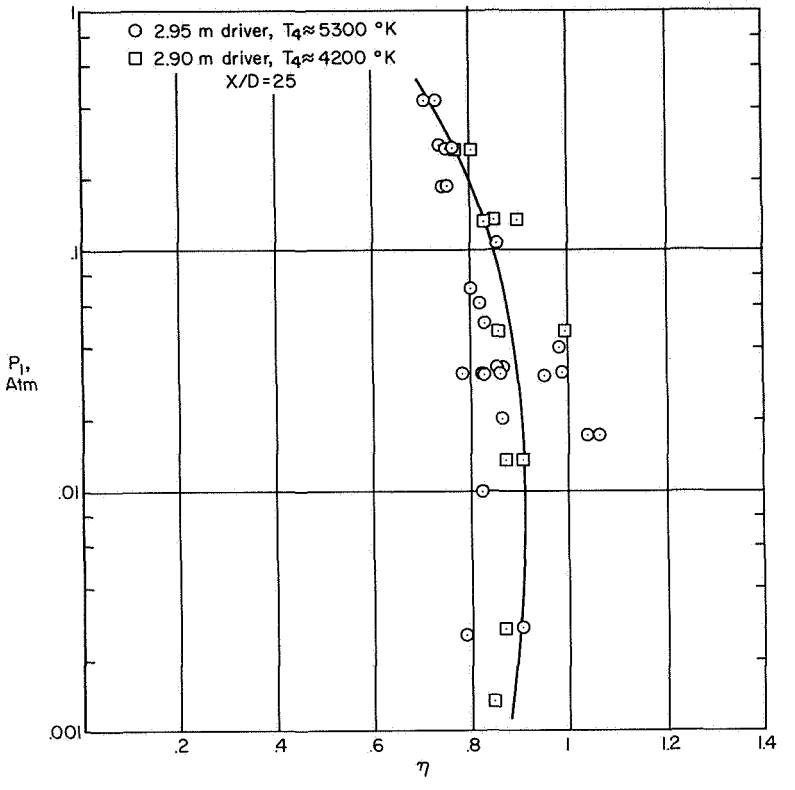

Figure 29.– Variation of η with tube initial pressure.

These results indicate a large fraction of the energy deposited in the driver chamber is initially made available to the driven tube, that the driver effectiveness is relatively constant at $T_4 > 5000°$ K, and that increasing diaphragm pressure ratio P_4/P_1 has a favorable influence. This is the situation as the incident shock wave is started down the driven tube.

Shock attenuation– It is generally accepted that the attenuation of an incident shock wave becomes more pronounced as the driver temperature is increased, presumably because of convective and radiative energy losses from the driver gas. If such is the case, it should be readily apparent in a comparison of total-to-boundary-layer-induced (viscous) attenuation. Hence, present results will be compared with the viscous attenuation theories developed by Mirels et al. and reported in references 24 to 26. Figure 30 illustrates the magnitude of the measured shock attenuation as a function of ideal driver temperature, at one driver tube loading pressure and with constant energy input. As T_4 increases, the experimental velocities at $x/D = 25$ stay near the ideal limit, while a substantial

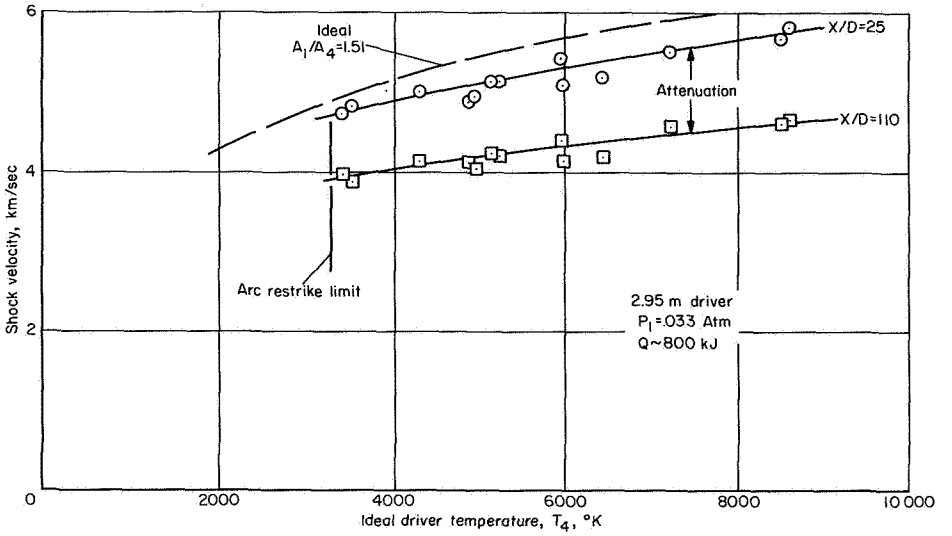

Figure 30.– Effect of driver temperature on shock attenuation.

and fairly constant attenuation occurs along the tube. Thus, at least for these conditions, the overall attenuation is not very temperature dependent.

In figure 31, the attenuation over the last 3 m of the tube is normalized by the appropriate theoretical value computed by the method of reference 24. The boundary layer was assumed turbulent. Despite considerable scatter in the data, it is obvious that relatively large attenuation occurs as P_1 increases and shock velocity correspondingly decreases. A rather strong influence of temperature is illustrated by the data at $P_1 \approx 0.03$ atm where a threefold increase in T_4 increases they relative attenuation by the same factor. Therefore, as T_4 is increased the influence of timewise variations in driver-gas properties appears to extend further downstream by virtue of the increased wave propagation speeds in the moving gas. The large values of attenuation (fig. 31) probably result from perturbations in the driver gas, which emanate from the driver itself, since the viscous attenuation theory is in reasonable agreement with experiment in other cases. The trends illustrated in the figure are attributed to expansion waves from

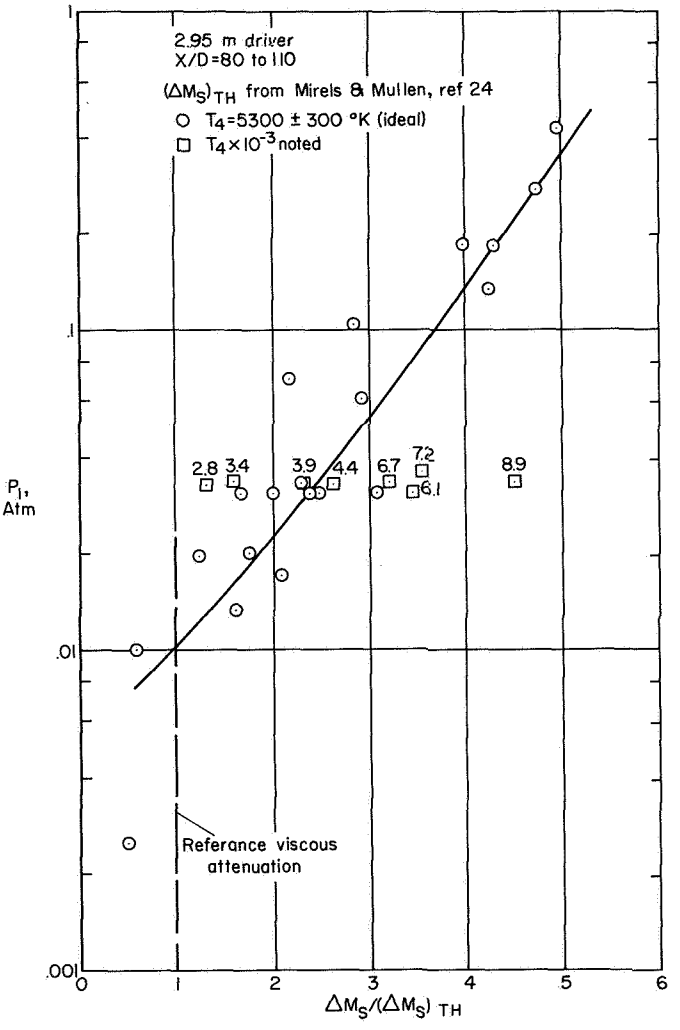

Figure 31.– Variation of shock attenuation ratio with inital pressure.

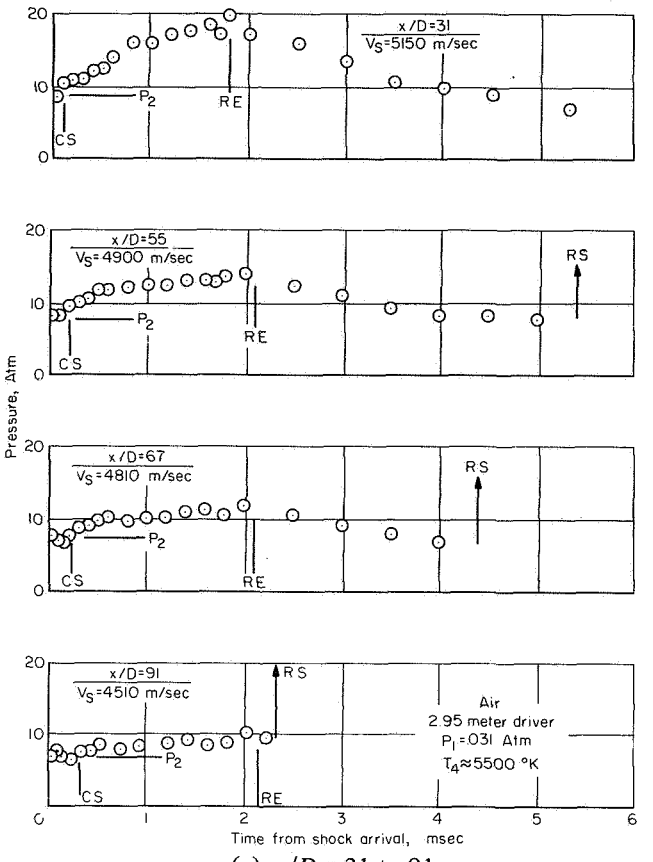

(a) $x/D = 31$ to 91

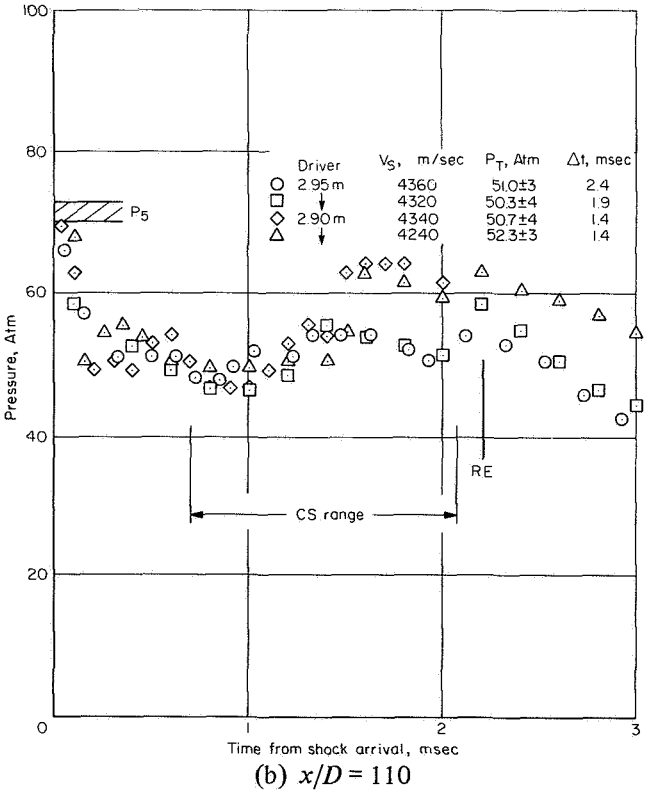

(b) $x/D = 110$

Figure 32.– Side wall pressure histories.

the driver, which could result from a nonuniform radial or axial temperature distribution. Very roughly, it appears that the higher velocity shock waves (lower P_1) outrun more of these secondary disturbances. Conversely, increasing T_4 causes a more rapid propagation of such disturbances down the tube. An investigation of driver performance is now under way to better understand the reasons for this behavior.

Wave histories– Before a discussion of conditions in the reflected-shock reservoir, an overall view of the wave system in the tube in in order. Figure 32 shows representative pressure histories at five positions along the tube from $x/D = 31$ to 110, for $P_1 = 0.031$ atm and $T_4 \approx 5500°$ K. Events are as expected at successive positions (fig. 32(a)), with a developing region of constant pressure behind the shock wave at the predicted level, an identification of the contact region by the twin-electrode probe record, (fig. 12) a gradual stretching of the primary driver expansion, and a following reflected expansion from the driver. A close inspection of the primary expansion shows a second and possibly a third expansion wave embedded in the initial system. These overiding waves are believed to originate in the driver tube, as suggested earlier, and contribute to the attenuation of the shock wave. Near the end wall (fig. 32(b)), the incident shock reflects at about 70 atm and, at this apparently undertailored condition, the pressure drops quickly to a quasi-steady level. This decrease from the reflected-shock pressure occurs so soon after shock arrival that it must be initiated by an expansion wave embedded in the incident system; the behavior is similar with or without an attached nozzle and is therefore not related to nozzle inlet filling. After the first drop, the pressure is fairly steady for 2.4 msec with the 2.95-m driver, or until the arrival of the reflected driver

expansion. With the 2.90-m driver, a second pressure jump occurs at about 1.5 msec, a reasonable time for the arrival of compression waves reflected from the contact surface and an expected feature in an undertailored reservoir. The arrival of the contact surface at the end wall is, as before, identified by the side-wall impedance probe; over a number of runs (at these conditions), the time varied from 0.7 to 2.1 msec in a random manner.[4]

Reflected Shock Reservoir

Theoretical estimates of the time interval for steady conditions in a shock-heated reservoir of test gas were presented earlier. These estimates represent an idealized limit defined by the tailored-interface concept for uniform driver conditions, an instantaneous diaphragm opening, and no viscous losses. In practice, a number of phenonema that modify the ideal performance have been identified and formalized to the extent that reasonable predictions can be made; other effects are not so well understood and only general trends are available. The most obvious and bothersome phenomenon is contact surface mixing, which reduces the amount of usable test gas both behind the incident shock wave and at the reflected shock interaction; the processes are not well understood but relate strongly to the behavior of the main diaphragm and to the relative gas densities at the contact surface. The second phenonemon is the loss of gas from the test slug into the wall boundary layer; here the mechanism is rather well defined (e.g., refs. 24–26). An application of this body of theory to the present experiments is given in appendix A. A third effect that reduces the usable test gas in the reservoir is the reflected-shock bifurcation concept proposed by Mark (ref. 27) and advanced by Davies (ref. 28). This process allows the boundary layer behind the reflected shock wave to move toward the end wall and mix with the test gas entering the nozzle throat, in some cases well before contact surface mixing degrades the sample.

In addition to these viscous loss mechanisms, at least two sources generate pressure waves to perturb the reservoir gas, namely, the arc-heated driver and the contact surface. The possibility of driver-generated expansion waves has already been suggested, with nonuniform heating and/or radiative cooling as the driving functions. Mixing action at the contact surface creates a region with both concentration and temperature gradients (ref. 29) so that passage of the reflected shock wave will generate nonideal wave packets that smear out in time.

Lastly, energy loss by radiation could degrade the reservoir gas. This possibility is considered in a later section, when nozzle flow properties are discussed.

In view of these many effects that can alter conditions in the reflected-shock reservoir, a direct experimental approach was used to find the tailored interface. Some typical results are shown in figure 33, where pressure histories behind the incident shock at $x/D = 91$ and in the reservoir at $x/D = 110$ are given. Driver conditions are roughly constant at 5000° K and 300 atm, while tube loading pressure is varied by two orders of magnitude. (Ideally, tailoring should occur at $M_S = 17$ and $P_1 = 0.050$ atm). At $P_1 = 0.27$ atm (fig. 33(a)), the reservoir is far undertailored, that is, an expansion wave results from the reflected shock-interface interaction and reflects from the end wall. Even before this, however, the pressure decays from P_5 due to an expansion wave following

[4] The impedance probe will obviously *see* changes in gas properties near the tube wall just ahead of the end wall. Consequently, the observed signal may lead or lag the arrival of the contact surface at the tube centerline.

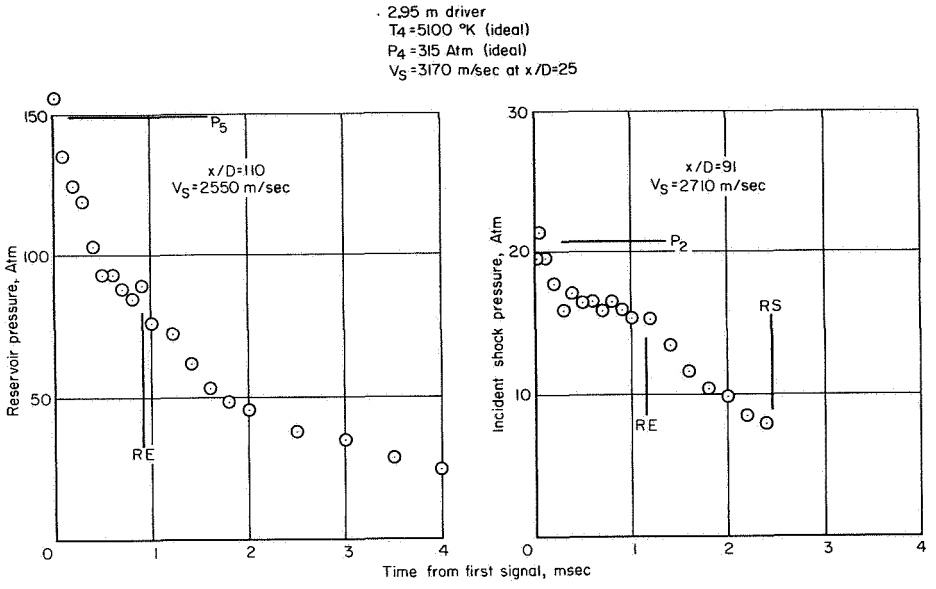

(a) P_1 = 0.276 atm

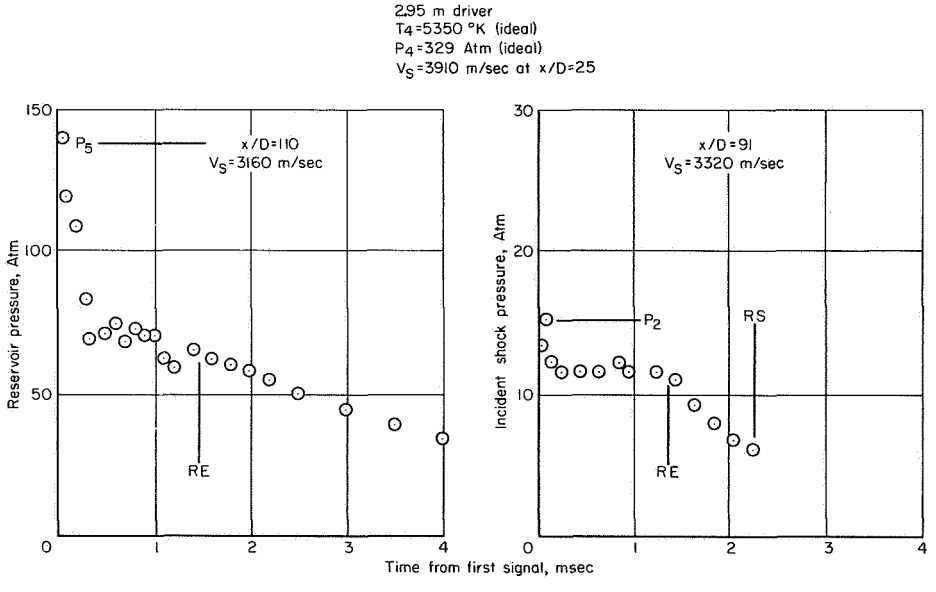

(b) P_1 = 0.132 atm

Figure 33.– Shock-tube performance at several initial pressures.

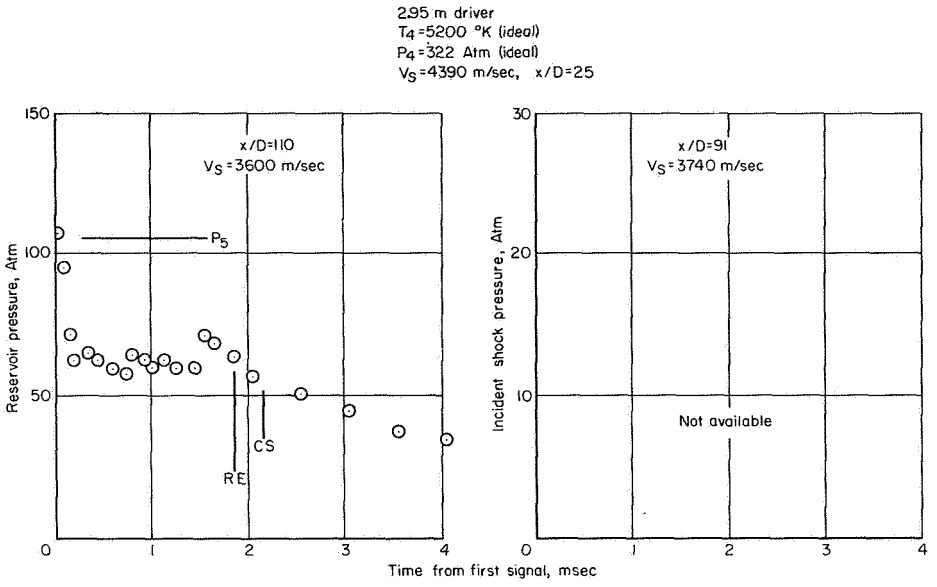

(c) $P_1 = 0.070$ atm

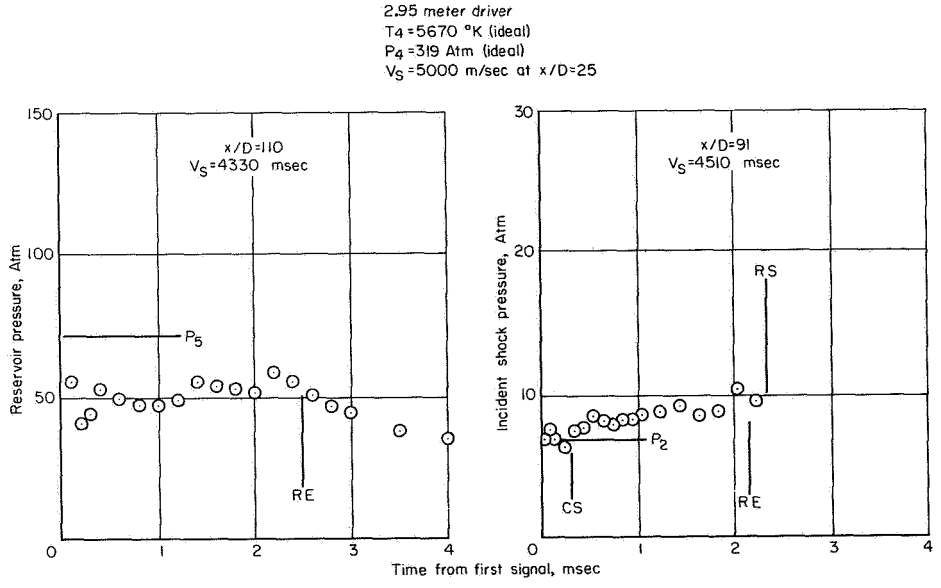

(d) $P_1 \approx 0.031$ atm

Figure 33.– Continued.

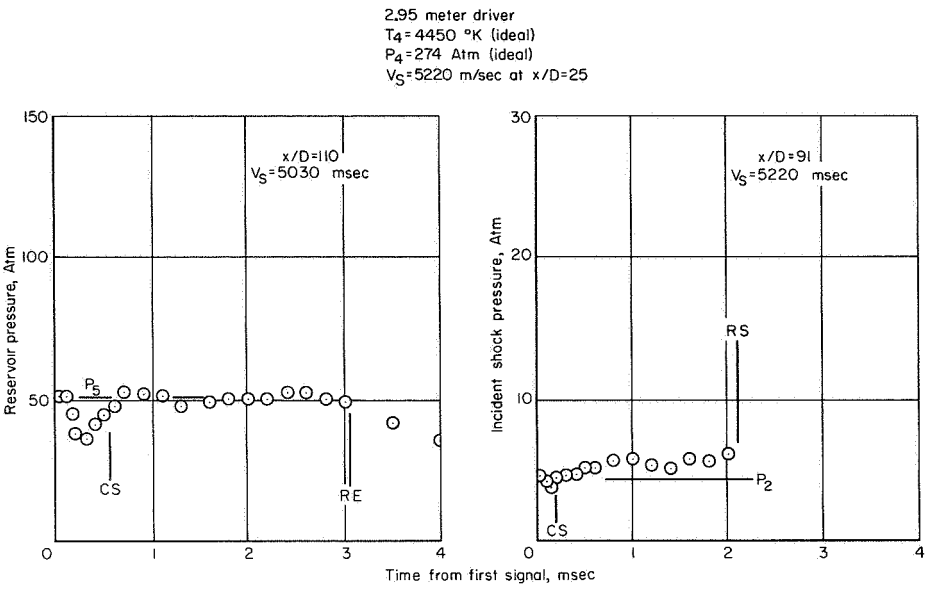

(e) P_1 = 0.015 atm

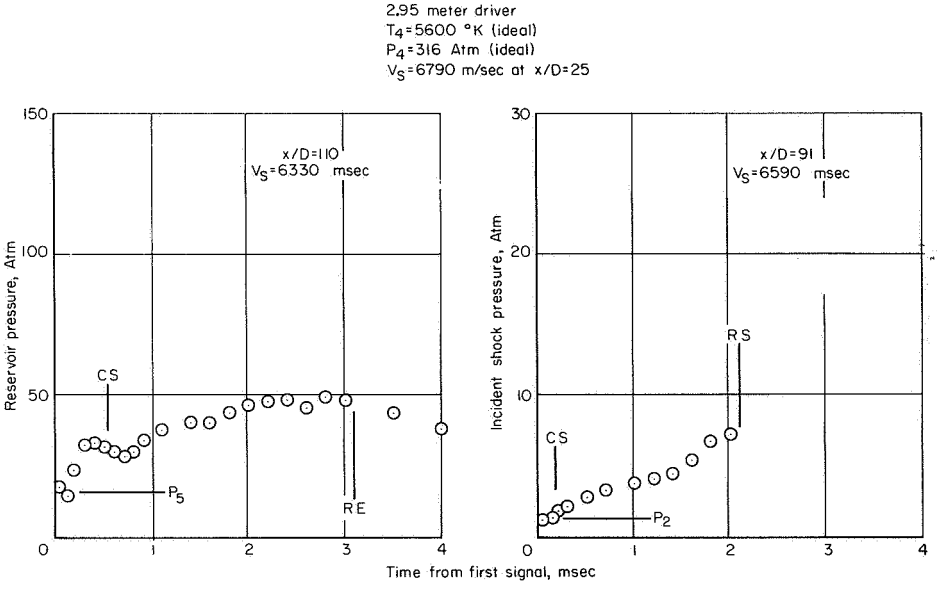

(f) P_1 = 0.0026 atm

Figure 33.– Concluded.

the incident shock, shown in the record at $x/D = 91$. The reservoir drops to about $1/2\,P_5$ before the reflected driver expansion arrives. The behavior is similar at $P_1 = 0.132$ and 0.070 (figs. 33(b) and 33(c)) except that the pressure is stable for a longer time. In figure 33(d), the loading pressure is well below the ideal value but the reservoir record remains undertailored; this can be attributed to the shock velocity being less than required for tailoring (due to viscous and expansion-wave attenuation) so that the driver gas behind the interface has not expanded to the desired temperature, T_3. On the other hand, the record at $x/D = 91$ now shows the rising pressure that should occur in the absence of a large secondary driver expansion. At $P_1 = 0.015$ atm, the record has the appearance of a tailored interface with two imposed expansion waves, already present at $x/D = 91$; the shock attenuation is quite small and the velocity comes close to the ideal value. Finally, in figure 33(f), where $P_1 \approx 0.003$ atm, the record indicates the reservoir to be overtailored (successive shock reflections), at incident shock velocities in excess of the ideal tailored value of about 5800 m/sec. Figure 34 is a summary plot of these and other results.

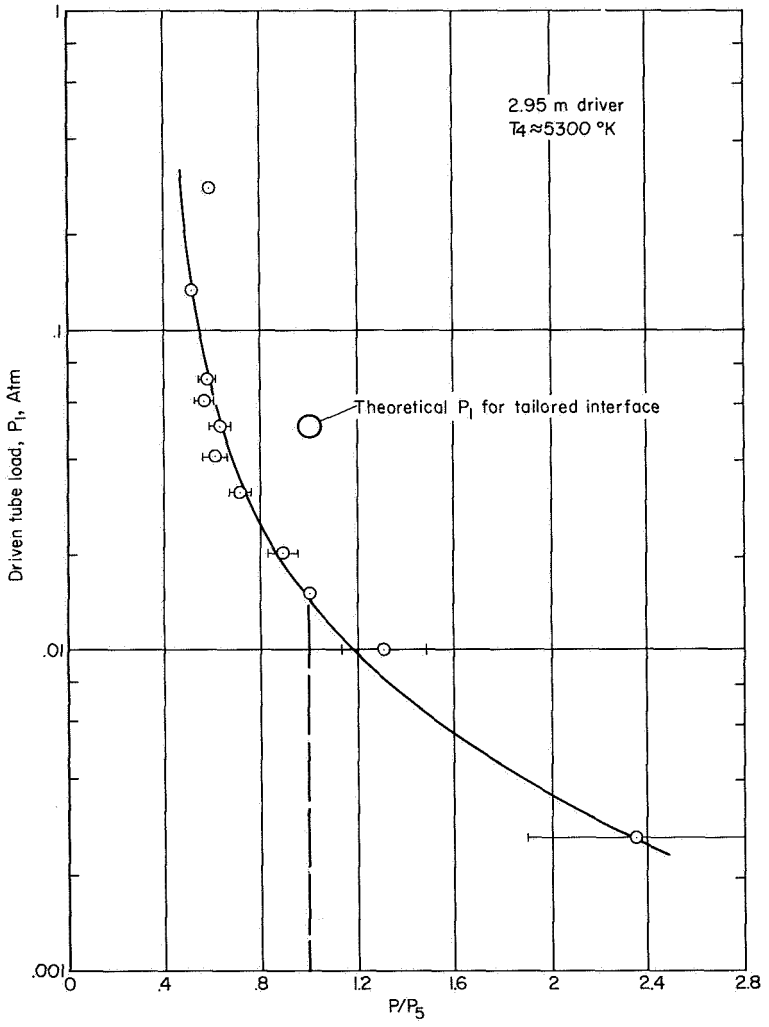

Figure 34.– Identification of tailored interface condition.

These results indicate that interface tailoring occurs when the driver gas has been expanded to about the temperature required for interface matching. In an ideal gas this is defined simply as

$$T_3 = T_2 \frac{(\gamma_4 + 1)m_4}{(\gamma_1 + 1)m_1} \tag{5}$$

while in real gases there is a dependence on P_1. To achieve the required gas velocity for matching T_3, the tube loading pressure must be reduced below the ideal value to compensate for nonideal effects in driver and diaphragm performance (in this illustration, by a factor of about 3).

An alternate approach to tailoring is shown in figure 35 where P_1 and P_4 (ideal) are nearly constant and T_4 (ideal) is varied from 8600° to 3470° K. At the right of each figure, the shock velocity profile is compared to the attenuation predicted from Mirels' theory for turbulent boundary layer (ref. 26), matched to the experimental velocity at $x/D = 25$. As T_4 is decreased the reservoir pressure approaches a tailored condition and the shock attenuation is reduced. At T_4 = 3470° K and P_4 = 314 atm (fig. 35(d)), the predicted tailoring velocity is 4730 m/sec at P_1 = 0.095 atm. Again, the tailored interface appears to occur at the shock velocity that expands T_3 to the interface matching value, while the loading pressure is about 1/3 the ideal.

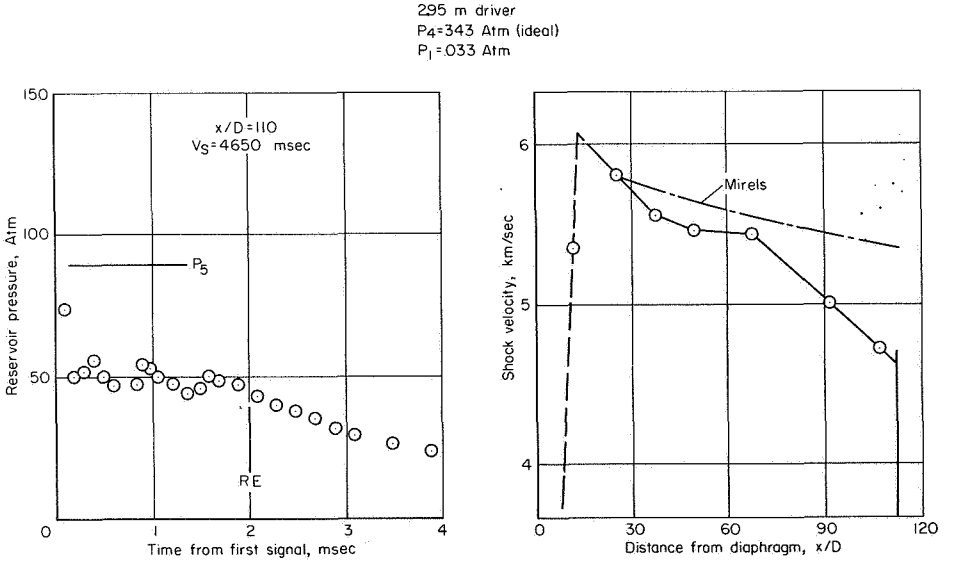

(a) T_4 = 8600° K (ideal).

Figure 35.– Shock-tube performance at several driver temperatures.

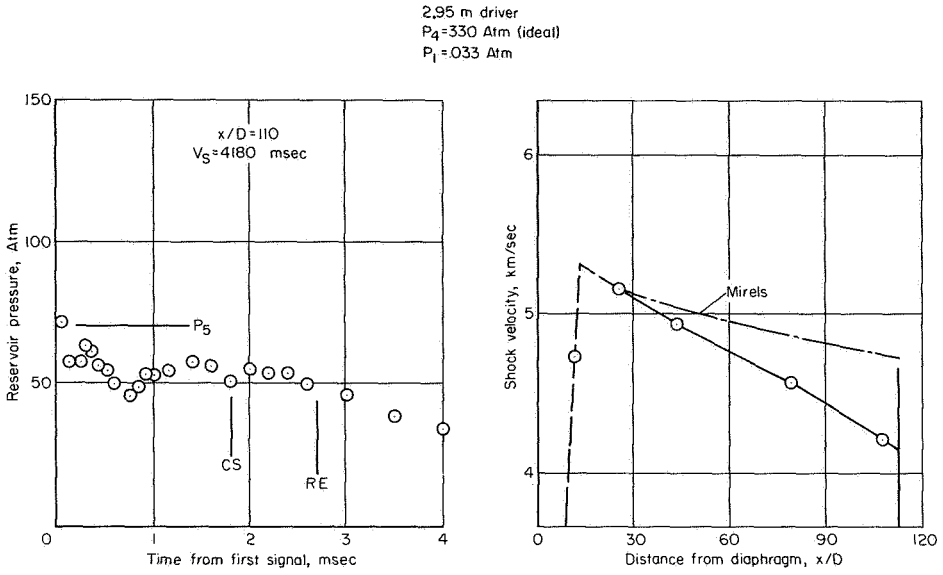

(b) $T_4 = 6460°$ K (ideal).

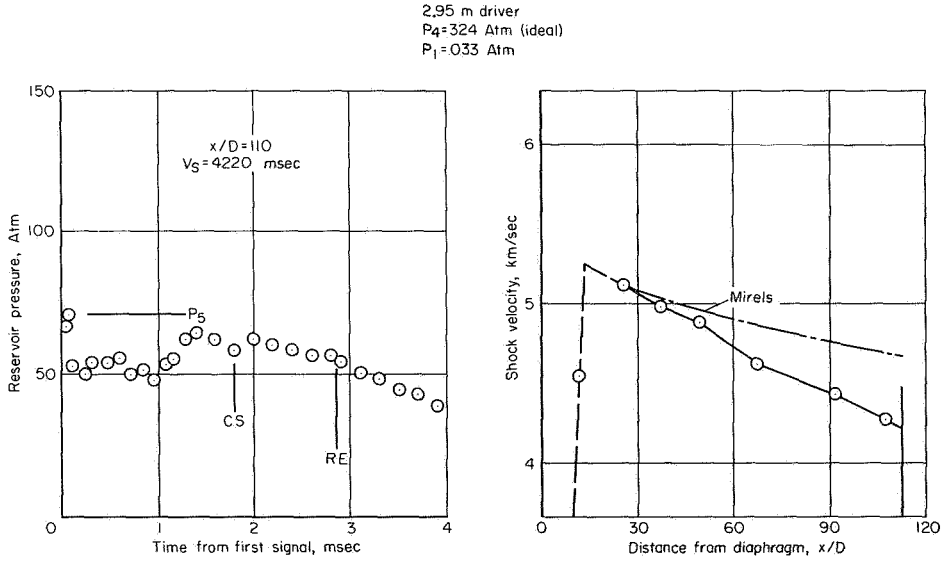

(c) $T_4 = 5250°$ K (ideal).

Figure 35.– Continued.

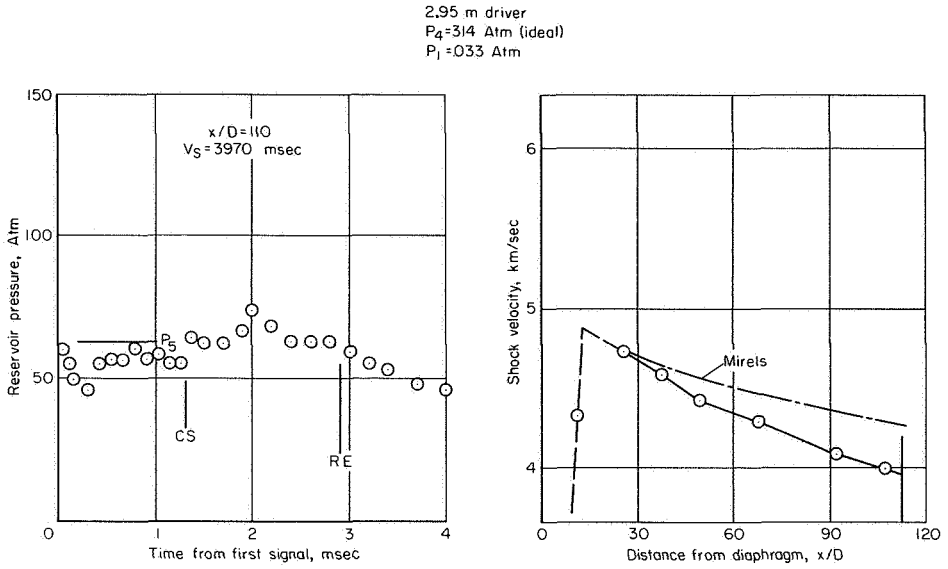

(d) T_4 = 3470° K (ideal).

Figure 35.– Concluded.

In summary, the arc-heated driver can be adjusted to yield tailored-interface reservoir conditions, with reasonably steady pressures for times that compare favorably with the theoretical predictions of figure 11. Results for two driver conditions are summarized in figure 36 where, as a function of shock-wave velocity, time is measured from the start of the steady pressure period. As shock velocity is increased (by lowering P_1) toward the tailored interface condition, the arrival of the reflected driver expansion is delayed and the useful time increases. At $V_S > 4$ km/sec, the reservoir pressure remains nearly steady for 1.5 to 2.0 msec. In general, tailored reservoir pressures are limited by available driver pressure (which, in turn, is fixed by capacitor energy) and by the reduction in tube loading pressure needed to achieve the tailoring shock wave velocity. Tailored reservoir enthalpy depends mainly on driver temperature, which is easily varied, but will be limited by attenuation and radiation losses as T_4 is increased.

A detailed examination of the several viscous effects that serve to reduce the usable slug of reservoir gas is beyond the scope of the present report. However, a brief study of the mass loss around the interface is given in appendix A, where the predictions of Mirels compare favorably with experiment. The combined effect of viscous losses will be considered in the next section by evaluating the residual test time available in the nozzle flow.

Nozzle Flow

The characteristics of an expanding nozzle flow of air and the stream properties in the test section were investigated for a nominal set of reservoir conditions, H_T = 18.6 kJ/g and P_T = 54 atm. These conditions were obtained, purposely, with an undertailored shock system, to suppress the propagation of interface – mixed gases into the test gas adjacent to the nozzle inlet.

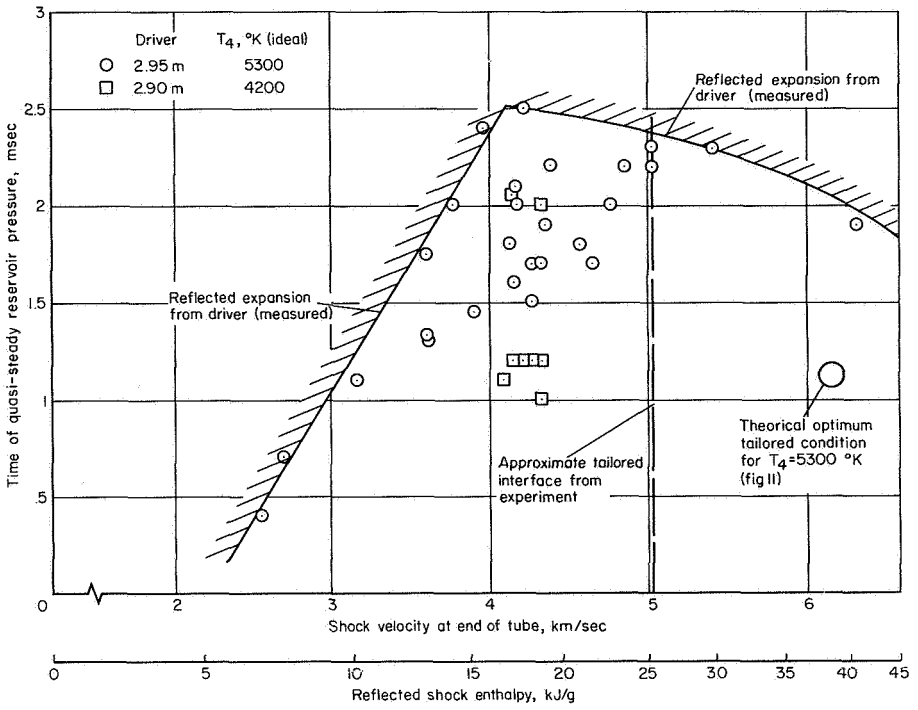

Figure 36.– Duration of steady reservoir pressure.

Typical reservoir pressure histories are illustrated in figure 32(b) for the two driver configurations used. Figure 37 is a photograph of the nozzle and test section.

Nozzle starting time– The time required for the starting shock wave and the first steady-flow signal to reach the test section are shown in figure 38, for two nozzle throat diameters.[5] The experimental results are compared with the incident shock theory of reference 11 and the steady-flow concept of reference 9, as shown previously in figure 15. It is apparent that the incident shock wave arrives much earlier than predicted, particularly when the smaller throat ($d^* = 0.45$ cm) is used. Steady-flow arrival times agree reasonably well with the simple ($U-a$) prediction and show little effect of nozzle throat size; values range from about 0.7 to 1.0 msec. If ($U+a$) time gained at the end of nozzle flow (fig. 15) is subtracted from these values, the net loss in test time due to nozzle transients is only 0.3 to 0.5 msec. This loss factor is expected to vary inversely with total enthalpy, which is corroborated by the trends shown in figure 39 for pure nitrogen. These data, from the investigation reported in reference 30, were obtained in this same nozzle with $d^* = 0.32$ cm; they indicate a similar shock arrival time but a longer interval until steady flow begins. As the enthalpy H_T is increased from 7 to 40 kJ/g, the starting interval is reduced by 1/2.

Model starting time– A limited amount of data was obtained to indicate the time required for steady flow to become established on a long slender model (compared in fig. 40 as a function of local flow temperature, with predictions shown earlier in fig. 16). The two curves of $t = L/a$ correspond to the pressure orifice locations L on a static pressure probe with an ogive tip of fineness

[5] The usable flow time in the test section begins with the first steady flow signal and continues until a ($U+a$) wave from the reservoir signals the arrival of the reflected driver expansion.

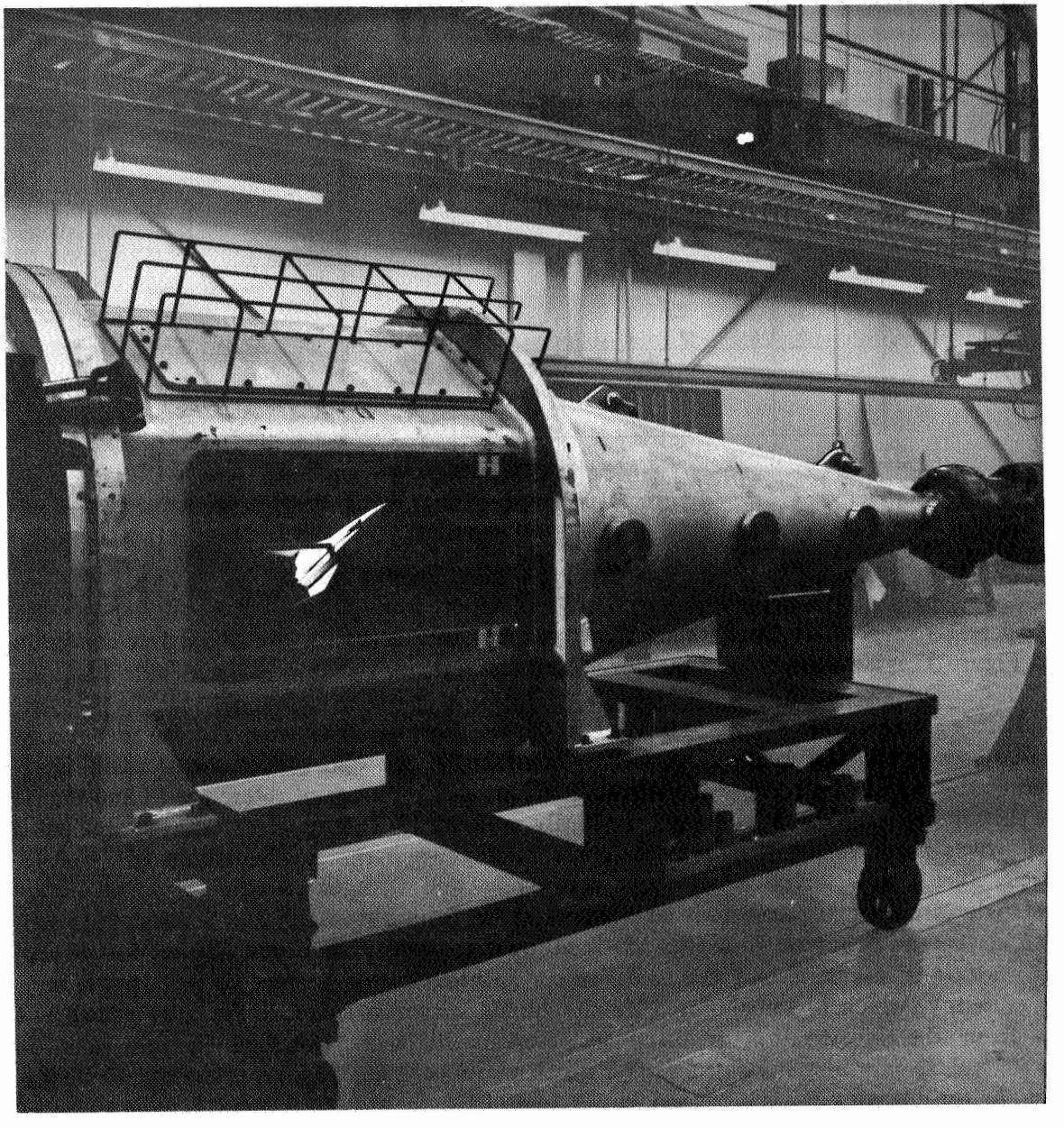

Figure 37.– Nozzle and test section.

ratio 10.9. The experimental results are shown as index marks on these curves, at the appropriate time values. Local flow temperatures are not known for each case but should be less than the equilibrium flow estimate shown in the figure. With one exception, the flow adjustment times appear in reasonable agreement with predictions based on the local speed of sound and body length. Note that these times are about the same as those identified with nozzle starting transients.

Test time– Measurements of nozzle test time are shown in figure 41 at shock velocities near 4300 m/sec, the velocity that yields a nominal reservoir enthalpy of 18.6 kJ/g. Test time is defined here as that period during which the flow in the test section is "aerodynamically clean" as evidenced by a constant ratio of either static pressure to total (reservoir) pressure P_∞/P_T or pitot pressure to total pressure P_{T2}/P_T, and/or by a stagnation heating rate representative of the test gas reservoir enthalpy. In most cases, the arrival of driver gas in the test region was signaled by a clear deviation from these criteria. In figure 41 the

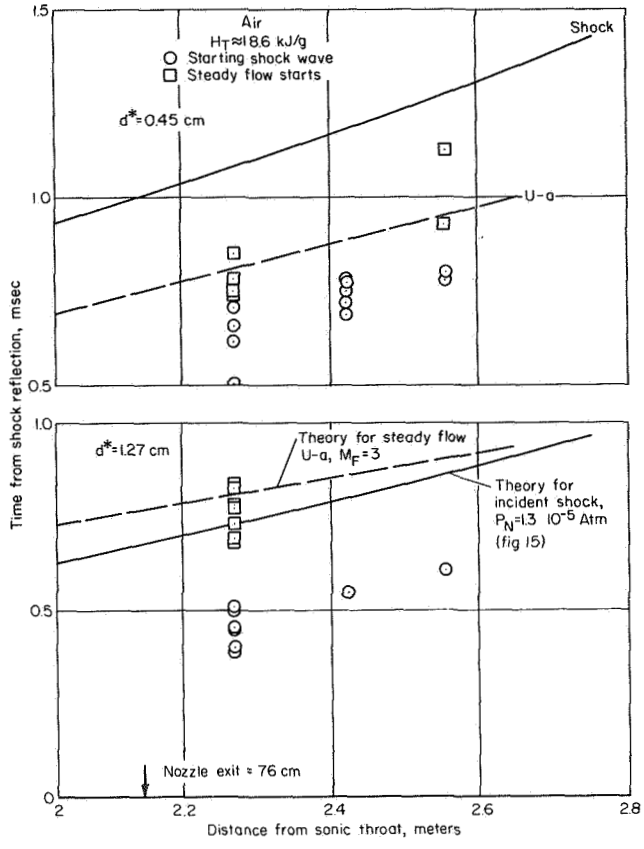

Figure 38.– Comparison of nozzle starting time with theory.

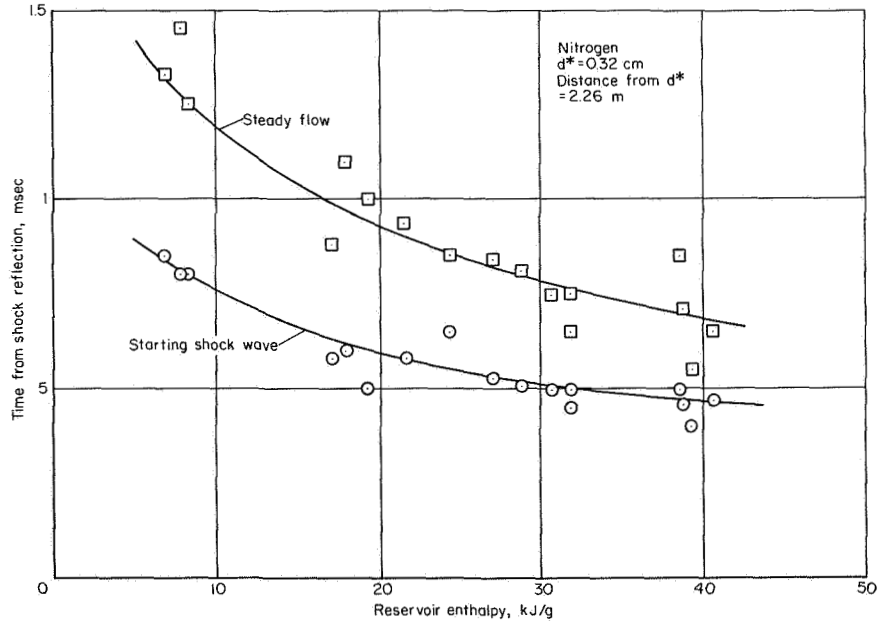

Figure 39.– Effect of reservoir enthalpy on nozzle starting time.

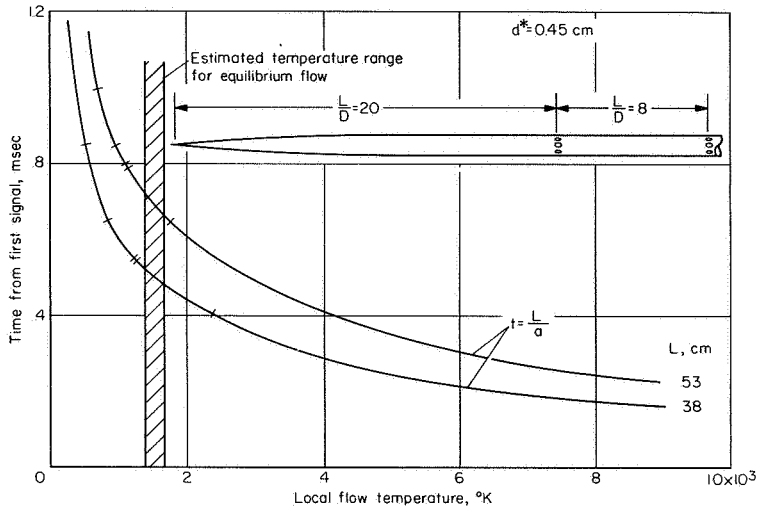

Figure 40.– Time to establish steady flow on a slender model.

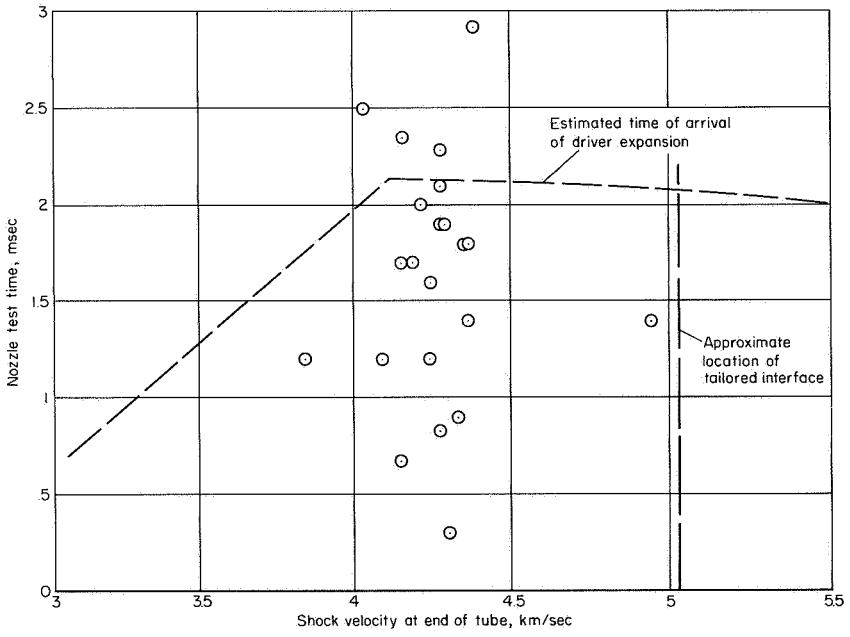

Figure 41.– Test time at exit of 76-cm nozzle.

data are compared with an upper boundary represented by the arrival of the leading edge of the reflected driver expansion in the test region. The recorded test time varies substantially from run to run but generally falls within the indicated limit. The average is between 1.5 and 2.0 msec, with lower values attributed to more interface mixing in the reservoir or a slower nozzle starting process. A few relatively long times show that test gas, on occasion, can be available up to or even beyond the arrival of the driver expansion. Thus, on the basis of the present sample, a test time of at least 1.0 msec is available in four out of five runs at the stated reservoir conditions.

Stream calibration– The nozzle expansion of a shock-heated, partly dissociated, diatomic gas can be safely assumed to incur nonequilibrium of both chemical and vibrational energies. The

available literature has demonstrated this fact most convincingly. Knowing this, the stream properties to be measured must be chosen to identify the degree of nonequilibrium, that is, the depth to which the fine structure is probed should be consistent with the intended use. In the present study, the method outlined in reference 2 will be used since the objective is a stream suitable for aerodynamic testing. Hiers (ref. 2) shows that when the conventional stream pressures (pitot and static) are properly interpreted, they define an effective freeze Mach number M_F and expansion ratio A/A^*; these terms can be used, in turn, to derive the remaining stream properties. The resultant set was found (ref. 2) to be in good agreement with a numerical solution of the nonequilibrium expansion.

This method is applied to the present results in figure 42, where the coordinates are static pressure and pitot pressure referenced to reservoir pressure. The M_F and A/A^* grid represents a set of one-dimensional, real-gas calculations of air expansions; in each solution, equilibrium flow is assumed to exist from the reservoir to the flow freeze point defined by M_F. Beyond this point, the chemical composition and the vibrational energy are assumed constant as the expansion continues in the translational and rotational energy modes. This grid is the theoretical map to which the experimental measurements will be matched.

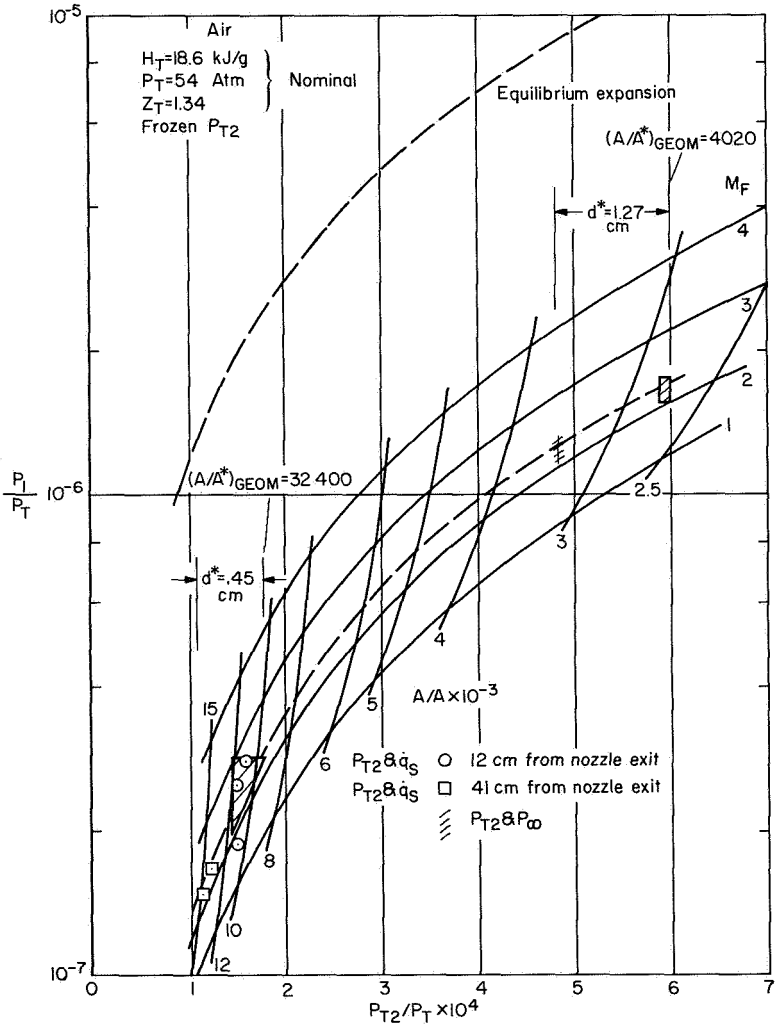

Figure 42.– Nozzle flow map.

The pressure probes used in these experiments are illustrated in figure 43. Stretched-diaphragm, variable-capacitance pressure cells were mounted in the probes behind heat sink baffles. The static pressure probe was mounted on the acceleration damping support (fig. 17), while the pitot probe was mounted on an adjustable rake that spanned the test stream. This rake also held several heat-transfer probes – thin copper hemispheres (2.5-cm diam and 0.012 mm thick) – instrumented at the stagnation point with 40-gage chromel-constantan thermocouples.

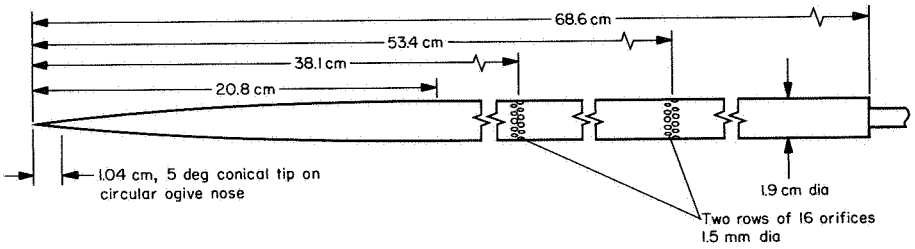

(a) Static pressure probe.

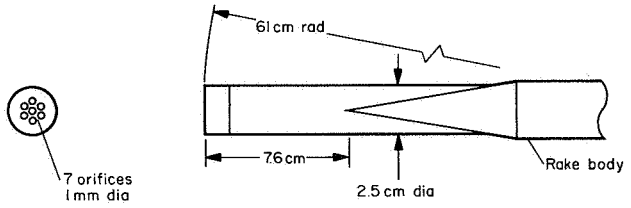

(b) Pitot pressure probe.

Figure 43.– Test section probes.

Pressure and heat-transfer measurements were made at two axial stations in the test section, one 12 cm downstream of the nozzle exit plane and the other 41 cm, for the nominal reservoir conditions $H_T = 18.6$ kJ/g and $P_T = 54$ atm. Nozzle throat diameters of 0.45 and 1.27 cm were used. Corrections to measured pitot pressure for low-density effects were found to be negligible. On the other hand, corrections to the static probe measurements were substantial and difficult to define (for a discussion, see appendix B).

Table 2 is a summary of test conditions and measurements. The first thing to note in the table is the agreement of measured and theoretical stagnation heating rates (columns 9 and 11) for the runs with the larger nozzle throat diameter (runs 1, 2, 24, 25, and 28). The theoretical rates were obtained from equation 3 of reference 31, which in present notation, is

$$\dot{q}_S = 86.9 \sqrt{\frac{P_{T2}}{R}} \left(\frac{U_\infty}{10000}\right)^{1.99} \left(1 - \frac{Hw}{H_T}\right) \tag{6}$$

where U_∞ is the local flow velocity appropriate to an equilibrium expansion. The observed agreement between theory and experiment is evidence of two conditions: first, that the energy of dissociation is recovered at the model surface by recombination either in the boundary layer or by

TABLE 2.– SUMMARY OF NOZZLE CALIBRATION DATA

Run	Reservoir conditions						Stream measurements				Dissociation heat balance			
	V_s, m/sec	P_T, atm	H_T, kJ/g	$(S/R)_T$	α_T	d^*, cm	P_{T2}/P_T $\times 10^4$	P_∞/P_T $\times 10^6$	$\dot{q}_s$, W/cm^2	Meas. interval, msec	Equil. $\dot{q}_s$, W/cm^2	Meas. $\dot{q}_s$ / equil. $\dot{q}_s$	M_F	Test station
1	4200	51.0	17.25	38.35	0.308	1.27			327	1.6	321	1.02		1
2	4270	53.0	17.75	38.55	.318	1.27			321	1.2	336	.96		1
5	4300	50.3	17.65	38.55	.316	1.27	5.70			1.4				1
7	4340	51.0	18.00	38.70	.325	.45	1.80			1.2				1
8	4240	53.1	17.95	38.62	.322	.45			103	1.6	162	.64	2.1	1
9	4210	57.8	17.50	38.27	.310	.45	1.60			1.3				1
10	4340	51.0	18.65	39.00	.338	.45		2.73[a]		.7				1
11	4310	51.0	18.10	38.75	.326	.45		2.70[a]		.7				1
12	4260	51.0	18.00	38.70	.324	.45		2.45[a]		2.0				1
13	4150	57.9	17.50	38.30	.314	.45		2.00[b]		.5				1
14	4300	57.8	18.60	38.80	.335	.45		1.85[b]		.7				1
17	4310	59.5	18.70	38.80	.337	.45		1.80[b]		1.0				1
18	4240	63.3	18.35	38.50	.327	.45		1.81[c]		1.6				1
21	4360	54.4	19.05	39.05	.346	1.27		3.45[b]		1.6				1
22	4020	44.2	16.00	37.95	.283	.45	1.50		83	1.3	118	.70	2.7	1
23	4080	47.6	16.55	38.10	.293	.45	1.45		85	1.5	129	.66	2.3	1
24	3840	44.2	14.85	37.40	.257	1.27	6.00		222	1.0	214	1.03		1
26	4140	47.6	16.95	38.30	.302	.45	1.14		75	1.7	117	.65	2.2	2
27	4180	49.7	17.40	38.45	.312	.45	1.24		85	2.4	129	.66	2.3	2
28	4250	64.6	18.70	38.70	.336	1.27	4.80		284	1.8	293	.97		2
34	4320	62.9	19.25	39.00	.348	.45	1.50		100	2.1	165	.61	1.9	1
56	4270	51.0	18.20	38.80	.329	1.27				1.6				1
57	4240	51.0	17.85	38.65	.320	.45	1.80			1.3				1
58	4340	51.0	18.50	38.95	.336	1.27	5.90			1.7				1

[a]Ogive nose L/D = 6.0

[b]Ogive nose L/D = 10.9

[c]Ogive nose L/D = 5.2

surface reaction, and second, that the total stream enthalpy is the same as that in the reservoir during the interval of measurement (column 10 of table 1).[6] This latter result has also been observed in references 2 and 30 for air and nitrogen over a range of reservoir enthalpies. Thus, it is concluded that at the present conditions there is no significant loss of energy from the central core of reservoir gas to the enclosing walls during the test period.

With the 0.45 cm nozzle throat (runs 8, 22, 23, 26, and 34), the measured stagnation heating rates were only 60 to 70 percent of the theoretical predictions, indicating that some of the flow energy is not available to the probe. Presumably, this would be in the inert energy modes, dissociation and molecular vibration. Accordingly, limiting estimates of gas reactions in the probe shock layer are summarized in table 3. These results show that very little dissociation or vibrational

TABLE 3.–ESTIMATES OF GAS REACTIONS IN PROBE SHOCK LAYER FOR R = 1.27 cm

Energy exchange process	Defining parameter	Calculated value		Degree of activity $(\Delta E/HT)_{A/A^*=11{,}000}$	Ref. no.
		A/A^* = 2800 $P_{T2} = 3.3\times10^{-2}$ atm	A/A^* = 11000 $P_{T2} = 8.2\times10^{-3}$ atm		
Oxygen dissociation	$(d\alpha/dt)_O \times \tau_R$ Rate × Residence time	0.023 – 0.035	0.006 – 0.009	<0.007	32
Nitrogen dissociation	$(d\alpha/dt)_N \times \tau_R$	0.008	0.002	<0.003	32
Nitrogen vibrational excitation	τ_V/τ_R Excitation time / Residence time	12.4	40.3	~0	32
Recombination on surface	$\dfrac{\dot{q}_s - (\dot{q}_s)_{K_w}}{(\dot{q}_s)_{K_w=\infty} - (\dot{q}_s)_{K_w=0}} = 0$	0.55 – 0.84	0 – 0.24	<0.054	33
Recombination in boundary layer	C_1 Diffusion time / Char. atom lifetime	$<8\times10^{-6}$	$<2\times10^{-6}$	0	33
Combined gas – surface recombination	C_1^* Residence time / Recombination time	2×10^{-3}	$<1\times10^{-4}$	0	34
Recovery of vibrational energy	- - -	- - -	- - -	0.069	- - -

[6] Reservoir enthalpy is defined here by using the measured pressure and the entropy corresponding to the equilibrium, reflected-shock conditions.

excitation will occur in the shock layer ($A/A^* = 11{,}000$), so that the gas approaching the stagnation point of the probe is essentially at free-stream composition and excitation level due to the relatively low pressure and short flow residence time on this small probe. Further, the results show that no atom recombination will occur in the stagnation region boundary layer, and very little, if any, on the surface itself. This last reaction, the recombination due to surface catalycity, is the most difficult to evaluate. Taken along, after the manner of reference 33, a measurable energy recovery is predicted. Considered together with the gas-phase behavior near the surface (as in ref. 34), the energy recovery should be negligible. This disparity is resolved by comparison of theory with measured results in figure 44, where the heating rate to a surface of arbitrary catalycity is ratioed to that for a fully catalytic surface and plotted versus effective freeze Mach number. The lower dashed curves, for K_W (the catalytic reaction rate constant) equal to 0, represent the case for no surface energy recovery and compare favorably with experiment.

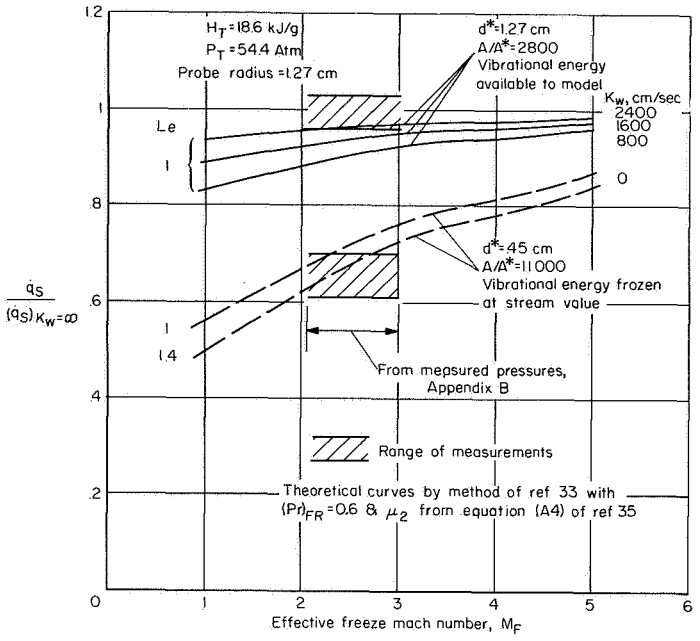

Figure 44.– Energy available to heat-transfer probe.

To summarize, table 3 and figure 44 define the condition of the shock layer on the heat-transfer probe as follows:

1. At the higher density condition ($A/A^* = 2800$)the inviscid layer is essentially frozen at the stream composition, the boundary layer is also chemically inactive, but the surface reaction is sufficiently fast ($K_W > 2000$) that both the dissociation and vibrational energies are fully recovered.

2. In the lower density flow at $A/A^* = 11{,}000$, the shock layer is completely inactive, and the surface reaction is negligible in that essentially none of the dissociation or vibrational energy is recovered.

It is somewhat surprising that the energy exchange at the probe surface is so sensitive to a density change of only about 5; by inference from these results, it appears that the composite Damkohler number C_1^* (ref. 34) is more strongly influenced by diffusion of atoms in the boundary layer than the theory predicts.

Since both the shock layer and the surface are inactive at $A/A^* = 11{,}000$, the measured heating rate can be used to infer the atom concentration that exists in the flow approaching the probe. If both vibrational energy exchange and atom recombination are assumed to freeze at the same location in the nozzle expansion, the results are as shown by the symbols in figure 42. The effective M_F of this flow is 2.3 ± 0.4 based on the stagnation heating and pitot-pressure measurements. A similar result is obtained for this expansion ratio if pitot and static pressures are used to define the flow; the crosshatched area in the figure yields $M_F = 2.6 + 0.4$. Other results are shown

in the figure to define the flow (with $d^* = 0.45$ cm) 41 cm from the nozzle exit, and for both axial positions with $d^* = 1.27$ cm. To the accuracy of measurement, the effective freeze Mach number is essentially the same for both nozzle expansion ratios, and the resultant atom mass fraction is about 0.25. Thus, the recombination processes appear sufficiently rapid to return nearly all the nitrogen to molecular form, leaving essentially all the oxygen in the atomic state. Figure 42 also shows how far the actual flow departs from an equilibrium expansion, and the reduction in A/A^* due to the nozzle wall boundary layer.

For nominal reservoir conditions and $M_F = 2.3$ the remaining stream properties have been derived in table 4. The velocity is about 5040 m/sec, while Mach numbers vary from 16 to 24 for

TABLE 4.– SUMMARY OF TEST STREAM PROPERTIES

[H_T = 18.6 kJ/g; P_T = 54 atm; test gas, dry air; test time, 1.5 msec]

	$M_F = 2.3$			
	$d^* = 0.45$ cm		$d^* = 1.27$ cm	
	Station 1	Station 2	Station 1	Station 2
M_∞	22.9	23.8	15.9	16.9
U_∞, m/sec	5040	5050	5010	5020
T_∞, °K	95	83	184	167
Z_∞	1.25	1.25	1.25	1.25
P_∞, atm	1.23×10^{-5}	0.86×10^{-5}	9.12×10^{-5}	6.53×10^{-5}
ρ_∞, g/cm^3	3.69×10^{-8}	2.91×10^{-8}	1.41×10^{-7}	1.11×10^{-7}
Density alt., km	76.2	77.8	66.5	68.3
Re/cm	230	185	525	450
Test core diam., cm	30	35	45	>45
A/A^*	11000	14000	2800	3500
Frozen chemical energy fraction	0.255	0.255	0.255	0.255
Frozen vibrational energy fraction	0.073	0.073	0.073	0.073

the different stream temperatures. Stream Reynolds numbers vary from about 180 to 525 per centimeter, and test core diameters from 30 cm to more than 45 cm. The inactive energy tied up in dissociation and vibrations is about 1/3 the total stream energy. This set of properties represents test conditions available for aerodynamic studies at the exit of the 76-cm nozzle with H_T = 18.6 kJ/g.

Axial and transverse gradients—The axial and transverse variations of flow properties in the test region are illustrated by results from pitot-pressure surveys (fig. 45). With the 1.27 cm nozzle throat, measurements in the vertical center plane show a test core about 40 to 45 cm in diameter with a reasonably uniform profile. The flow overexpands slightly near the centerline and is not quite symmetrical, with an underexpanded region near the top edge of the inviscid core. The wall boundary layer is about 15 cm thick. Corresponding Mach numbers are shown in the lower part of figure 45(a); the axial gradient is about 0.036 units/cm.

In figure 45(b), the survey data with d^* = 0.45 cm are shown for both the horizontal and vertical center planes. The test core is generally symmetric about the centerline, is about 30 to 35 cm in diameter, and is slightly overexpanded in the center region. The wall boundary layer is about 20 cm thick. In the lower part of the figure, the corresponding Mach numbers indicate an axial gradient of 0.33 units/cm.

These calibration results show that the inviscid conical flow is rather strongly influenced by the nozzle wall boundary layer. Ideally, the flow in any cross plane should expand beyond the centerline value with increasing radial

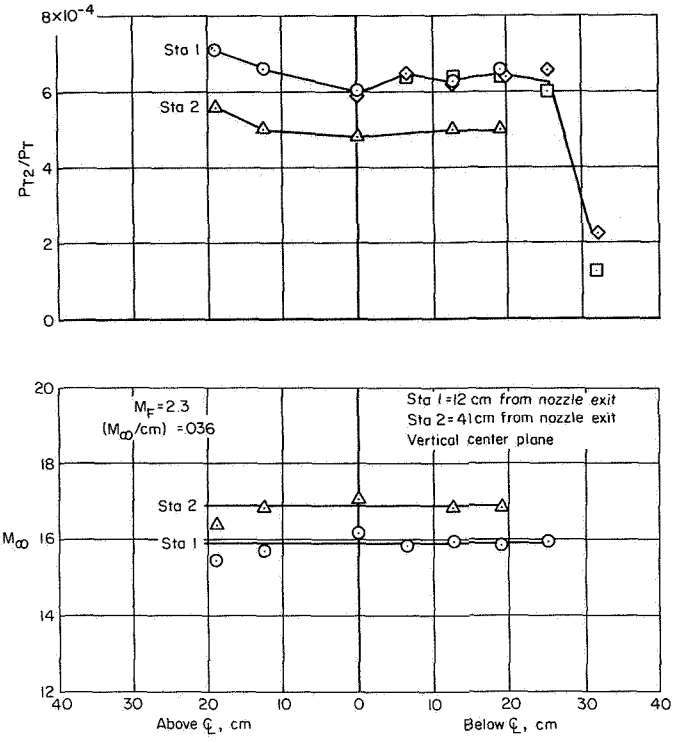

(a) d^* = 1.27 cm

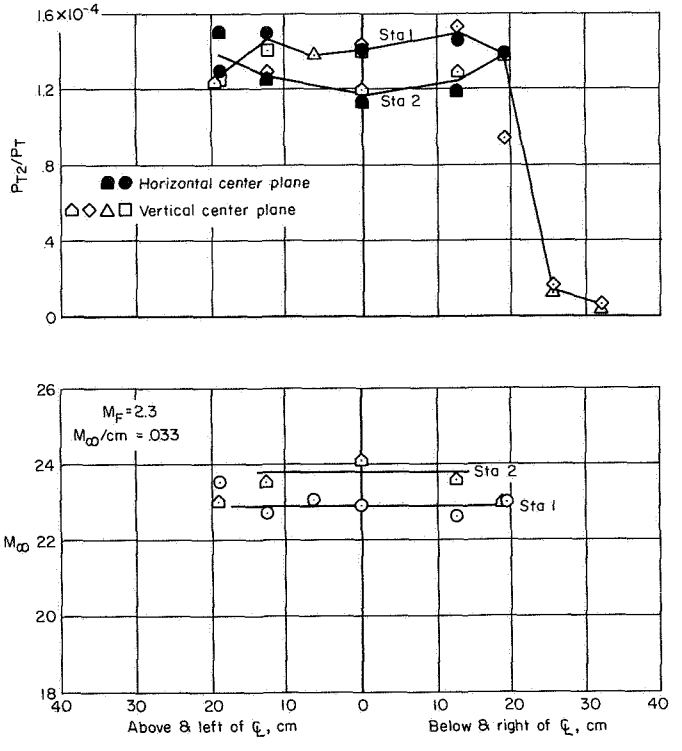

(b) d^* = 0.45 cm

Figure 45.— Pitot pressure and Mach number variation in test region.

distance, whereas in practice the opposite is true. Thus, the boundary layer is acting to modify the nozzle shape so that the inviscid flow is turned inward and the local flow angles in the outer region of the test core are reduced. If this effect of aerodynamic contouring is included, the maximum local flow angles in the test core are estimated to be no more than 5° and 3°, respectively, for the $d^* = 1.27$ cm and 0.45-cm nozzle throats.

CONCLUDING REMARKS

The design and performance of a high enthalpy shock tunnel using arc-heated helium as the driver gas has been described, and the potential range of operation as a gasdynamic test facility at total stream energies from 7000 to 35,000 J/g has been indicated. Arc-discharge heating has proven to be a reliable method of energizing many different gases, to the end that reservoir conditions suitable for large nozzle expansions can be achieved for a variety of test gases and entropy levels.

The initial energy conversion efficiency of the arc driver (in terms of shock speed) varied from nearly 100 percent to about 75 percent as the driver-gas temperature increased from 3000° to 8600° K. Conversely, shock-wave attenuation was substantially above theoretical predictions at high driver temperatures and lower shock velocities, indicating that energy losses in the driver are time dependent.

Tailored interface conditions occurred at pressures about a factor of 3 below predictions, as operation was adjusted to compensate for shock-wave attenuation; with driver temperature, the tailored shock Mach number in air increased from 11.5 at 3500° K to 14.6 at 4500° K.

A preliminary nozzle calibration was obtained in air at a nominal reservoir pressure of 54 atm and enthalpy of 18,600 J/g. The flow in the test section was essentially a mixture of atomic oxygen and molecular nitrogen, moving at a velocity of 5000 m/sec. Mach numbers varied from 16 to 24 and Reynolds numbers from 200 to 500 per centimeter, for test core sizes from 30 to 45 cm. Flow times suitable for aerodynamic testing averaged 1.5 to 2.0 msec at these conditions; no significant loss of total stream energy occurred during the test period.

Ames Research Center
National Aeronautics and Space Administration
Moffett Field, Calif., 94035, Nov. 5, 1972

APPENDIX A

LOSS OF TEST GAS BY INTERFACE LEAKAGE

Ideal shock-tube theory has the separation distance between the shock wave and contact surface increasing linearly with distance from the diaphragm. When viscosity is included, the wall boundary layer that develops behind the shock wave becomes a gasdynamic sink that moves the test gas past the contact surface. This causes the shock to slow down and the contact surface to speed up, reducing the separation distance below the ideal value. This reduction obviously will decrease the size of the test gas slug behind the reflected shock.

The work of Mirels has become the classical standard for predicting these losses, as presented in references 25 and 26 for laminar and turbulent boundary layers, respectively. In the present application, predicted separation distances will be compared with measured values behind the incident shock and the extent of the reservoir gas slug will be inferred from this result. Figure 46 shows a representative set of M_S data for nominal $T_4 = 5300°$ K and $P_4 = 310$ atm; note that shock attenuation decreases at lower initial pressures. In figure 47, the same data are represented by Reynolds numbers based on the predicted separation distance, using an expression similar to Mirels':

$$Re_{\ell} = \frac{P_2 \bar{u}_2 \left[(V_S/\bar{u}_2) - 1\right] \ell}{\mu_2} \tag{A1}$$

where $\bar{u}_2$ is the gas velocity relative to the shock wave and ℓ, the predicted separation distance at $x/D = 110$, for either the laminar or turbulent boundary layer. The dashed lines in the figure are extensions of the approximate limits suggested by Mirels for the region of boundary-layer transition between the shock and contact surface. For the present operating conditions, the transition region is indicated at M_S about 10 to 12 at Reynolds numbers near 10^7, in reasonable agreement with the location of the decrease in shock attenuation noted in figure 46. (The theory predicts laminar attenuation to be less than turbulent attenuation.)

Combining these ideas in figure 48, incident test slug length is shown in relation to initial pressure, P_1, with laminar and turbulent predictions shown as solid lines. The symbols denote values measured near the end of the tube with the impedance probe; filled symbols correspond to the data of the previous two figures. Agreement is good at high and low pressures where the boundary layer is fully turbulent or fully laminar, while a transition band lying somewhat below the prediction connects the two curves. Incident slug lengths vary from 0.45 to 1.05 m.

The good agreement of experiment with theory for the incident shock wave serves as a basis for estimating the quantity of test gas behind the reflected shock. If other viscous loss mechanisms are neglected, and with the density ratio P_5/P_2 as the inverse of length, the results shown in figure 49 were obtained. Test gas lengths behind the reflected shock are shown as dashed lines. Solid lines represent the "equilibrium interface" condition, a quasi-steady situation occurring after secondary wave reflections between the end wall and interface have sensibly been damped. At high

initial pressures, the reservoir is undertailored, the final pressure (and density) is less than P_5, and the slug length increases. At low pressures the opposite is true as pressures increase above P_5 in successive compressions. Thus, lengths of 9 to 30 cm are predicted for a turbulent boundary layer, and 3 to 21 cm for a laminar boundary layer. Near tailoring, at $P_1 \approx 0.015$ atm, the length estimated in this manner is about 80 percent of the ideal. While these results are in the nature of an upper limit on the available test gas in the reservoir, it appears that a substantial fraction of the initial mass will be available in the test section.

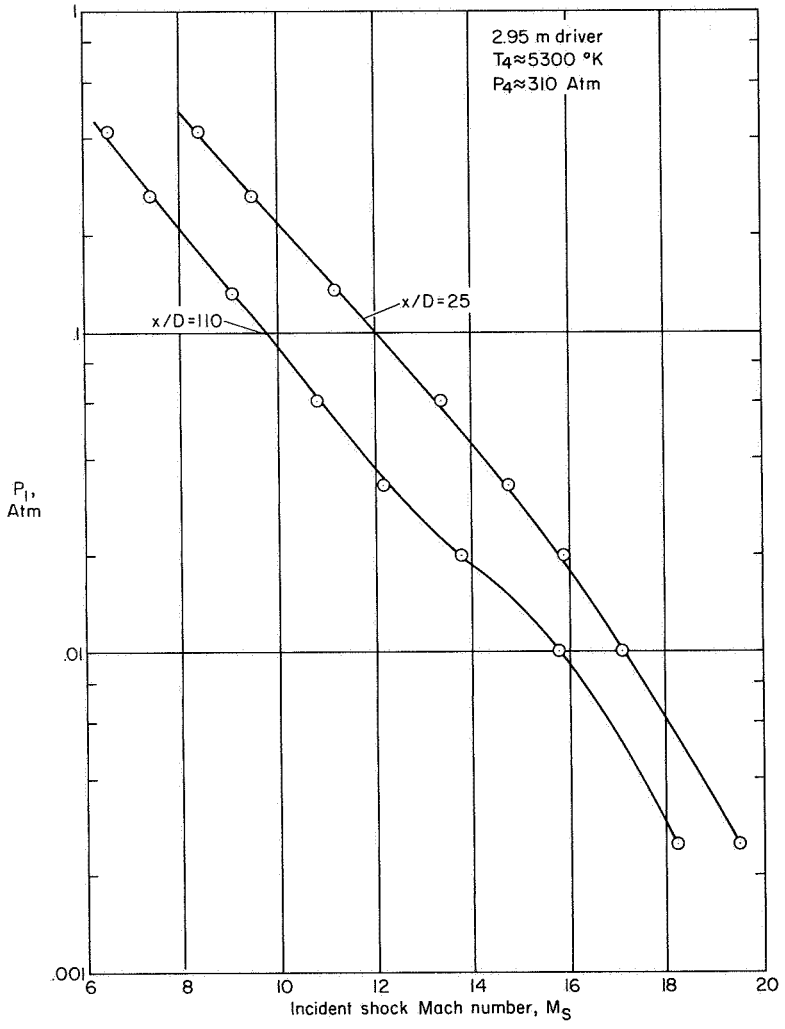

Figure 46.– Variation of M_S with initial pressure in tube.

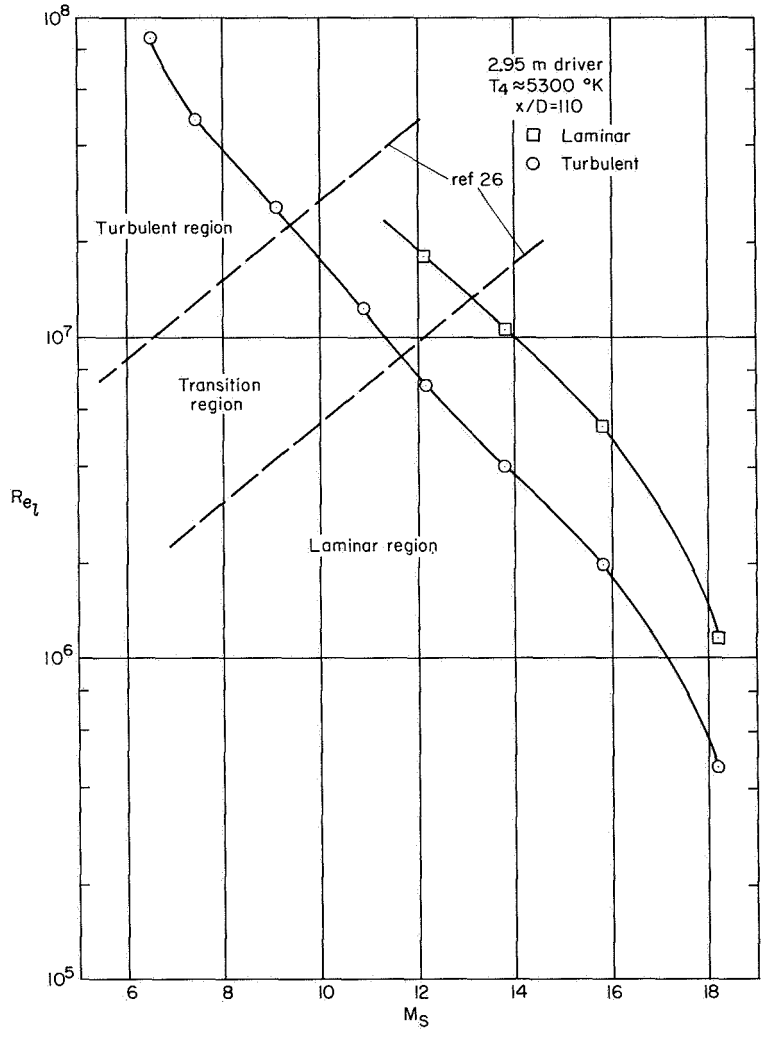

Figure 47.– Reynolds numbers for predicted shock-interface separation distance.

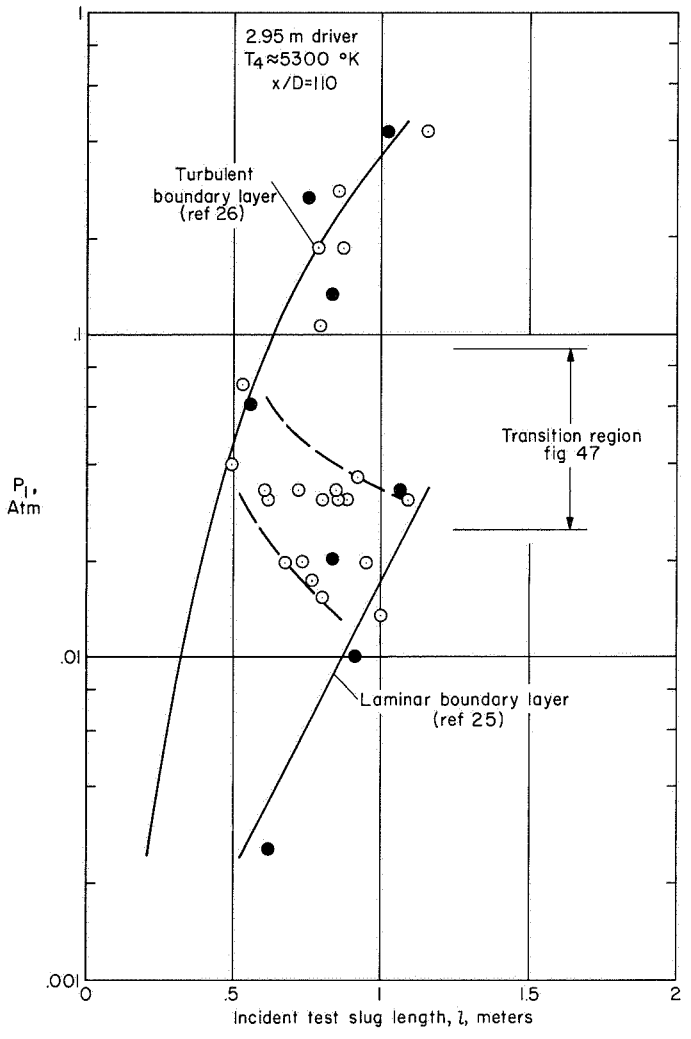

Figure 48.– Variation of test slug length in laminar and turbulent regions.

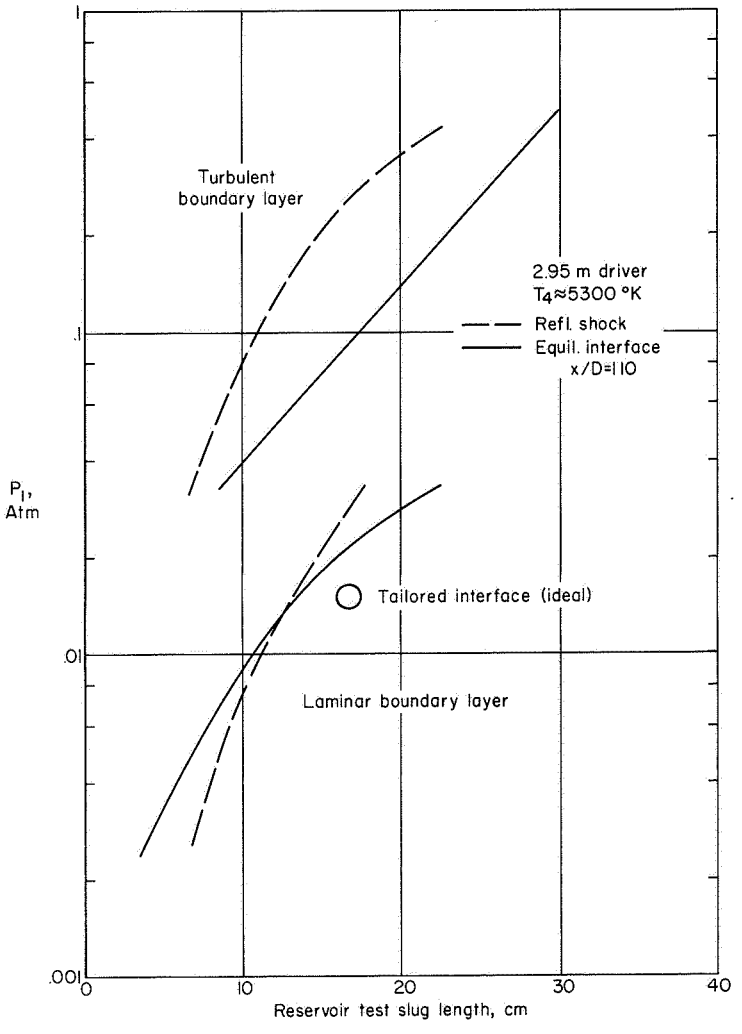

Figure 49.– Estimated length of test slug at reservoir conditions.

APPENDIX B

REDUCTION OF STATIC PROBE PRESSURE MEASUREMENTS

The measurement of static pressure in shock-heated, high Mach number gas streams is difficult for many reasons. The absolute pressure is below the operating range of conventional transducers, considering the size limitation and required response time; the temperature potential of the flow requires thermal shielding which, if in the form of an orifice and cavity, introduces substantial orifice corrections; and the boundary-layer-induced pressures in high Mach number, low-density flow are not well understood. In the present calibration study, a stream probe was used, rather than side-wall pressure taps, to evaluate static pressure in the test region. A slender, cylindrical shape with changeable ogive tip sections was used (see fig. 43). Runs were made with ogive tips having fineness ratios of 5.2, 6.0, and 10.9 (as shown in table 2), and measured pressures ranged from 4×10^{-5} to 13×10^{-5} atm (30 to 100 μHg absolute). These results were corrected for low-density effects at the orifice using the method of reference 36 (listed in table 2).

Allowance for boundary-layer-induced pressures was made using the theoretical formulation of reference 37, modified slightly to accord with two numerical solutions of similar low-density, high Mach number flows over very slender bodies, and the experimental results of reference 38. From equation 49 of reference 37, the viscous induced pressure on a blunted slender rod can be expressed as

$$\frac{P_V - P_\infty}{P_\infty} = \frac{1}{2}\left\{\sqrt{\left(\frac{P_b}{P_\infty}\right)^2 + \frac{\gamma(\gamma+1)}{2}\left[(1-n)K_4\right]^2\left(\frac{\bar{C}G^2M_\infty^6}{Re_{d,\infty}\,x/d}\right)} - \frac{P_b}{P_\infty}\right\} \tag{B1}$$

where

$$G = 1.72\left(\frac{\gamma-1}{2}\right)\left(\frac{T_w}{T_T} + 0.386\right) \quad \text{and} \quad \bar{C} = \frac{\mu_w T_\infty}{\mu_\infty T_w} \tag{B2}$$

while n and K_4 relate to the *inviscid* pressure decay in the blast-wave region just downstream of the blunt tip. For present purposes, equation (B1) was modified as follows. First, the term $[(1-n)K_4]^2$ was assumed to be unity, that is, the limiting value for small viscous interaction. Justification for this action is based on two observations: (1) for the slender probe tips used here, the predicted inviscid pressure distribution (see fig. 50) is not like a blast-wave decay, but shows flow overexpansion at the tip-cylinder juncture (shoulder) with a subsequent pressure recovery back

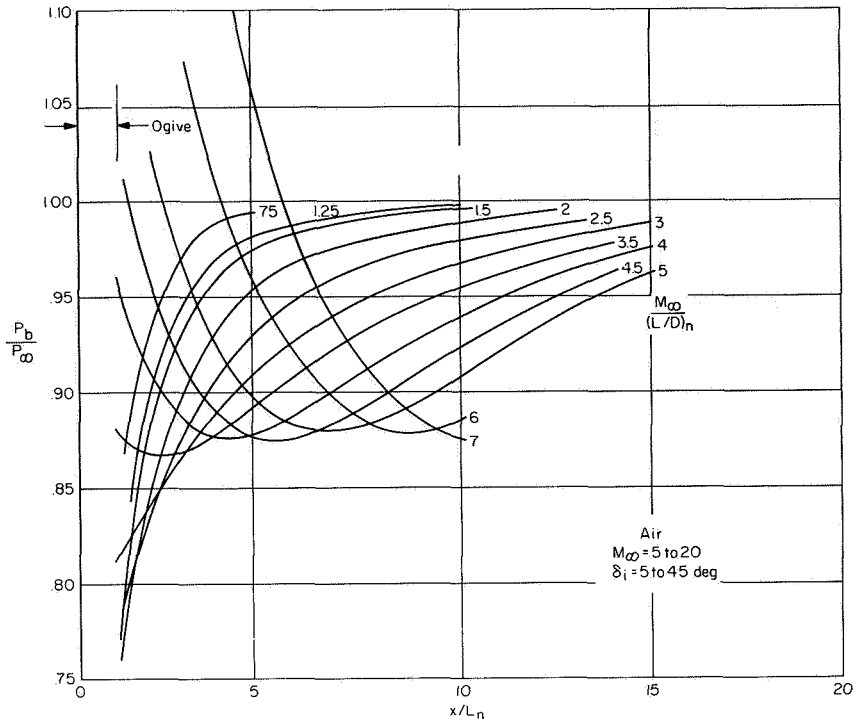

Figure 50.– Correlation of method of characteristics solutions for ogive-cyclinder bodies; ideal gas, $\gamma = 1.4$.

to the stream value along the cylinder; (2) the thick boundary layer on the cylinder, far from the shoulder, is expected to grow gradually, which will not induce large surface pressure gradients. Thus, the flow field on the cylinder, which in conventional terms could be classified as a strong interaction region with large values of the parameter $M^3/\sqrt{Re}$, actually does not exhibit such behavior. The second (and minor) change in equation (B1) is to replace T_w/T_t in the expression for G with H_w/H_T, the enthalpy ratio.

To check the validity of these arguments and the usefulness of equation (B1) for slender pointed bodies, several predictions of induced pressure are compared with numerical solutions in figure 51. The first case (fig. 51(a)) is for an equilibrium, uniform flow of air at $M_\infty = 10$; the numerical solution was obtained by iterating between the inviscid flow (MOC) and the flow with boundary layer, after the method of reference 39. At $x/D > 10$, the induced pressure is relatively small and both methods give about the same result, although the axial gradient is less by the approximate method. In the second case (fig. 51(b)), the uniform, frozen flow conditions for the numerical prediction are approximately those of the present tests, while the probe geometry is identical. The iterative solution (ref. 40) follows the work of Gravalos et al. and Levine. In this case, the induced pressures are sizable and the axial gradient at $x/D > 10$ is fairly large. The approximate prediction again shows a smaller gradient, although the pressure level is comparable. In figure 51(c), the comparison is with the theoretical and experimental results of reference 38. Again the stream flow is uniform and essentially in equilibrium, while the probe is a very slender cone cylinder. The range of measured data is shown by the bar symbols. In this case, the approximate prediction compares very well with the data of Ellinwood (ref. 38) at $M_\infty = 20$ in air.

In view of the favorable results obtained in these comparisons, the modified form of equation (B1) was used along with the experimental values of surface pressure to solve for the local static

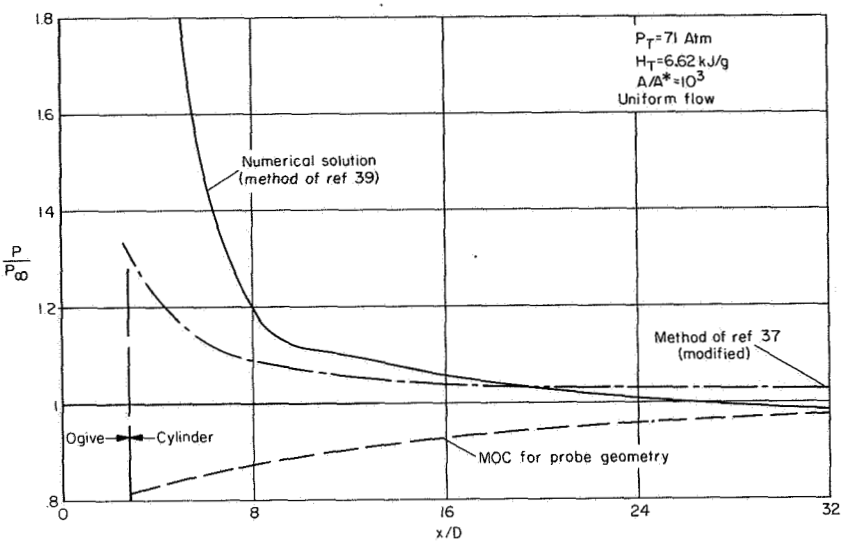

(a) $M_\infty = 10, (L/D)_n = 2.83$ ogive cylinder.

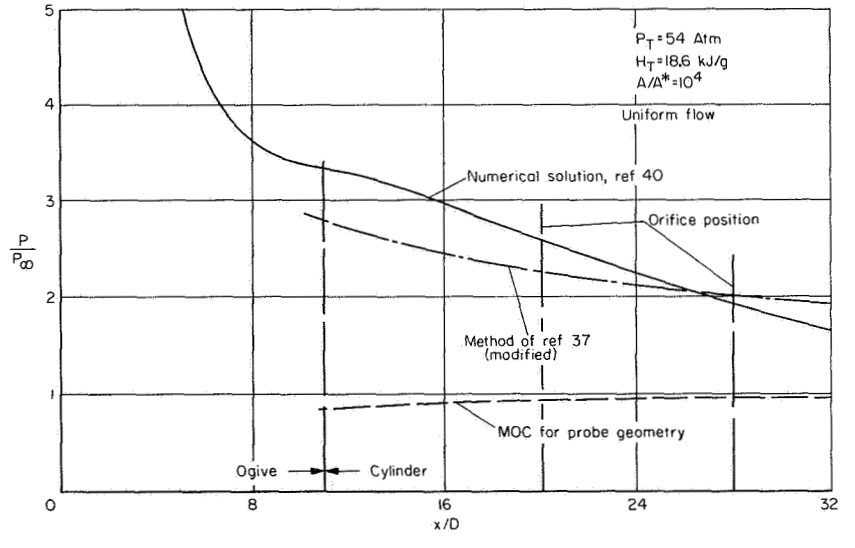

(b) $M_\infty = 14, (L/D)_n = 10.9$ ogive cylinder.

Figure 51.– Variation of inviscid and viscous induced pressures on slender pointed cylinders.

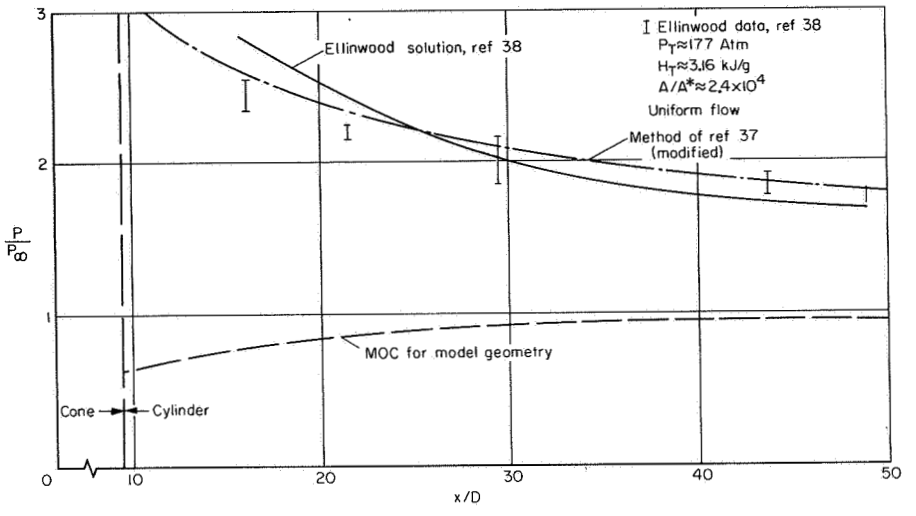

(c) $M_\infty = 20, (L/D)_n = 9.5$ cone cylinder.

Figure 51.– Concluded.

pressure. Solutions were obtained for several assumed values of M_F until the initial and final P_∞ were equal. The required stream properties M_∞, Re_∞, T_∞ in each case were those appropriate to the assumed M_F (after ref. 2, and as discussed earlier in connection with fig. 42). The pressure correction factor was based on stream properties in the actual flow at the model tip, even though the test flow is a modified conical expansion. The pressure correction so obtained is probably on the low side; nevertheless, it should be more representative of the pressure field of the developing boundary layer than a correction based on the local stream properties at the A/A^* of the orifice location (see fig. 42).

REFERENCES

1. Wittliff, C. E.; Sundaram, T. R.; Rae, W. J.; and Lordi, J. A.: Study of High-Density Hypervelocity Flows and Similitudes. AEDC–TR–67–72, 1967.

2. Hiers, Robert S. Jr.; and Reller, John O. Jr.: Analysis of Nonequilibrium Air Streams in the Ames 1-Foot Shock Tunnel. NASA TN D–4985, 1969.

3. Loubsky, William J.; and Reller, John O. Jr.: Analysis of Tailored - Interface Operation of Shock Tubes With Helium-Driven Planetary Gases. NASA TN D–3495, 1966.

4. Dannenberg, Robert E.; and Silva, Anthony F.: Exploding Wire Initiation and Electrical Operation of a 40–kV System for Arc-Heated Drivers up to 10 Feet Long. NASA TN D–5126, 1969.

5. Camm, John C.; and Rose, Peter H.: Electric Shock Tube for High Velocity Simulation. AFCRL–62–568, AVCO, 1962.

6. Gruszczynski, J. S.; and Warren, W. R. Jr.: Experimental Heat Transfer Studies of Hypervelocity Flight in Planetary Atmospheres. AIAA J., vol. 2, no. 9, Sept., 1964, pp. 1542–1550.

7. Dannenberg, Robert E.; and Humphry, Donald E.: Microsecond Response System for Measuring Shock Arrival by Changes in Stream Impedance in a Shock Tube. Rev. Sci. Inst., vol. 39, no. 11, Nov. 1968, pp. 1692–1696.

8. Ackroyd, J. A. D.: A Study of Running Times in Reflected Shock Tunnels. ARC–CP–883, 1967.

9. Smith, C. Edward: The Starting Process in a Hypersonic Nozzle. J. Fluid Mech., vol. 24, pt. 4, Apr. 1966, pp. 625–640.

10. Laval, Pierre: Pseudo-Viscosity Method and Starting Process in a Nozzle. La Recherche Aerospatiale, N. 131 July-August 1969, pp. 4–16, (NASA TT F–12, 863).

11. Chisnell, R. F.: The Motion of a Shock Wave in a Channel, with Applications to Cylindrical and Spherical Shock Waves. J. Fluid Mech., vol. 2, pt. 3, May, 1957, pp. 286–298.

12. Softley, E J.; and Graber, B. C.: An Experimental Study of the Pressure and Heat Transfer on the Base of Cones in Hypersonic Flow. AGARD Proc. no. 19, vol. 1, May 1967.

13. Holder, D. W.; and Shultz, D. L.: Note on the Time Required for the Achievement of Steady Flow Past a Slender Body in a Hypersonic Shock Tunnel. ARC–CP–567, ARC 22, 512, 1961.

14. Rom, Josep: Measurements of Heat Transfer Rates in Separated Regions in a Shock Tube and in a Shock Tunnel. AIAA J., vol. 1, no. 9, Sept. 1963, pp. 2193–2194.

15. Powers, W. E.; Stetson, K. F.; and Adams, M. C.: A Shock Tube Investigation of Heat Transfer in the Wake of a Hemisphere- Cylinder, with Application to Hypersonic Flight. AVCO Corp., Res. Rep. 30, 1958.

16. Coon, G. W.: A Diaphragm Type Capacitance Transducer. U.S. Patent 3,027,769, 1962.

17. Seegmiller, H. L.: Inertia Diaphragm Pressure Transducer. U.S. Patent 3,352,157, 1967.

18. Seegmiller, H. Lee; and Mazer, Louis: A 500,000 Sample Per Second Digital Recorder for the Ames Electric Arc Shock Tunnel. 3rd Int. Congress on Inst. in Aerospace Simulation Facilities (IEEE), 1969, pp. 243–247.

19. Dannenberg, Robert E.; and Katzman, Howard: An Application of Optical Telemetry to Shock-Tube Measurements. Rev. Sci. Inst., vol. 40, no. 5, May, 1969, pp. 640–642.

20. Dannenberg, R. E.: An Imploding Trigger Technique for Improved Operation of Electric Arc Drivers. Shock Tubes, Proceedings Seventh International Shock Tube Symposium Edited by I. I. Glass, University of Toronto Press, Toronto, 1970, pp. 186–200.

21. Cheng, D. Y.; and Dannenberg, Robert E.: Dark Pause Measurements in a High Pressure Arc Discharge. AIAA J., vol. 9, no. 1, Jan. 1971, pp. 184–186.

22. Dannenberg, Robert E.; and Silva, Anthony F.: Arc Driver Operation for Either Efficient Energy Transfer or High-Current Generator. NASA TM X–62,162, May, 1972.

23. Flagg, R. F.: Detailed Analysis of Shock Tube Tailored Conditions. RAD–TM–63–64, AVCO Corp., 1963.

24. Mirels, H.; and Mullen, J. F.: Small-Perturbation Theory for Shock Tube Attenuation and Nonuniformity. Phys. Fluids, vol. 7, no. 8, Aug. 1964, pp. 1208–1218.

25. Mirels, Harold: Test Time in Low-Pressure Shock Tubes. Phys. Fluids, vol. 6, no. 9, Sept. 1963, pp. 1201–1214.

26. Mirels, Harold: Shock Tube Test Time Limitation Due to Turbulent-Wall Boundary Layer. AIAA J., vol. 2, no. 1, Jan. 1964, pp. 84–93.

27. Mark, Herman: The Interaction of a Reflected Shock Wave With the Boundary Layer in a Shock Tube. NACA TM 1418, 1958.

28. Davies, L.: The Interaction of the Reflected Shock with the Boundary Layer in a Shock Tube and Its Influence on the Duration of Hot Flow in the Reflected-Shock Tunnel. Part I, NPL Aero. Rept. 1158, July 1965; Part II, NPL Aero. Rept. 1167, Sept. 1965.

29. Blair M. F.: Performance of the JPL 43–Inch Hypersonic Shock Tunnel. NASA CR–101634/-JPL–TR32–1370, 1969.

30. Reller, J. O., Jr.: and Reddy, N. M.: Analysis of the Flow in a One-Megajoule Electric-Arc Shock Tunnel. NASA TN D–6865, 1972.

31. Marvin, Joseph G.; and Akin, Clifford M.: Pressure and Convective Heat-Transfer Measurements in a Shock Tunnel Using Several Test Gasses. NASA TN D–3017, 1965.

32. Thomas, R. E.; Brooke, D.; and Petrie, S. L.: Similitude for Normal Shock Waves in Non-Equilibrium Flows. AFFDL–TR–65–91, 1965.

33. Pope, R. B.: Stagnation-Point Convective Heat Transfer in Frozen Boundary Layers. AIAA J., vol. 6, no. 4, Apr. 1968, pp. 619–626.

34. Inger, George R.: Nonequilibrium Stagnation Point Boundary Layers with Arbitrary Surface Catalycity. AIAA J., vol. 1, no. 8, Aug. 1963, pp. 1776–1784.

35. Okuno, Arthur F. and Park, Chul: Stagnation-Point Heat-Transfer Rate in Nitrogen Plasma Flows: Theory and Experiment. ASME 69–WA/HT–49, 1969.

36. Guy, R. W.; and Winebarger, R. M.: Effect of Orifice Size and Heat-Transfer Rate on Measured Static Pressures in a Low-Density Arc-Heated Wind Tunnel. NASA TN D–3829, 1967.

37. Bertram, Mitchel H.; and Blackstock, Thomas A.: Some Simple Solutions to the Problem of Predicting Boundary-Layer Self-Induced Pressures. NASA TN D–798, 1961.

38. Ellinwood, J. W.: Pressure-Interaction Methods for Axisymmetric, Hypersonic, Laminar, Unseparated Flows. Aerospace Corp., TR–0059 (6240–10)–3, 1971.

39. Clutter, Darwin W.; and Smith, A. M. O.: Solution of the General Boundary-Layer Equations for Compressible Laminar Flow, Including Transverse Curvature. Rept. LB31088, Douglas Aircraft Co., 1963.

40. Rie, H.: Inviscid Flow Field and Boundary Layer Calculations. Rept. 69 SD810 General Electric Co. RESD, under contract NAS2–5377.

NATIONAL AERONAUTICS AND SPACE ADMINISTRATION
WASHINGTON, D.C. 20546

OFFICIAL BUSINESS
PENALTY FOR PRIVATE USE $300

SPECIAL FOURTH-CLASS RATE BOOK

POSTAGE AND FEES PAID
NATIONAL AERONAUTICS AND SPACE ADMINISTRATION
451

U.S. MAIL

POSTMASTER: If Undeliverable (Section 158 Postal Manual) Do Not Return

"The aeronautical and space activities of the United States shall be conducted so as to contribute . . . to the expansion of human knowledge of phenomena in the atmosphere and space. The Administration shall provide for the widest practicable and appropriate dissemination of information concerning its activities and the results thereof."

—NATIONAL AERONAUTICS AND SPACE ACT OF 1958

NASA SCIENTIFIC AND TECHNICAL PUBLICATIONS

TECHNICAL REPORTS: Scientific and technical information considered important, complete, and a lasting contribution to existing knowledge.

TECHNICAL NOTES: Information less broad in scope but nevertheless of importance as a contribution to existing knowledge.

TECHNICAL MEMORANDUMS: Information receiving limited distribution because of preliminary data, security classification, or other reasons. Also includes conference proceedings with either limited or unlimited distribution.

CONTRACTOR REPORTS: Scientific and technical information generated under a NASA contract or grant and considered an important contribution to existing knowledge.

TECHNICAL TRANSLATIONS: Information published in a foreign language considered to merit NASA distribution in English.

SPECIAL PUBLICATIONS: Information derived from or of value to NASA activities. Publications include final reports of major projects, monographs, data compilations, handbooks, sourcebooks, and special bibliographies.

TECHNOLOGY UTILIZATION PUBLICATIONS: Information on technology used by NASA that may be of particular interest in commercial and other non-aerospace applications. Publications include Tech Briefs, Technology Utilization Reports and Technology Surveys.

Details on the availability of these publications may be obtained from:

SCIENTIFIC AND TECHNICAL INFORMATION OFFICE

NATIONAL AERONAUTICS AND SPACE ADMINISTRATION

Washington, D.C. 20546